

Quadruple-Junction Thin-Film Silicon-Based Solar Cells

Si, Fai Tong

DOI

[10.4233/uuid:36b80a78-ffd2-4a3d-a6b3-9bbc188b255e](https://doi.org/10.4233/uuid:36b80a78-ffd2-4a3d-a6b3-9bbc188b255e)

Publication date

2017

Document Version

Final published version

Citation (APA)

Si, F. T. (2017). *Quadruple-Junction Thin-Film Silicon-Based Solar Cells*. [Dissertation (TU Delft), Delft University of Technology]. <https://doi.org/10.4233/uuid:36b80a78-ffd2-4a3d-a6b3-9bbc188b255e>

Important note

To cite this publication, please use the final published version (if applicable).
Please check the document version above.

Copyright

Other than for strictly personal use, it is not permitted to download, forward or distribute the text or part of it, without the consent of the author(s) and/or copyright holder(s), unless the work is under an open content license such as Creative Commons.

Takedown policy

Please contact us and provide details if you believe this document breaches copyrights.
We will remove access to the work immediately and investigate your claim.

Quadruple-Junction Thin-Film Silicon-Based Solar Cells

Fai Tong Si

Quadruple-Junction Thin-Film Silicon-Based Solar Cells

Proefschrift

ter verkrijging van de graad van doctor
aan de Technische Universiteit Delft,
op gezag van de Rector Magnificus prof.ir. K.C.A.M. Luyben,
voorzitter van het College voor Promoties,
in het openbaar te verdedigen op
maandag 4 december 2017 om 15:00 uur

door

Fai Tong Si

Master of Engineering, Chinese Academy of Sciences, China
geboren te Macau

This dissertation has been approved by the promotor:

Prof.dr. M. Zeman

copromotor:

Dr.ir. O. Isabella

Composition of the doctoral committee:

Rector Magnificus

Prof.dr. M. Zeman

Dr.ir. O. Isabella

chairperson

Technische Universiteit Delft

Technische Universiteit Delft

Independent members:

Prof.dr. A.W. Weeber

Prof.dr. P.M. Sarro

Prof.dr. R. Schlatmann

Dr.ir. J.J. Schermer

Dr. J.-W. Schüttauf

Technische Universiteit Delft / ECN

Technische Universiteit Delft

HTW Berlin, Germany

Radboud Universiteit

CSEM, Switzerland

The work described in this thesis is a part of the programme "Stirring of Light!".
The programme is funded by the Foundation for Fundamental Research on Matter (FOM), which is part of the Netherlands Organization for Scientific Research (NWO).

ISBN: 978-94-028-0869-8

DOI: [10.4233/uuid:36b80a78-ffd2-4a3d-a6b3-9bbc188b255e](https://doi.org/10.4233/uuid:36b80a78-ffd2-4a3d-a6b3-9bbc188b255e)

Copyright © 2017 F.T. Si

All rights reserved. No part of this publication may be reproduced, stored in a retrieval system, or transmitted in any form or by any means without the prior written permission of the copyright owner.

Printed by *Ipskamp Printing*, the Netherlands.

Contents

Summary	vii
Samenvatting	ix
1 Introduction	1
1.1 The energy challenge	1
1.2 Photovoltaics	1
1.3 Thin-film silicon PV	3
1.3.1 Basics	3
1.3.2 Light management	6
1.3.3 Motivations for research	7
1.4 Multi-junction solar cells	10
1.4.1 Concept	10
1.4.2 Multi-junction TFSSC and its status	11
1.5 Goals of the work	12
1.6 Outline of the thesis	12
1.7 Contributions to the field	13
2 Quadruple-junction thin-film silicon-based solar cells with high open-circuit voltage	15
2.1 Introduction	16
2.2 Experimental	17
2.3 Initial demonstration	18
2.4 Simulation-assisted current matching	20
2.5 Device optimization	21
2.6 Discussion	22
2.7 Conclusions	23
3 Artifact interpretation of spectral response measurements on two-terminal multi-junction solar cells	25
3.1 Introduction	26
3.2 Terminology and scope	27
3.3 Experimental section	28
3.4 The model	29
3.5 Artifact analysis	32
3.5.1 Artifact formation by the drift of operation points	33
3.5.2 Effect of shunt resistance	33
3.5.3 Effect of bias conditions	37
3.5.4 Illumination-dependent response	39
3.5.5 Experimental application	45
3.6 On the proper measurement configuration and interpretation	47
3.7 Outlook	49
3.8 Conclusions	51

4	Thin-film amorphous silicon germanium solar cells with p- and n-type hydrogenated silicon oxide layers	53
4.1	Introduction	54
4.2	Experimental	55
4.3	Use of SiO _x :H in p-layer	57
4.4	Use of SiO _x :H in n-layer	59
4.5	Optical spacer at back reflectors	60
4.6	Improvement by light scattering substrates	62
4.7	Conclusions	64
5	Quadruple-junction thin-film silicon-based solar cells using four different absorber materials	65
5.1	Introduction	66
5.2	Experimental	68
5.3	Tunnel recombination junctions	70
5.4	Front TCO	71
5.5	Enhanced light scattering by MST	72
5.6	Potential improvements	73
5.7	Conclusions	75
6	Too many junctions? — a case study of multi-junction thin-film silicon-based solar cells	77
6.1	Introduction	78
6.2	Device structures and outline	79
6.3	Lossless estimation	81
6.4	Optical analysis	82
6.4.1	Spectral overlap	85
6.4.2	Parasitic absorption	85
6.4.3	Reflection losses	87
6.5	Tunnel recombination junctions	89
6.6	Filtered illumination	91
6.7	Thickness limitations	92
6.8	Optimal number of subcells	94
6.9	Variations in photocurrent generation	95
6.10	Conclusions	99
7	Conclusions and Outlook	101
7.1	Conclusions	101
7.2	Outlook	103
	Bibliography	105
	Acknowledgements	125
	List of Publications	127
	Curriculum Vitae	131

Summary

The direct utilization of sunlight is a critical energy source in a sustainable future. One of the options is to convert the solar energy into electricity using thin-film silicon-based solar cells (TFSSCs). Solar cells in a triple-junction configuration have exhibited the highest energy conversion efficiencies within the thin-film silicon photovoltaic technology. Going further from the state-of-the-art device structures, this thesis works on the concept of quadruple-junction TFSSCs, and explores the potential and feasibility of such configuration.

The initial experimental realization of quadruple-junction TFSSCs is demonstrated in Chapter 2. The fabricated thin-film $a\text{-SiO}_x\text{:H}/a\text{-Si:H}/nc\text{-Si:H}/nc\text{-Si:H}$ solar cells showed favorable fill factors (FF) and exceptionally high open-circuit voltages (V_{OC}) up to 2.91 V, suggesting a high quality of the material depositions and of the process control. Optical simulations were used in the design of the device structure, to precisely control the thickness and optical absorption in the layers. This preliminary experiment indicated how improvements can be made by better light management.

The spectral response of the component subcells is important information for the study of multi-junction solar cells, and the accurate measurement of such properties turns out to be challenging. Chapter 3 analyzes the mechanism of the spectral response measurement of multi-junction solar cells, by means of modeling the optoelectrical response of the subcells and their internal interactions. The formation of measurement artifacts, and their dependence on cell properties and measurement conditions, are elucidated. The analyses lead to comprehensive guidelines on how to conduct a trustworthy measurement and sensible data interpretation.

Absorbing semiconductor materials with different bandgaps are desirable for multi-junction solar cells. Thin-film $a\text{-SiGe}_x\text{:H}$ cells have been developed to accommodate an absorber material with an intermediate bandgap between that of $a\text{-Si:H}$ and $nc\text{-Si:H}$. Chapter 4 reports the development of $a\text{-SiGe}_x\text{:H}$ cells using mixed-phase $\text{SiO}_x\text{:H}$ materials in the doped layers. Bearing the band alignment in mind, the optimization of p- and n-type $\text{SiO}_x\text{:H}$ layers resulted in satisfying device performance. The use of $\text{SiO}_x\text{:H}$ p- and n-layers offers great flexibility when integrating the cell in a multi-junction solar cell.

Chapter 5 describes the development of quadruple-junction TFSSCs using four different absorber materials. The thin-film wide-gap $a\text{-Si:H}/$ narrow-gap $a\text{-Si:H}/a\text{-SiGe}_x\text{:H}/nc\text{-Si:H}$ solar cells promotes reasonable spectral utilization because of the descending bandgap along the direction of light incidence. The tunnel recombination junctions between the subcells have been optimized to ensure effective interconnections thus the proper functioning of the multi-junction device. Advanced light management, which involved the use of modulated surface textured front electrode, was arranged for enhancing the optical performance. These investigations reveal the potential of quadruple-junction TFSSCs.

Chapter 6 evaluates the benefit of multi-junction solar cells with different number of subcells. The gains and losses inherent in adding more subcells have been critically assessed from the optical and electrical points of view. The effects of optical reflection,

parasitic absorption, tunnel recombination junctions, and filtered illumination in multi-junction cells on the performance were investigated. In general, all types of losses increase with the number of subcells. Among them, the filtered illumination in the subcells can play a significant role in case of a large number of subcells. These results show that such comprehensive analysis helps to judge whether it is reasonable to develop a multi-junction solar cell with a certain structure.

Samenvatting

Dutch translation by Johan Blanker.

De directe omzetting van zonlicht is een essentiële energiebron in een duurzame toekomst. Een van de opties is het omzetten van zonne-energie naar electriciteit met zonnecellen met op silicium gebaseerde dunne lagen (DLS). Binnen de DLS zonnecellen hebben configuraties met een driedubbele junctie het hoogste omzettingsrendement tentoongespreid. Voortbordurend op deze state-of-the-art ontwerpen, wordt er in dit proefschrift een extra junctie toegevoegd en wordt de potentie en haalbaarheid van een zonnecelconfiguratie met een vier-juncties onderzocht.

In hoofdstuk 2 worden de initiële experimentele resultaten van een dergelijke vier-junctie DLS zonnecel gedemonstreerd. De gefabriceerde $a\text{-SiO}_x\text{:H}/a\text{-Si:H}/nc\text{-Si:H}/nc\text{-Si:H}$ zonnecellen hebben aantrekkelijke fill factors (FF) en exceptioneel hoge open klemspanningen (V_{OC}) tot wel 2.91 V, wat een hoge kwaliteit van materiaal en een hoge procesbehoudigheid suggereert. Met optische simulaties zijn de diktes van de verschillende lagen geoptimaliseerd en zijn de optische absorptie in deze lagen nauwkeurig in kaart gebracht. In deze eerste resultaten kwam naar voren hoe deze configuratie verbeterd kon worden met behulp van optische verbeteringen.

Binnen zonnecellen met meerdere juncties is het belangrijk de spectrale respons van de verschillende subcellen te kennen. Het accuraat meten van deze respons blijkt echter een behoorlijke uitdaging. In hoofdstuk 3 wordt het mechanisme achter een dergelijke meting geanalyseerd. Dit wordt gedaan met behulp van het modelleren van de opto-electrische eigenschappen van de subcellen en interacties tussen deze subcellen. De vorming van meet-artefacten wordt verklaard met een causale correlatie tot de ceileigenschappen en de meetcondities. De analyse leidt tot uitgebreide richtlijnen over hoe een betrouwbare meting uit te voeren en hoe de verkregen data te interpreteren.

Voor zonnecellen met meerdere juncties is het wenselijk absorberende halfgeleidermaterialen met verschillende bandgaps te gebruiken. $a\text{-SiGe}_x\text{:H}$ is een absorberend halfgeleidermateriaal met een bandgap tussen $a\text{-Si:H}$ en $nc\text{-Si}$. In hoofdstuk 4 wordt de ontwikkeling van $a\text{-SiGe}_x\text{:H}$ zonnecellen met een enkelvoudige junctie behandeld. In deze cellen is voor de gedoteerde lagen gebruik gemaakt van $\text{SiO}_x\text{:H}$ die in gemixte fase verkeert. Met inachtneming van de verschillende energetische bandstructuren, heeft de optimalisatie van de p-type en n-type $\text{SiO}_x\text{:H}$ lagen een bevredigende kwaliteit zonnecellen opgeleverd. Het gebruik van p-type en n-type $\text{SiO}_x\text{:H}$ lagen biedt erg veel flexibiliteit wanneer deze absorberende laag in een zonnecelconfiguratie met meerdere juncties wordt geïntegreerd.

Hoofdstuk 5 beschrijft de ontwikkeling van DLS zonnecellen met 4 juncties, waarbij van vier verschillende type absorberende lagen gebruik wordt gemaakt. De configuratie van brede bandgap $a\text{-Si:H}$ /smalle bandgap $a\text{-Si:H}/a\text{-SiGe}_x\text{:H}/nc\text{-Si:H}$ heeft een vrij efficiënte benutting van het zonnenspectrum. Dit omdat in deze configuratie iedere opeenvolgende subcel, vanaf de belichte zijde gezien, een afnemende breedte in bandgap heeft. De tunnel-recombinatie-overgangen tussen de subcellen zijn geoptimaliseerd om een zo effectief mogelijke interconnectie en daartoe goed functionerende multijunctie

zonnecellen te faciliteren. Geavanceerde lightmanagementmethoden, zoals het gebruik van gemoduleerde oppervlakte-texturen in de voor-electroden, zijn toegepast om de optische prestaties te verbeteren. Dit onderzoek onthult de potentie van DLS zonnecellen met vier juncties.

In hoofdstuk 6 worden de voordelen van DLS zonnecellen met verschillende hoeveelheden subcellen geëvalueerd. Er wordt vanuit zowel optisch als elektrisch oogpunt nauwkeurig vastgesteld wat voor winsten en verliezen inherent verbonden zijn met het toevoegen van een extra subcel. Dit onderzoek omsluit de effecten van optische reflectie, parasitische absorptie, de verschillen door extra tunnel-recombinatie-overgangen, en effecten van gefilterde belichting in de verschillende multi-junctie DLS zonnecellen. In het algemeen nemen alle type verliezen toe met de hoeveelheid subcellen. Het blijkt dat gefilterde belichting bij een grote hoeveelheid subcellen een belangrijke rol speelt. Deze resultaten laten zien dat een dergelijke grondige analyse van belang is om de juiste afweging te kunnen maken of het nuttig is om bepaalde configuraties van multi-junctie zonnecellen te ontwikkelen.

1

Introduction

1.1 The energy challenge

The global energy consumption by human activities increases along with the development of the civilization. Even in the ideal scenario that the growth of global energy demand may be reduced by the implementation of more energy-efficient technologies, the base of the consumption is still massive. For energy supply, fossil fuels have been the main contributor for more than a century and they still are today, but replacements are urgently needed. Not only the reserve of fossil fuels will be depleted, more importantly, burning fossil fuels releases greenhouse gases to the atmosphere and causes global warming. The urge to prevent the dramatic climate change, which can make the planet Earth inhabitable, led to the adoption of Paris Agreement [1] in 2015. The aim of the Paris Agreement is to hold the global temperature rise well below 2 °C above pre-industrial levels. Carbon-free, clean and renewable energy sources are one of the key elements for achieving this goal and a sustainable future.

1.2 Photovoltaics

The sun is an inexhaustible energy source for the humankind and the origin of most energy sources on Earth including the fossil fuels, wind, hydropower, etc. Logically, solar energy should be an indispensable part of the sustainable development, especially taking into account that most areas on the planet have access to a decent amount of solar irradiance. Solar energy can be harvested by converting it into electricity, or into thermal energy which may be used to drive electric generators.

The direct conversion of solar energy into electricity is done by a photovoltaic (PV) cell, also referred to as solar cell. The operation of solar cells is based on the photovoltaic effect. Upon exposure to light, mobile electric charge carriers are generated in a semiconductor material, which is the light absorbing region of a solar cell. The photo-generated carriers can then be separated in the solar cell, and the carrier separation leads to a difference in chemical potential between the two electrodes of the solar cell. This difference in potential, equivalent to an electrical voltage, can be used to perform work in an external circuit.

The working principle of a solar cell includes the generation, transportation, separation and collection of the electric charge carriers. When a photon is absorbed in a semiconductor material, the energy of the photon excites an electron and creates an electron-hole pair. The excited carriers, which are the negative charged electrons

and positively charged holes, will eventually recombine and lose their energy unless the two are separated. The carrier separation typically occurs at the interface between two materials with different work functions, such as a semiconductor p - n junction. At a p - n junction, electrons and holes are driven by the built-in electric field and move in two opposite directions. The two types of charge carriers are separated, ending up in two different materials. When a separated carrier arrives at a material in which it is the majority carrier, it becomes less likely to recombine.

Depending on the electronic quality of the materials, either a p - n or p - i - n junction can be used in a solar cell. The diffusion length, which is the average distance a carrier can travel in a material before it recombines, can be used to indicate the electronic quality of the material. When the electronic quality of a material is high, i.e. the carrier diffusion lengths are long, a solar cell structure based on p - n junction can be used, like the conventional crystalline silicon solar cells. In this type of solar cell, the photo-generated carriers can diffuse throughout the absorber material with little recombination. When a minority carrier reaches the p - n junction, it will be moved by the built-in electric field into the other side of the junction, so the carrier separation is achieved. When the electronic quality of a material is relatively poor, the carrier diffusion length is too short that most photo-generated carriers will recombine before they can diffuse to the interfaces for separation. In such cases, a solar cell structure based on p - i - n junction can be used. In a p - i - n junction, a layer of intrinsic material (i -layer) is sandwiched between a p -layer and an n -layer. The intrinsic material is less defective and has lower carrier concentration compared to the corresponding doped materials, so the charge carriers in it have a lower recombination rate. Therefore, the intrinsic material can be made relatively thick to serve as the absorber of the solar cell. As a result of the electronic band structure of the p - i - n junction, an electric field is built across the i -layer and it strengthens the directional carrier transport in the layer. Under the effect of the electric field, the photo-generated holes and electrons in the i -layer drift towards the p - and n -layers, respectively. They are separated at the p - i and i - n interfaces, and arrive at the p - and n -layers where they become the majority carriers in the materials.

Many different types of PV technologies have been developed in the past decades. They are usually recognized by the semiconductor material used to form the device. Solar cells and modules based on crystalline silicon dominate the market because of their high and stable efficiencies and competitive prices. Also, there are three main thin-film PV technologies commercially available: Cadmium telluride (CdTe), copper-indium-gallium-selenide (CIGS), and thin-film silicon (widely known as amorphous silicon), in the order from high to low module efficiency. Solar cells using III-V semiconductor materials have delivered so far the highest efficiencies among all PV technologies, although they are expensive to produce and are mainly used in space applications or in terrestrial applications with the use of solar tracker and concentrator. Meanwhile, the organic solar cells, dye sensitized solar cells, perovskite solar cells, and quantum dot solar cells have been extensively studied in laboratories because of their potential to be manufactured by an inexpensive and large-scale roll-to-roll process. Notably, the record efficiency of perovskite solar cells has skyrocketed since the end of 2000s, from 3.8% [2] to more than 22% [3], demonstrated a promising technology for low-cost, high-efficiency photovoltaics.

In applications, multiple solar cells can be connected to form a solar module in order to provide the voltage and current suitable for practical use. Solar modules together with other components can form a PV system to fulfil the functions for certain applications. For example, an inverter is needed to convert the direct current (DC) into alternating current (AC) for common household appliances; a battery can be used to store the electricity, etc.

1.3 Thin-film silicon PV

In 1975, W.E. Spear and P.G. Le Comber realized the substitutional doping of amorphous silicon [4]. Soon after that, D.E. Carlson and C.R. Wronski reported in 1976 the first ever thin-film amorphous silicon solar cell [5]. The research field of thin-film silicon-based photovoltaics were kicked off.

1.3.1 Basics

Thin-film silicon-based solar cells (TFSSCs) use thin layers of silicon-based amorphous or nanocrystalline materials to form the solar cell. The device structure of TFSSCs is a semiconductor *p-i-n* junction. As it was explained, the carrier transport in a *p-i-n* junction relies on the drift mechanism. Very thin layers of p-type and n-type materials, of which the thickness is typically in the range of 20 nm, are at the two sides to build up an electric field across the intrinsic layer. Because the intrinsic materials have lower defect densities and lower majority carrier concentrations than the respective doped materials, the charge carriers in the i-layer are less likely to recombine and lose their energy. Therefore, an intrinsic material is used as the absorber of the solar cell, and the thickness of this i-layer can be much thicker than the doped layers. Driven by the electric field, the electrons and holes generated in the i-layer can drift in two opposite directions towards the n- and p-layers, respectively, and eventually be collected there. Hydrogenated amorphous silicon (a-Si:H) and hydrogenated nanocrystalline silicon (nc-Si:H, also often referred to as hydrogenated microcrystalline silicon, $\mu\text{c-Si:H}$) are the most common absorber materials used in TFSSCs. Restricted by the electronic quality of the materials, usually the i-layer is made within 1 μm in case of a-Si:H, and no more than 5 μm in case of nc-Si:H.

Plasma-enhanced chemical vapor deposition (PECVD) is the most common technique used for depositing the p-, i-, and n-layers in TFSSCs. The intrinsic a-Si:H or nc-Si:H material is formed using silane as the main gas precursor. The thin layers of p-type and n-type materials are usually deposited by adding boron- or phosphorus-containing precursor to the gas mixture, respectively. All these intrinsic and doped materials are referred to as the silicon alloys used in TFSSCs. Because in the absorber layer the holes have a shorter lifetime than the electrons, most TFSSCs are made in a way that the sunlight enters the solar cell from the p-side. Since a large portion of the photons is absorbed right after they enter the i-layer, this sequence of layers gives the holes a shorter distance, on average, to travel to the p-layer. On the other hand, the sequence of cell deposition can start either from the back side (substrate or *n-i-p* configuration), or from the front side where the light enters the device (superstrate

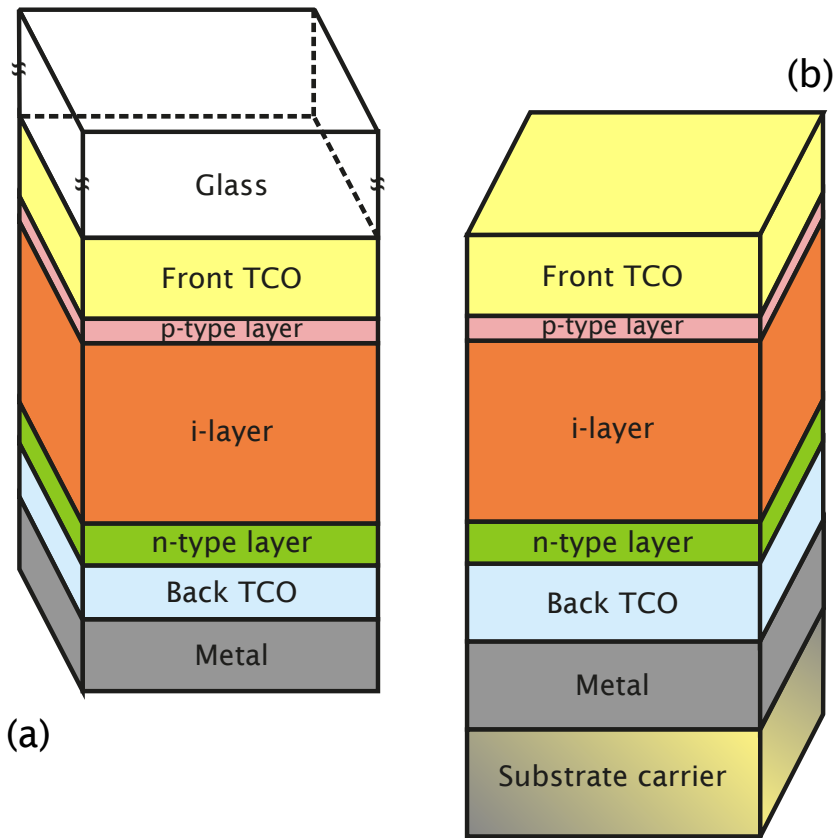


Figure 1.1: A simplistic structure of a TFSSC in (a) superstrate or (b) substrate configuration [6].

or $p-i-n$ configuration). The schematics in Figure 1.1 illustrate these two basic structures of TFSSCs. In $p-i-n$ configuration, the mechanical carrier (superstrate) has to be transparent because it is the first layer facing the incident light.

The separated charge carriers in p - and n -layers need to be transported laterally to the electrical terminals where the connections between the cell and the external circuit are made. While the $p-i-n$ junction realizes the carrier separation and collection in the transverse direction, the electrical resistance of the p - and n -layers are too large to conduct the carrier transport in the lateral direction, where the distance could be a few millimetres. Therefore, more conductive materials are used in the electrodes to transport the collected carriers to the external circuit. The electrode at the front side should absorb as little light as possible, because only the carriers photo-generated in the absorber layer can result in usable electricity. The energy of the photons absorbed in other layers is lost. For this reason, transparent conductive oxide (TCO) materials are used in the front electrode to satisfy the dual requirements of optical transparency

and electrical conductivity. The back electrode can be made of either TCO or metal, or a combination of the two.

The absorber materials for TFSSCs cover a big family of silicon-based alloys. a-Si:H is one of the earliest studied materials obtained by radio-frequency glow discharge [7], [8]. Optically, a-Si:H behaves similarly to a semiconductor with a direct bandgap. The optical bandgap is typically in the range of 1.7 to 1.8 eV. It strongly absorbs the light with photon energy higher than its bandgap, but is mostly transparent to the wavelengths longer than 800 nm. A a-Si:H layer of a few hundred nanometers is enough to capture most of the relevant photons. On the contrary, nc-Si:H [9]–[11] is a very different absorber material from a-Si:H. nc-Si:H has an indirect bandgap of 1.12 eV. On the one hand, the narrower bandgap allows nc-Si:H to absorb the near-infrared light, and thus utilize more photons than a-Si:H does. On the other hand, the indirect bandgap results in much weaker absorption coefficient and much larger thickness needed to have adequate optical absorption. The thickness of nc-Si:H absorber layer can vary from 1 to 5 μm depending on the light management of the device structure. The practical maximum of the thickness is decided by the electronic quality of the absorber material. Interestingly, by alloying the atoms of other elements with silicon and hydrogen, various bandgaps rather than that of a-Si:H or nc-Si:H can be obtained. Having smaller atoms incorporated in the silicon matrix, hydrogenated amorphous silicon carbide (a-SiC_x:H) [12], [13] and hydrogenated amorphous silicon oxide (a-SiO_x:H) [14], [15] can exhibit a larger bandgap than that of a-Si:H. Similarly, alloying with the large Ge atoms leads to the smaller bandgaps of hydrogenated amorphous silicon germanium (a-SiGe_x:H) [16]–[18] and hydrogenated nanocrystalline silicon germanium (nc-SiGe_x:H) [19], [20], compared to a-Si:H and nc-Si:H, respectively. The variety of absorber materials provides great flexibility for different applications in TFSSCs.

A noteworthy phenomenon in TFSSCs is the light-induced degradation (LID), also widely known as the Staebler–Wronski effect. Soon after the invention of thin-film a-Si:H solar cells, D.L. Staebler and C.R. Wronski discovered that the long exposure of a-Si:H to light decreased the conductivity of the material [21]. In solar cells consisting of amorphous absorber materials such as a-Si:H, a-SiGe_x:H, a-SiO_x:H and a-SiC_x:H, this degradation results in the deterioration of device performance. The most noticeable effect on the external parameters is the degradation of the FF , which can be more than 10% absolute. Next to the FF , the decline in J_{SC} is also obvious. With the material quality being the same, a solar cell with a thicker layer of amorphous absorber suffers more severely from the LID. Overall, the energy conversion efficiency can decrease by 10 to 30% from the initial state after prolonged light exposure. Therefore, whenever the performance of a solar cell comprising an amorphous absorber is reported, it is necessary to distinguish between the initial and the stabilized performance. Although the nature of LID has not yet been unambiguously clarified, it is generally ascribed to the creation of metastable defects in the amorphous materials [22], [23]. As a consequence, a major part of the degradation is reversible by an annealing process at a temperature over 150 °C [21].

1.3.2 Light management

Ideally, the absorber layer of a solar cell should be sufficiently thick to absorb all the relevant photons, especially for the materials with weak absorption coefficient like nc-Si:H. Nonetheless, there are several reasons to make the absorber layers in TFSSCs thin. Firstly, the carrier separation in TFSSCs relies on the drift mechanism, so it also becomes less efficient as the intensity of the electric field decreases with the increase in absorber thickness. As a result, lesser electrical performance is expected from TFSSCs with thick absorber layers. Secondly, a thicker layer of amorphous silicon-based absorber will experience a higher extent of LID, meaning a larger difference between the initial and stabilized efficiencies. Furthermore, the manufacturing cost of thin-film silicon-based solar cells and modules increases with the deposition time, so thick layers in the device will be translated into a high price and thus less competitive product. With all considered, the absorber layer should be both thick and thin at the same time. These contradictory requirements suggest that a compromise needs to be made between the two extremes to find the optimum structure. To achieve the best out of this compromise, researchers have been looking into different ways of light management to create TFSSCs which are electrically-thin, but optically-thick. In other words, light management is used to create solar cells which absorb much light with little material mass.

An essential aspect of the light management in TFSSCs is to increase the optical path length of light within an absorber layer with a limited thickness, for the light which is weakly absorbed by the material. If we define the optical path length as the geometrical distance along which the light propagates in the absorber material, in a simple planar multi-layered structure, the average optical path length is not much more than the thickness of the layer. Even with a perfect light reflector on the back side, the optical path length is merely two times the thickness. In order to enhance the absorption, light scattering can be introduced to increase the optical path length in the medium. Theoretically, E. Yablonovitch and G.D. Cody determined the maximum enhancement of light intensity in a slab of weakly absorbing dielectric sandwiched by the vacuum [24]. Presuming no reflection on the front side, full randomization of light in the medium and perfect reflection on the back side, the upper limit of the enhancement was derived as $4n^2$, where n is the refractive index of the dielectric medium. For crystalline silicon or nc-Si:H, it is an enhancement around 50 near the wavelengths corresponding to the bandgap energy.

Another fundamental requirement for the light management is to increase the photons capable of reaching the absorber layer. Under a certain incident illumination, this requirement implies the reduction of optical losses. On the front side, the reflection of light should be minimized because the reflected photons have no chance to reach the absorber layer. Meanwhile, because the absorption occurring outside the absorber layer (parasitic absorption) does not contribute to the output of electrical power, all materials in the solar cell except the absorber should be as transparent as possible in the wavelength range which the absorber material is absorptive.

In the fabrication of TFSSCs, the light-scattering techniques commonly seen in research include interfaces with random roughness, plasmonic scatterers, and periodic diffraction gratings. A surface with random roughness is introduced onto mostly

the substrate carrier, before the deposition of silicon alloys. Such roughness is to a certain extent inherited along the deposition of the subsequent layers, creating multiple textured interfaces in the solar cell. Each textured interface is effective in scattering the impinging light when the wavelength of the light is similar to the feature size of the random roughness, and when the difference between the refractive indices of the two adjacent media is great. The textured surface on a substrate carrier can be generated either by the anisotropic etching of a surface [25]–[31], by different types of lithography techniques [32]–[34], or as the native morphology of a deposited layer [35]–[39]. The application of plasmonic scatterers in solar cells [40]–[53] is often at the back reflector. This is because the metallic nanostructures, which are necessary for the excitation of surface plasmons, will block a part of the incident light when placed in the front of the solar cell, or induce surface recombination when embedded in the middle of the absorber layer [53]. Metal nanoparticles with the proper size and density on the back side of a solar cell can scatter the unused low-energy photons into broad angles without introducing significant parasitic losses. Diffraction gratings are periodic photonic structures [6], [54]–[65] which can couple the incident light into discrete guided modes and prolong the effective optical path length in a medium. Typically, the interactions between the light and the periodic structures are wavelength-selective, and the enhancement of light absorption can go beyond the $4n^2$ limit at some specific wavelengths [55]. With the advances in various lithography technologies, many kinds of 1-D, 2-D and 3-D gratings can be fabricated to facilitate the desired light-trapping scheme.

Besides reducing the reflection and parasitic absorption and enhancing the effective absorption, light management may also involve the improvement of spectral utilization of a solar cell. Different parts of the solar spectrum can be utilized by different absorber materials in a solar cell to improve the conversion efficiency. Spectral utilization will be further explained in Section 1.4 with the introduction to multi-junction solar cells.

1.3.3 Motivations for research

The research and development of TFSSCs were once driven by the advantage of low manufacturing cost compared to other PV technologies. Although such argument is no longer valid since the price of monocrystalline silicon and polycrystalline silicon solar modules dropped dramatically in the late 2000s, the thin-film silicon-based PV technology still has a unique set of features which makes it interesting for continued developments. First of all, TFSSCs as a source of renewable energy are sustainable and environmentally friendly because of the great abundance and non-toxicity of the materials being used. Figure 1.2 shows the abundance of elements in Earth's crust. It can be seen in the graph that the main elements in TFSSCs, including Si, H, B, P, O, C, Zn and Al, are all abundant on the planet Earth. The solar modules using such abundant while mostly non-toxic materials have a greater feasibility of mass-production. Also, the energy payback time of TFSSCs is relatively short due to the low thermal budget in the manufacturing process. Because the functional materials of the device are in the form of thin films, flexible [67], [68] and/or semi-transparent [69] thin-film silicon-based solar modules can be made on flexible and/or transparent substrate like glass, metallic foils, plastic or even paper. The versatility

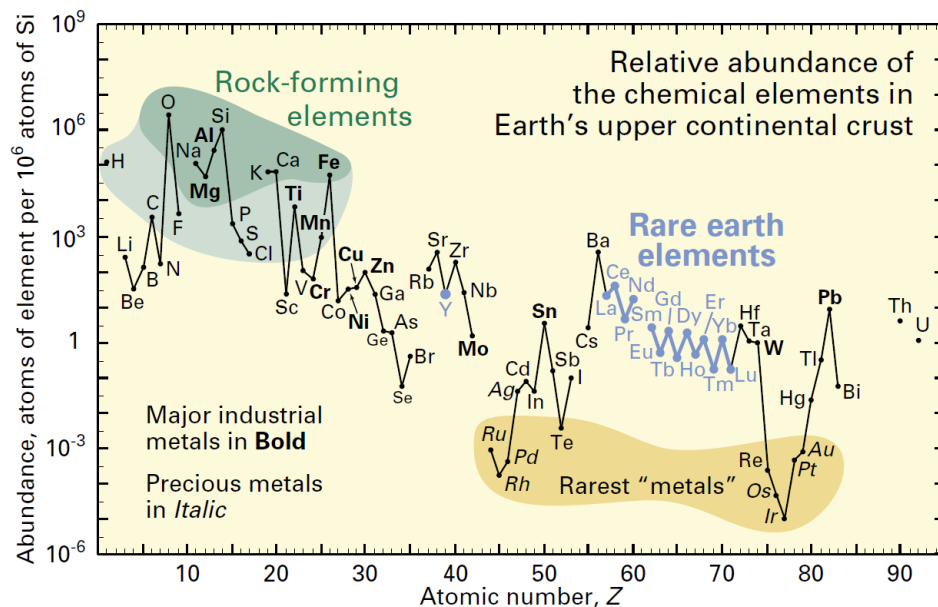


Figure 1.2: Abundance of the chemical elements in Earth's crust [66]. All elements used in TFSSCs can be found in the upper part of the graph, showing the great abundance of the involved materials.

enables various special applications such as building-integrated photovoltaics (BIPV) [69], [70] and consumer wearables. The most superior feature of thin-film silicon-based PV technology is arguably its ability to manufacture a module of an ultra-large area. As shown in Figure 1.3, for most types of PV cells/modules, the efficiencies of the large-area devices are systematically lower than the small-area counterparts because of the technical difficulties to control the fabrication processes at a uniformly high quality over a large area. This is not the case for TFSSCs. The efficiencies exhibited by the best lab cell and the best large-area module in the a-Si:H/nc-Si:H tandem configuration are nearly identical, that is made possible by the mature industrial PECVD processes and the design of electrical contacts.

The low efficiency of TFSSCs is the principal drawback withholding the technology from being adopted by applications. To lift the competitiveness of this technology, cost reduction is required and it can be done by scaling up the manufacturing capacity. Even so, improving the energy conversion efficiency of the solar modules is still of utmost importance, since the overall cost of a module is directly related to the performance of the PV cells.

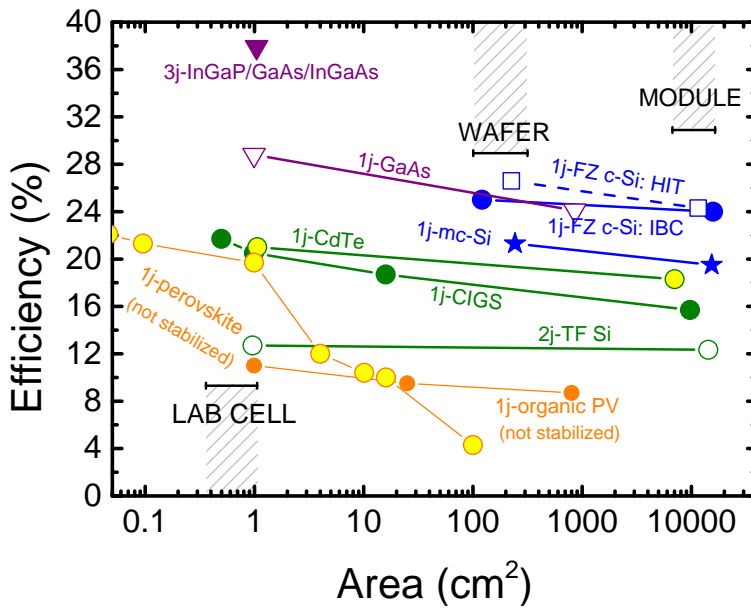


Figure 1.3: Record energy conversion efficiencies from different PV technologies as a function of the area of the PV cells or modules [71]. In general, the efficiencies decrease with the increase in area. A notable exception is TFSSCs (2j-TF Si, which means a-Si:H/nc-Si:H tandem TFSSC).

1.4 Multi-junction solar cells

1.4.1 Concept

Solar cells use absorber materials which are semiconductor. A photon excites an electron in the absorber material from the valence band to the conduction band and generates a electron-hole pair. A minimum energy of the photon, which is equal to the bandgap energy of the semiconductor material, is required to realize the excitation. The carriers at a high-energy state, however, will relax to the band edge of the conduction or valence band and release the excess energy as heat. The heat cannot provide electrical power so it is considered a loss in PV cells, and is referred to as the thermalization loss. On the other hand, photons with energy lower than the bandgap are not able to excite charge carriers in the absorber material. These photons are responsible for the non-absorption loss of the incident power. The thermalization and non-absorption losses originate from the misfit between the energy profile of the incident spectrum and the bandgap of the semiconductor material. These two together are referred to as the power losses in PV cells caused by spectral mismatch.

Bearing the spectral mismatch in mind among with other considerations, W. Shockley and H.J. Queisser calculated the theoretical limit for the energy conversion efficiency of a solar cell consisting of a single p - n junction [72]. This detailed balance limit suggested the upper efficiency limit for a single-junction solar cell is 30 %, assuming the sun as a blackbody with the temperature of 6000 K. This is known as the Shockley-Queisser limit. A recent calculation using AM1.5G solar spectrum indicated a limit of 33.7 % with an optimal absorber bandgap of 1.34 eV [73], under the modern standard test conditions.

Several concepts were proposed to circumvent the Shockley-Queisser limit, and two of them have proved particularly successful. By concentrating the sunlight, the solid angle subtended by the sun at the solar cell is effectively increased. The enhanced irradiance boosts the photocurrent in the device, while the dark current remains the same at a certain temperature. It results in improved open-circuit voltage and fill factor, and thus higher efficiency. Another method deals with the issue of spectral mismatch. Multiple p - n or p - i - n junctions can be stacked on top of each other to form a multi-junction solar cell. Each junction is a subcell of the multi-junction cell and contains a semiconductor absorber with a different bandgap. Starting from the surface of light incidence, the subcells are positioned in the order that the bandgap of the absorber materials is descending along the direction of forward propagation of the incident light. In this way, the high-energy photons are absorbed in the material with the largest bandgap, resulting in little thermalization loss and high output voltage. The remainder of the solar spectrum, which comprises the lower-energy photons, passes through the top subcell and reaches the subsequent subcell(s). Such process repeats in the subcells, each of which has an absorber with a bandgap smaller than the previous one. As a result, the sunlight is sequentially utilized by different subcells depending on the photon energy. The losses from spectral mismatch are suppressed in a multi-junction solar cell and the output voltage is maximized with the same amount of photo-generated carriers.

The detailed balance limit for the efficiency of the unconstrained multi-junction solar

cells, in which the operation point of each subcell is independent of the others, was calculated at 55.8 %, 63.8 %, 68.7 %, and 86.8 % for the cells containing two, three, four, and infinite number of subcells, respectively, under maximum solar concentration [74]. The unconstrained multi-junction solar cell requires separate electrical contacts for each subcell so its fabrication becomes impractical in case of a large number of subcells. A more common and practical multi-junction structure has two electrical contacts (terminals) at both ends of the device. In two-terminal/monolithic multi-junction solar cells, all component subcells are in a series connection so they are constrained to operate at the same level of current. This current-matching requirement slightly reduces the efficiency limit to 55.5 %, 63.2 %, 67.9 %, and 86.8 % in the cases of two, three, four, and infinite number of subcells, respectively [74].

1.4.2 Multi-junction TFSSC and its status

The thin-film silicon-based PV technology has both the capabilities and motives for developing multi-junction cells. A great variety of absorber materials can be obtained with bandgaps ranging from 0.95 eV [20] to 2.24 eV [75]. The extensive collection of materials opens a big room for the design of multi-junction structures. Depending on the desired number of subcells and the light-trapping scheme, a combination of several absorber materials with optimum bandgaps might be chosen. For the sake of improving device performance, the study of multi-junction concept is of significant interest to TFSSCs. Not only the spectral mismatch can be reduced, but the multi-junction concept also enables enhancement of light absorption in TFSSCs by allowing a large total thickness of absorber layers. While having a large total thickness, individually the absorber layers of the subcells can be made reasonably thin. Compared to a single-junction cell with a thick absorber layer, splitting the light absorption into multiple relatively thin subcells improves the carrier separation and mitigates the light-induced degradation of amorphous materials.

The study of multi-junction thin-film silicon-based solar cells can be traced back to the late 1970s, soon after the invention of the amorphous silicon solar cell. Researchers experimented with the idea of stacking up a few amorphous silicon or amorphous silicon germanium cells to create a high output voltage [76], [77]. These multi-junction structures, comprising up to five *p-i-n* junctions, helped to realize a large total absorber thickness and a high photocurrent while maintaining a satisfactory electrical performance. Despite the large number of subcells, however, these cells were mostly made of the same absorber material and did not improve from a single-junction device in terms of the spectral mismatch. It was the case until the introduction of nanocrystalline silicon in 1990s. The narrow bandgap of the material extends the active spectrum of TFSSCs to longer wavelengths up to 1100 nm. It opens some sensible options for creating multi-junction solar cells. The a-Si:H/nc-Si:H double-junction (Micromorph) [78] and the a-Si:H/a-SiGe_x:H/nc-Si:H triple-junction structures provide favorable spectral utilization because of the optimal combination of absorber bandgaps. On the other hand, the emphasized use of nc-Si:H in the a-Si:H/nc-Si:H/nc-Si:H triple-junction cells gives an alternative solution for achieving high stabilized efficiencies. To date, the highest energy conversion efficiencies in thin-film silicon-based PV come from the triple-junction configuration. In contrast to the best performing single-junction nc-

Si:H cell with an efficiency of 11.8% [79], a a-Si:H/a-SiGe_x:H/nc-Si:H triple-junction cell established the highest initial efficiency of 16.3% [80], while the highest stabilized efficiency of 14.0% was achieved by a a-Si:H/nc-Si:H/nc-Si:H triple-junction cell [81]. Evidently, the multi-junction approach has been a successful means to improve the performance of TFSSCs.

1.5 Goals of the work

The goal of this thesis is to explore the potential of quadruple-junction thin-film silicon-based solar cells. At the time this thesis project began, both the record initial efficiency and record stabilized efficiency of TFSSCs were held by solar cells in triple-junction configuration. Meanwhile, it was suggested by simulations that a TFSSC with four subcells using different absorber materials could potentially reach an (initial) efficiency near 20% [82]. From a-SiO_x:H [15], [75] to nc-SiGe_x:H [83], the functionality of thin-film silicon-based absorber materials with diverse values of bandgap had been successfully demonstrated in various devices. Mixed-phase SiO_x:H materials had exhibited their versatility to serve as doped layers with multiple optical and electrical functions [29], [80], [84]–[90]. The concept of modulated surface texture had been proposed to efficiently scatter light with wavelengths in a broad spectrum [29], [38], [90]–[95]. High-mobility TCO materials offered an additional means to enhance the infrared response of solar cells [96], [97]. All of these developments called for an adventure of experimentally realizing a quadruple-junction TFSSC. This thesis aims to answer the questions: Is it feasible to fabricate a multi-junction TFSSC as complex as having four subcells? If so, how well can an optimized quadruple-junction TFSSC perform, and is it superior to the triple-junction?

1.6 Outline of the thesis

This thesis is organized in the following way: Chapter 1 (this chapter) provides a basic background on photovoltaics and a brief introduction to the multi-junction thin-film silicon-based solar cells. Chapter 2 reports the preliminary attempt of fabricating quadruple-junction TFSSCs comprising three different absorber materials. Such initial result and experience shed light on the design rules of high-performance quadruple-junction cells. Dealing with the complicated devices, even the routine measurements become a challenging task. Chapter 3 discusses in-depth the spectral response measurement of multi-junction solar cells and the accompanying artifacts. Hydrogenated amorphous silicon germanium is a critical component to achieve a quadruple-junction TFSSC with four different absorber materials and optimal spectral utilization. Chapter 4 covers the development of solar cells using this absorber material. Chapter 5 presents the experimental efforts on the fabrication and optimization of quadruple-junction TFSSCs with non-repeating absorbers, tackling the issues of tunnel recombination junctions and light management. Based on all the learned experience, Chapter 6 investigates the possible pitfalls of multi-junction solar cells with a large number of subcells. It gives insights for evaluating the actual benefits of making multi-junction

cells so as to determine the most reasonable device structure. Chapter 7 summarizes the conclusions of this thesis and provides an outlook.

1.7 Contributions to the field

This thesis is dedicated to the field of multi-junction thin-film silicon-based solar cells, and has contributed to the studies in several ways.

The experimental realization of quadruple-junction TFSSCs containing three or four different absorber materials was reported. The investigated absorber combinations were a-SiO_x:H/a-Si:H/nc-Si:H/nc-Si:H and wide-gap a-Si:H/narrow-gap a-Si:H/a-SiGe_x:H/nc-Si:H. It was demonstrated that this complicated type of device can be made in a way such that the cell performance did not show any significant electrical losses. Not only the quadruple-junction cells delivered ultrahigh photo-voltage up to 2.91 V, but they were also used to experiment a way to further reduce the losses from spectral mismatch. Having deployed the state-of-the-art materials including In₂O₃:H and mixed-phase doped SiO_x:H, and optoelectrical designs such as the modulated surface texture, the efficiency potential of quadruple-junction TFSSCs was revealed from the experimental perspective, complementary to suggestions in literature based on simulations.

A critical evaluation on the benefits and drawbacks of multi-junction solar cells was performed. Many optical and electrical loss mechanisms accompanying the formation of multi-junction cells were taken into account. With the practical issues considered, the performance potential of various multi-junction structures can be compared in a way which is as fair and as realistic as possible. Such analysis can be used to define the most promising multi-junction structures and avoid the unnecessary efforts on developing over-complicated devices. In case of TFSSCs, it was determined that the a-Si:H/a-SiGe_x:H/nc-Si:H triple-junction configuration has the highest potential in terms of initial efficiency.

The mechanism of the spectral response measurement of multi-junction solar cells was studied comprehensively. Having examined the individual response of the subcells and the interactions between them, the principle of how the cell properties and measurement conditions impact the correctness of the results was illustrated. The modeling method as well as the explanation is broadly applicable to various multi-junction solar cells from different PV technologies. In addition to facilitating more reliable measurements and more accurate data interpretation, the more important contribution, arguably, is to alarm the research community of how vulnerable and deceptive this measurement can be.

2

Quadruple-junction thin-film silicon-based solar cells with high open-circuit voltage

This chapter was published in *Applied Physics Letters* [98].

Abstract

We have fabricated a-SiO_x:H/a-Si:H/nc-Si:H/nc-Si:H quadruple-junction thin-film silicon-based solar cells (4J TFSSCs) to obtain high spectral utilization and high voltages. By processing the solar cells on micro-textured superstrates, extremely high open-circuit voltages for photovoltaic technology based on thin-film silicon alloys up to 2.91 V has been achieved. Optical simulations of quadruple-junction solar cells using an advanced in-house model is a crucial tool to effectively tackle the challenging task of current matching among the individual subcells in such devices. After optimizing the optical design of the device and the absorber thicknesses, a power conversion efficiency of 11.4% has been achieved. The open-circuit voltage, short-circuit current density and fill factor were 2.82 V, 5.49 mA/cm² and 73.9%, respectively. Based on this demonstration, strategies for further development of highly efficient 4J TFSSCs are proposed.

2.1 Introduction

Spectral mismatch is one of the major loss mechanisms for energy conversion in photovoltaic devices. When $E_{\text{ph}} > E_{\text{g}}$, where E_{ph} is the energy of incident photon and E_{g} is the bandgap energy of absorber material, the energy of photon in excess of the band gap ($E_{\text{ph}} - E_{\text{g}}$) is lost via thermalization and cannot be converted into electricity. When $E_{\text{ph}} < E_{\text{g}}$, the absorber is transparent to the photon and the energy of the photon cannot be utilized as well. The effect of spectral mismatch on photovoltaic devices is evaluated with Shockley-Queisser limit. It concludes that the upper efficiency limit of solar cells consisting of a single semiconductor p - n junction is 33 % for an absorber with an ideal band gap of 1.34 eV [72], [74]. On the one hand the band gap of absorber should be high to reduce the thermalization loss, while on the other hand it should be low to make use of a broader part of the solar spectrum. In order to overcome this problem, stacking multiple junctions in series is the most widely used approach. In this approach, photons are supposed to be absorbed in different junctions according to their energy and the bandgap of the absorber material. Multi-junction solar cells promise smaller thermalization losses and thus a higher output voltage, as well as the utilization of long-wavelength photons. The performance of multi-junction cells depends on the bandgaps of absorber materials. With absorbers having optimal bandgaps, the corresponding efficiency limit is raised to 46 %, 51 % and 56 % for double-, triple- and quadruple-junction cells, respectively [74], [99]. Ideally, the more junctions with different bandgaps are used, the higher efficiency can be achieved.

Thin-film silicon-based solar cells (TFSSCs) have been featuring the potential for low-cost and large-area manufacturing. Using raw materials which are highly abundant in the Earth's crust makes TFSSCs as a favorable source of renewable energy. Improving its relatively low power conversion efficiency is the main challenge to stay competitive with other photovoltaic technologies. Examining the state-of-the-art TFSSCs, the record efficiency increases from 11.0 % in single-junction hydrogenated nanocrystalline silicon (nc-Si:H) cells [62], [100], [101] to 12.6 % in hydrogenated amorphous silicon (a-Si:H)/nc-Si:H tandem cells [102], [103]. Both the record initial and stabilized efficiency of TFSSCs were achieved on triple-junction devices, which were 16.3 % in a-Si:H/hydrogenated amorphous silicon germanium (a-SiGe_x:H)/nc-Si:H structure with short-circuit current density (J_{SC}) of 9.43 mA/cm² [80] and 13.4 % in a-Si:H/nc-Si:H/nc-Si:H structure with J_{SC} of 9.52 mA/cm² [104], respectively. (The record stabilized efficiency was 13.4 % at the time this article was published in *Applied Physics Letters* in 2014. Such record was later surpassed. A more up-to-date record is 14.0 % [81], reported in 2016 by Sai et al., also with a a-Si:H/nc-Si:H/nc-Si:H triple-junction cell.) It is evident that the efficiency of TFSSCs could be improved by adding more junctions into a solar cell.

Besides better spectral utilization, multi-junction TFSSCs benefit from mitigated light-induced degradation owing to thinner amorphous absorbers. In case of a-Si:H/nc-Si:H/nc-Si:H triple-junction cells, the two consecutive nc-Si:H subcells do not contribute to better spectral utilization, but promote more efficient light absorption and carrier transport in the device. From electrical point of view, the reduced operation current in such devices (e.g. half in a tandem, one-fourth in a quadruple-junction cell) comparing with single-junction cells leads to less parasitic electrical loss. A lower

requirement of series resistance in the device means that the transparent conductive oxide (TCO) layer can be made thinner and more transparent to reduce the parasitic optical absorption [33]. Therefore, making quadruple-junction (4J) cells is considered a sensible option for further development of highly efficient TFSSCs. A theoretical study based on optical simulation [82] revealed that an initial efficiency of 19.8% can be achieved with a 4J TFSSC with hydrogenated amorphous silicon oxide ($a\text{-SiO}_x\text{:H}$), $a\text{-SiGe}_x\text{:H}$, $nc\text{-Si:H}$ and hydrogenated nanocrystalline silicon germanium ($nc\text{-SiGe}_x\text{:H}$) as the absorbers in the four component junctions. In that study Lambertian scattering at internal interfaces was assumed and resulted in a J_{SC} of 8.72 mA/cm^2 . The simulation study demonstrated the potential of thin-film technology for being competitive with the mainstream silicon wafer-based or other thin-film photovoltaic technologies. So far, not many experimental results on 4J TFSSCs have been reported since Yang et al. demonstrated in 1985 an $a\text{-Si:F:H/a-Si:F:H/a-Si:F:H/a-Si:Ge:F:H}$ 4J cell with an efficiency of 11.0% [77]. In this device thick amorphous layers were used and the device utilized a narrow range of the solar spectrum up to 850 nm that was limited by the use of $a\text{-Si:Ge:F:H}$ absorber.

In this work, we present experimental results of 4J TFSSCs consisting of $a\text{-SiO}_x\text{:H/a-Si:H/nc-Si:H/nc-Si:H}$ absorbers with open-circuit voltage (V_{OC}) up to 2.91 V and solar spectrum utilization up to 1100 nm. Optical simulations were used to design the absorber thicknesses in such a way that light absorption is appropriately distributed in the four junctions. By optimizing the optical design of our 4J cells an initial efficiency of 11.4% has been achieved.

2.2 Experimental

The 4J TFSSCs were fabricated on textured glass substrates in $p\text{-i-n}$ configuration. The surface of the textured glass on which the layers were deposited resembled crater-like features with lateral correlation length around $6\text{ }\mu\text{m}$ and aspect ratio of 0.1. The micro-textured substrate was chosen to ease the defect control in this first demonstration of such device. The smooth morphology of substrate can avoid the formation of defective areas during $nc\text{-Si:H}$ deposition so that guarantee high material quality. The glass texturing process has been reported elsewhere [29]. 90 nm of tin-doped indium oxide (ITO) was deposited as part of the front contact of the solar cells by RF magnetron sputtering. The $p\text{-i-n}$ junctions of the cells were deposited by radio-frequency (13.56 MHz) plasma-enhanced chemical vapor deposition (RF-PECVD), except for the intrinsic $nc\text{-Si:H}$ absorber that was made using PECVD with a frequency of 40.68 MHz. A stack of Ag/Cr/Al with thickness of 300/30/500 nm was evaporated as back reflector and electrode, with a pattern defining the cell area ($4 \times 4\text{ mm}^2$). After the depositions, edge isolation of the cells was performed by reactive ion etching of silicon and silicon alloys outside the cell areas. The fabrication was finished with a thermal annealing step at $170\text{ }^\circ\text{C}$ for two hours. Relevant single-, double-, and triple-junction cells were co-deposited for obtaining information about the quality of the deposition process and the component subcells.

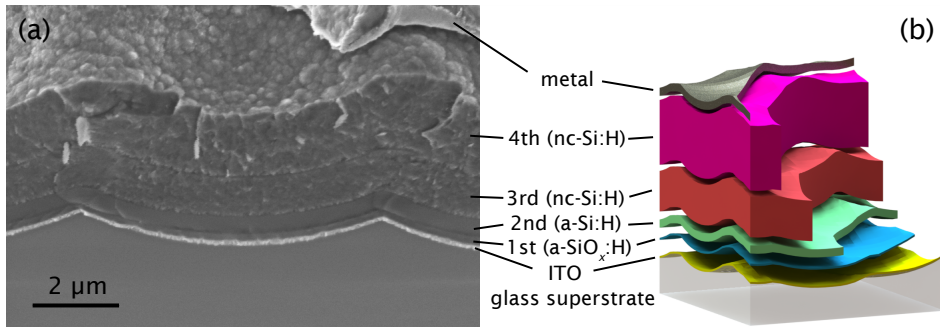


Figure 2.1: (a) SEM image exhibiting the cross section of a 4J cell in *p-i-n* configuration with a-SiO_x:H/a-Si:H/nc-Si:H/nc-Si:H absorber layers on top of textured glass substrate. Division of the subcells is indicated. The image acquisition was performed at a tilted angle of 45°. (b) Simplified structure of the studied 4J TFSSC.

2.3 Initial demonstration

Our 4J cells were initially fabricated by stacking an additional top subcell with a-SiO_x:H absorber [75] on a typical triple-junction a-Si:H/nc-Si:H/nc-Si:H cells. The bandgap of a-SiO_x:H (2.1 eV) is higher than that of a-Si:H (1.8 eV). The shift towards a higher bandgap offers a better spectral utilization in a-SiO_x:H/a-Si:H/nc-Si:H/nc-Si:H 4J cells. The properties of the intrinsic nc-Si:H absorbers in the third and fourth subcells were not intentionally differentiated, so they may share the same bandgap energy. In such configuration, two subcells with identical absorber material do not suppress the thermalization loss but provide a reasonable distribution of photo-generated carriers among all the subcells, since they are connected in series and the available currents should be well matched. Meanwhile the absorber thickness in individual subcell is reduced that results in improved carrier collection efficiency. Figure 2.1 shows the structure of the studied 4J cells in a simplified sketch and a cross-sectional SEM image of a fabricated device.

The fabricated cells were characterized by illuminated current-voltage (*I-V*) measurements with an AM1.5G solar simulator to determine the V_{OC} and fill factor (*FF*). The measured data in terms of voltage is presented in Table 2.1. One can notice that the increase of V_{OC} of a cell with increasing number of junctions is consistent with the V_{OC} of corresponding single-junction cells. From 1.03 V for a-SiO_x:H single-junction cell, the V_{OC} was sequentially increased to 1.91 V, 2.41 V, and finally 2.91 V for our 4J TFSSC. Therefore, the 4J cell functioned as expected from voltage point of view, showing that the absorber materials were of high quality in spite of the large thickness in the bottom subcell [29], and the tunnel recombination junctions between the subcells are performing well. A fill factor up to 78% was obtained, but it should be noted that the value of *FF* can be affected by the level of current mismatch [105].

External quantum efficiency (EQE) measurements with proper bias illumination were performed to investigate the spectral response of each subcell as well as to estimate

	V_{OC} (V)	Component V_{OC} (V)
a-SiO _x :H	1.03	1.03 (a-SiO _x :H)
a-SiO _x :H/a-Si:H	1.91 (+0.88)	0.89 (a-Si:H)
a-SiO _x :H/a-Si:H/nc-Si:H	2.41 (+0.50)	0.53 (nc-Si:H)
a-SiO _x :H/a-Si:H/nc-Si:H/nc-Si:H	2.91 (+0.50)	0.53 (nc-Si:H)

Table 2.1: Measured V_{OC} of relevant TFSSCs. Column on the left shows the V_{OC} of corresponding multi-junction cells starting with a-SiO_x:H subcell. Values in parentheses indicate the increase in V_{OC} . Column on the right shows typical V_{OC} of respective single-junction cells under AM1.5G illumination.

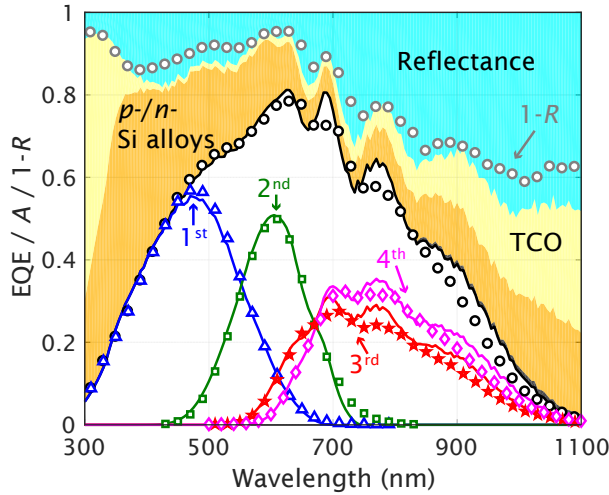


Figure 2.2: Spectral response of a 4J TFSSC. Colored symbols are experimental EQE and reflectance, while solid lines show simulated absorption spectra of the four subcells in a same solar cell structure. Simulated reflectance and parasitic absorption are indicated by the area plot.

the J_{SC} of the whole 4J device. For measuring the individual subcells, different combinations of light-emitting diodes (LEDs) were used to generate sufficient photocarriers in the remaining three subcells. The reflectance (R) of the solar cell was also measured to determine the total absorption ($A = 1 - R$) in the entire structure including parasitic optical losses in the supporting layers. In Figure 2.2, the colored symbols show the measured EQE of the four subcells of our first fabricated 4J device. The photocurrent density which a subcell can potentially generate was calculated by integrating the respective EQE with the AM1.5G spectrum, and the values are given in Table 2.2. It can be seen that the light absorption and thus the potential photocurrent density is not evenly distributed over the component subcells. The net current density of multi-junction solar cells is limited by the subcell delivering the smallest potential current density. The excess light absorption in other subcells cannot contribute to power generation.

	1st	2nd	3rd	4th	Total
Simulated initial	5.65	4.96	5.43	5.98	22.02
Measured initial	5.79	5.00	4.91	5.61	21.31
Measured optimized	5.49	5.99	6.16	6.09	23.73

Table 2.2: Implied/Measured photocurrent density of 4J cells in mA/cm². Current densities in individual subcells and their sum as the total response in the absorbers are shown.

2.4 Simulation-assisted current matching

Current mismatch is an essential problem in making highly efficient multi-junction TFSSC, and has a higher impact on the efficiency of solar cells consisting of more junctions because of their high voltage and low current density. Furthermore, current matching becomes more challenging for 4J cells since the structure contains a large number of layers as well as textured interfaces and each of them can affect the optical environment of the others. It is impractical to experimentally optimize current matching from scratch because there are too many variables for optimization and the fabrication of 4J TFSSCs at lab-scale is relatively time-consuming.

In order to facilitate the burdensome task of current matching, optical simulations have been used to estimate the absorption distribution in a solar cell. In the in-house optical model GenPro4 [106], [107], simulation of scattering properties at a textured interface is treated either by ray tracing or by scalar scattering theory depending on feature size of the concerned morphology. The feature size of the textured glass is much larger than the wavelengths of interest therefore ray tracing approach was selected in our simulations. The light is regarded as coherent in most of the layers in the structure, except the glass substrate and the intrinsic nc-Si:H layers in the third and fourth subcells, which are rather thick that the light does not exhibit interference effect. For the input parameters of simulation, atomic force microscopy was used to obtain morphological information of the textured substrate. The 3-dimensional topography was used to simulate the scattering properties of the interfaces by ray-tracing. Complex refractive indices of all involved materials were acquired with spectroscopic ellipsometry by analyzing respective layers deposited on flat glass. By assigning the materials, thicknesses and interfaces to the simulated structure in the model, the absorption spectrum for every layer as well as the total reflectance of the device can be calculated.

A simulation was carried out on a structure identical to the presented 4J device, so that the effectiveness of the optical model can be evaluated by experimental results. The simulated spectral response of the four subcells shown in Figure 2.2 (solid lines) agrees reasonably well with the experimental results except for the discrepancy at long wavelengths. Interestingly, the clearly visible fluctuation of EQE between 600 – 900 nm, the wavelength range within which the light is mainly absorbed in the third and fourth subcells, actually originates from the effect of coherent propagation of light in the intrinsic a-Si:H layer in the second subcell. The discrepancy at long wavelengths may be ascribed to the less accurate characterization of materials' optical constants, considering that determining absorption coefficients by spectroscopic ellipsometry is

very challenging for thin layers with low absorption. On the other hand, since the evolution of interface morphology depends on the deposition dynamics and is not perfectly conformal [64], [108], the scattering properties will change with the morphology of the interface. Overall the good agreement within a major part of the spectrum of interest confirms that this simulation approach is valid for our application, so it can be used for optimizing the design of 4J solar cells, in particular determining the thicknesses of absorber layers. Indeed, the simulated spectra also acted as a useful hint for choosing appropriate LEDs in the EQE measurements. According to the expected spectral response, the LEDs were selected to have low response in the measured subcell but can generate sufficient photo-carriers in other subcells.

2.5 Device optimization

Optimization of 4J TFSSCs was then carried out, based on the materials available at our lab. The influence of intermediate reflector, p-layer of the top subcell, anti-reflective coating and current matching has been taken into account. At first, n-type $\text{SiO}_x\text{:H}$ was used in the third and fourth subcells. It is a commonly used intermediate reflector for boosting the light absorption of upper subcells in multi-junction TFSSCs [80], [84], [86], [109]. However, it exhibits a broadband reflection which is not ideal for multi-junction cells. In this work, intermediate reflector was only used between the bottom subcells to avoid undesirable reflection losses of long-wavelength light. Secondly, it can be seen in Figure 2.2 that the EQE of the first subcell does not exhibit a sharp onset due to significant parasitic absorption. Concerning parasitic optical losses, in addition to the front TCO, the p-layer in the first subcell is of major importance, because high-energy photons can be easily absorbed in these layers before reaching the first absorber layer. Tackling this problem, the deposition parameters of the p-layer were adjusted to make the material more transparent. As a result, the improved response at the short wavelengths led to a gain in photocurrent density of 1 mA/cm^2 , while the thickness of a- $\text{SiO}_x\text{:H}$ absorber could be reduced. Finally, a plastic foil functioning as a broadband anti-reflective layer was applied onto the front side of solar cells to enhance the in-coupling of incident photons into the device.

Once the configuration of 4J TFSSCs with respect to the sequence of materials was decided, thickness determination of absorber layers was assisted by aforementioned optical simulations and fine-tuned by experimental examinations. The thicknesses of absorber layers from top to bottom were 70 nm, 380 nm, $1.9 \mu\text{m}$ and $3.2 \mu\text{m}$. Figure 2.3 shows the spectral response and illuminated J - V curve of the optimized 4J cell with better matched photocurrent densities and an improved optical design. From the EQE measurement, the J_{SC} of the optimized cell was estimated to be 5.49 mA/cm^2 . With V_{OC} and FF of 2.82 V and 73.9% respectively determined from illuminated I - V measurements, an initial efficiency of 11.4% has been achieved. The reduced V_{OC} is due to the adaption of the p-layer.

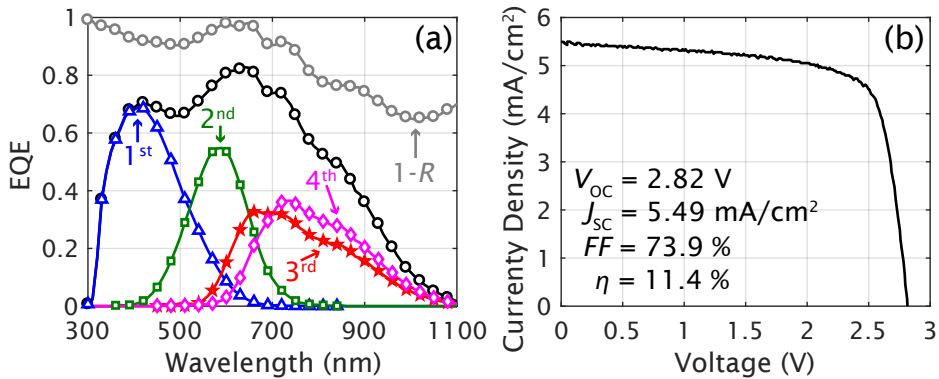


Figure 2.3: (a) Measured spectral response and (b) measured J - V curve of an optimized 4J TFSSC.

2.6 Discussion

Although the best initial efficiency of 11.4% achieved by the 4J TFSSCs is less than the state-of-the-art tandem and triple-junction cells, it demonstrated high V_{OC} and FF . The efficiency can be significantly improved by employing advanced materials in the cell. For instance, by replacing the front ITO with a high-mobility TCO material characterizing low free-carrier absorption such as hydrogen-doped indium oxide (IOH) [110], the absorption loss in the front TCO as well as the primary reflectance at long wavelengths can be reduced without compromising the electrical performance. Specifically, according to the simulations, the infrared absorption in front TCO can be decreased by an amount corresponding to a photocurrent density of 3 mA/cm². Similar adaption should also apply to supporting p- and n-layers. It can be seen in Figure 2.2 and Figure 2.3(a) that these supporting layers consume about 20% of the incident light in the range of 400 – 600 nm and a considerable amount in the infrared. On the other hand, the substrate morphology should be optimized to enhance the light scattering effect without scarfying the quality of materials deposited subsequently. Deploying effectively-scattering substrate can raise the EQE in the long-wavelength while reducing the parasitic losses in the short-wavelength by efficiently absorbing the blue light in the top cell. Moreover, beyond the existing technology, one of the most important tasks is to develop high-performance narrow-band intermediate reflectors, by which the blue light is reflected back to the upper subcells while the red light can be utilized in the bottom subcells. In this way the thicknesses of amorphous absorbers in the upper subcells can be reduced and a higher stabilized efficiency can be achieved in 4J TFSSCs. Last but not least, a low bandgap absorber such as nc-SiGe_x:H [83] should be introduced in the bottommost subcell to absorb the low-energy photons, so that it can extend the spectral utilization of TFSSCs to a broader part of the solar spectrum. This absorber is expected to have high absorption coefficient at long wavelengths as well as high material quality to reduce the material consumption and guarantee satisfactory electrical performance.

2.7 Conclusions

To conclude, a-SiO_x:H/a-Si:H/nc-Si:H/nc-Si:H *p-i-n* quadruple-junction TFSSCs have been experimentally demonstrated with V_{OC} higher than 2.82 V. Current matching in the 4J solar cells was facilitated by optical simulations to determine the optimal absorber thicknesses with minimum efforts at fabrication. Based on the available materials and light trapping scheme, the optical design of the solar-cell structure has been optimized. It resulted in a J_{SC} of 5.49 mA/cm² and ultimately an efficiency of 11.4%. Strategies were pointed out for further improvement in the performance of 4J TFSSCs.

3

Artifact interpretation of spectral response measurements on two-terminal multi-junction solar cells

This chapter was published in *Advanced Energy Materials* [111].

Abstract

Multi-junction solar cells promise higher power-conversion efficiency than the single-junction. With respect to two-terminal devices, an accurate measurement of the spectral response requires a delicate adjustment of the light- and voltage-biasing; otherwise it can result in artifacts in the data and thus misinterpretation of the cell properties. In this chapter, the formation of measurement artifacts is analyzed by modeling the measurement process, that is, how the current-voltage characteristics of the component subcells evolve with the photoresponse to the incident spectrum. This enables the examination on the operation conditions of the subcells, offering additional information for the study of artifacts. In particular, the influence of shunt resistance, bias-light intensity and bias voltage on the measurement is examined. Having observed the dynamics and vulnerability of the measurement, the proper ways to configure and interpret a measurement are discussed in depth. As a practical example, simulations of the measurements on a quadruple-junction thin-film silicon-based solar cell demonstrate that the modeling can be used to interpret eventual irregularities in the measured spectral response. The application of such tool is especially meaningful taking account of the diverse and rapid development of novel hybrid multi-junction solar cells, in which the role of reliable characterizations is essential.

3.1 Introduction

Multi-junction solar cells can reach higher power conversion efficiency than their single-junction counterparts by means of the better utilization of the photon energy in the solar spectrum [99]. They hold the highest record efficiencies across different branches of solar-cell technologies [112]–[114]. Typically, multi-junction solar cells are made in a two-terminal structure because of the simple workflow of device fabrication as well as the straightforward design of electrical terminals. The component subcells are electrically connected in series such that the device has only two terminals to interact with the external circuit. As a consequence, the individual response of the subcells is not directly accessible, leading to restrictions on the device characterization.

The measurement of the spectral response or external quantum efficiency (EQE) requires specialized strategies when applied to two-terminal multi-junction solar cells. Back in 1980s, certain procedures were proposed to measure the EQE of multi-junction cells [115]. The basic idea is to measure the EQE of each subcell separately, i.e., only one subcell is examined at a time. Continuous light sources, which are referred to as the bias light, are used to generate photocarriers in the subcells. Having manipulated the bias spectrum, the targeted subcell provides the least potential photocurrent. Owing to the nature of series connection, this subcell limits the current of the multi-junction cell. On top of the bias light, a periodically-chopped monochromatic light source is used to excite additional photocarriers in the subcells. The resulting periodic perturbation in the external circuit, detected by a lock-in amplifier, represents the response of the current-limiting subcell to the incident monochromatic light. As a result, the EQEs of different subcells can be examined individually by adjusting the bias illumination. To improve the measurement, voltage biasing may be used in addition to light biasing. Conventionally, a bias voltage is applied such that the targeted subcell can operate like it is in its short-circuit condition.

Such measurement is susceptible to artifacts because of its indirect and dynamic essence of signal generation as well as the strong correlation between the subcells. Several possible measurement artifacts have been observed and discussed in literature. Based on the observations on GaInP/Ga(In)As/Ge triple-junction cells, Meusel et al. systematically studied the artifacts and associated them with the low shunt resistance or low reverse breakdown voltage of the subcell to be measured [116]. They also ascribed the artifact formation to the correlation between the operation points of the subcells. The measured signal including the artifacts can be affected by the bias condition. These effects have been discussed with the emphasis on either bias light [117]–[120] or bias voltage [116], [119], [121]–[123], resulting in suggestions for mitigating certain measurement artifacts. Accordingly, to promote reliable measurements, comprehensive measurement procedures have been proposed in literature [116], [124] and in a standard published by ASTM International [125].

Although the mentioned literature can serve as useful guidelines for adjusting the measurement configuration, it does not provide an unambiguous indication to distinguish between the genuine response and the artifacts. Furthermore, refining the measurement configuration is typically a cumbersome and time-consuming process which requires iterative changes on both bias light and bias voltage. In practice, it becomes especially difficult when more than two subcells are involved and/or when

the EQE spectra of the subcells spectrally overlap to a great extent, that is usually the case in thin-film silicon-based solar cells [80], [98], [113], [126]–[128]. Similar challenges can also be expected when studying two-terminal multi-junction solar cells with novel materials and/or structures, for which the EQEs of the component subcells may not be well-known. In these cases, it can be tricky to determine a proper bias configuration and to interpret the result. This issue is worth extra attention considering that many novel hybrid structures have emerged in the last few years, such as perovskite/crystalline silicon tandem cells [129]–[131], perovskite/CIGS tandem cells [132], [133] and a-Si:H/organic double- and triple-junction cells [134]. While the researches demonstrated promising routes to surpass the high efficiencies given by optimized single-junction cells, little concern was shown for the credibility of the EQEs being reported.

In experiments, measurement artifacts can be studied by varying the measurement conditions and with different solar cells. The information is quite limited since the current in external circuit is the only output signal. In consequence, understanding the mechanism of artifact formation is not a straightforward task. In this work, we studied the formation of various types of artifact in the EQE measurement of two-terminal multi-junction cells by means of modeling. The signal obtained in an EQE measurement of a multi-junction cell under defined bias light and bias voltage condition can be simulated. Through the simulations, it was clearly shown how the cell properties or the bias conditions can affect the EQE spectra acquired in measurements. Modeling the entire measurement process gives extra internal information about the operation conditions of the subcells, which leads to better understanding of the mechanisms of artifact formation. The model was also applied to interpret the irregular EQE spectra obtained in actual measurements. The insights gained from the in-depth analyses on artifact formations, together with the application of auxiliary modeling in the measurement and interpretation process, enable more reliable determination of the studied spectral response of multi-junction solar cells.

3.2 Terminology and scope

In this chapter, a measurement artifact means a deviation of the probed EQE from the genuine EQE. The **genuine EQE** is regarded as an inherent property of the solar cell (and its subcells). We define the genuine EQE as the EQE of a subcell when it operates in its own short-circuit condition and when its parent multi-junction cell is under an incident spectrum comparable to the AM1.5G. In contrast, the **probed EQE** is regarded as a quantity obtained in a measurement. The probed EQE is derived from the detected signal so it is dependent on the measurement condition. It does not necessarily reproduce the genuine EQE, which one intends to measure. The discrepancy between the genuine and probed EQE, i.e. the artifact, is the main object of this study.

Besides, a few terms used in this chapter might not be common in literature so they require clear definitions. In principle, the EQEs of different subcells in a multi-junction cell are measured separately. In a certain measurement, one sets up a bias condition, which is a combination of bias light and bias voltage, with the *intention* to measure

a certain subcell. To clarify, we refer this subcell being intentionally investigated to as the **targeted subcell**; the rest of the subcell(s) is referred to as the **non-targeted subcell(s)**. While the incident continuous light is referred to as the **bias light**, the chopped monochromatic light being used to excite a periodic signal is referred to as the **probe light**. When the J - V characteristic of a subcell is examined as it is a separate solar cell with its own electrical terminals, such J - V characteristic is referred to as the **implied J - V** characteristic because it is not accessible in experiments but only in simulations. Similarly, the incident light generates excess carriers in a subcell, which would result in a certain photocurrent if it was an independent solar cell. Because the actual current in a subcell also relies on the other subcells in the series, such hypothetical photocurrent is referred to as the **potential photocurrent** of the subcell. For simplicity, the potential photocurrent density is indicated as J_{ph} . J_{ph} is also used to quantitatively represent the illumination level of a subcell. Lastly, in many cases, a multi-junction cell and its subcells are examined at their operation points. The **operation point** of a (sub)cell is represented by its operation voltage and operation current density (V, J), under a given external condition. An operation point can typically be indicated as a point on the (implied) J - V curve. At such point on the curve, the derivative of current density (J) with respect to voltage (V), dJ/dV , can be examined for further analyses. The derivative is the differential conductance per unit area of the subcell, and is referred to as **differential conductance** in this paper for simplicity.

This chapter is structured as the following. The modeling method used in this work is described in Section 3.4. With the help of modeling, the mechanisms of artifact formation are analyzed in Section 3.5. Measurements on tandem solar cells, which are the simplest multi-junction cells, have been simulated. The shunt resistance of the targeted subcell, the bias light intensity and the bias voltage were altered to examine how they affect the probed EQE. In Section 3.5.5, a set of experimentally measured EQE spectra for a quadruple-junction solar cell is shown to demonstrate how modeling can help to interpret the results from actual measurements. Having gained a better understanding of the principle and mechanism behind the EQE measurement and its artifact formation, in Section 3.6 we gave an in-depth discussion on how to properly conduct the measurement and interpret the outcome. Finally, perspectives are presented in Section 3.7 on the potential applications of the model. All experimental details regarding the acquisition of simulation input and the demonstrated measurements are reported in Section 3.3.

3.3 Experimental section

In this work, the origin of artifacts is studied by modeling the EQE measurements of tandem (double-junction) solar cells. The simulations are based on a thin-film p - i - n a-Si:H / nc-Si:H tandem cell. The thickness of the absorber layers is 350 nm and 3000 nm, and the J_{ph} is 14.0 mA/cm² and 14.4 mA/cm² for the top and bottom subcells, respectively. The genuine EQE spectra used for the simulations were adopted from the work by Tan et al. [90], and are shown in Figure 3.4(a) (gray dashed lines). The quadruple-junction cell discussed in Section 3.5.5 is a thin-film p - i - n a-SiO_x:H /

a-Si:H / nc-Si:H / nc-Si:H quadruple-junction solar cell. The thickness of the absorber layers is 67/380/1900/3200 nm and the device structure is the same as the one reported in Chapter 2. The genuine EQE spectra required in the simulations were obtained by deliberate measurements on the studied cell and further confirmed with the result of optical simulations [98], although it should be pointed out that the purpose of the simulations is to find out how the probed EQE may deviate from the genuine EQE. In this scenario, it is irrelevant whether or not the used EQE spectra accurately represent the original device.

The EQE measurements of the quadruple-junction cell were performed using an in-house system. The system uses a xenon light source and a 3-grating monochromator to provide a monochromatic light source, which was then chopped at a frequency of 123 Hz before reaching the devices. The current induced by this light was measured through a resistor with a lock-in amplifier. The measured value was compared with the one from a calibrated reference diode to calculate the EQE. The bias light was provided by a selection from 8 different LEDs with adjustable intensity and with wavelengths of emission peak ranging from 350 nm to 940 nm. The voltage of the measured cell was biased via the control circuit. In addition, the temperature of the solar cell was controlled at 25 °C through the mounting stage. As for another input of the simulations, the spectral irradiance of every light source was measured using a spectrometer (Avantes AvaSpec-2048 UA/IB) at the spot where the solar cell was mounted.

For every component subcell in the studied tandem and quadruple-junction solar cells, a single-junction cell was fabricated in order to acquire the parameters in the one-diode equation for the simulations. The single-junction cells have similar *p-i-n* structures to their counterparts in the multi-junction cells, while their front and rear sides are covered by glass/TCO and Ag, respectively. The fabrication procedure and further details about the cell structures are reported elsewhere [90], [98]. Illuminated *J-V* measurements were performed on the single-junction cells using a dual-lamp continuous solar simulator (WACOM WXS-90S-L2, class AAA) with an incident irradiance of 1000 W/m². Dark *J-V* measurements were performed using the same setup but shielding the cells from the light. During all measurements, the temperature of the cells was controlled at 25 °C. The one-diode equation was fitted with the measured *J-V* data to extract a set of diode parameters for every single-junction cell. The parameter sets were then used to simulate the *J-V* characteristics of the corresponding subcells.

3.4 The model

In this work, a model was developed to simulate the probed EQE of a two-terminal multi-junction cell in a differential spectral response measurement, in response to a defined measurement condition. In measurements, a certain experimental configuration results in a certain electrical signal in the studied solar cell, which is then interpreted as the EQE of the targeted subcell. The model includes the influence of the probe light, bias light and bias voltage, together with the optoelectronic response of the solar cell, so that it reflects the realistic response of the device. By simulating step-by-step how

a specific solar cell and a measurement condition result in the current signal which can be detected in the external circuit, the model enables investigations on the internal changes of the multi-junction cell and its component subcells during the process of measurement. It provides extra information about the cell operation, which is typically inaccessible in measurements.

The procedure of a simulation with our model is illustrated in Figure 3.1, and is further explained below:

1. The incident spectrum, the spectral photon flux density in specific, is a major input for the simulations. It comprises a static component from the continuous bias light and a periodic component from the chopped probe light. With the bias light as a background illumination, the response of the solar cell is simulated with and without the probe light, respectively.
2. The potential photocurrent density (J_{ph}) in each subcell is calculated by integrating the spectrum of incident photons with the genuine EQE spectrum of the corresponding subcell.
3. The implied current density-voltage (J - V) characteristic of each subcell is determined by its illumination level, which is represented by its J_{ph} . To do so, each subcell is treated as an individual single-junction cell. The derivation of the J - V curves in respect of certain J_{ph} makes use of physical models describing the device behavior, which can vary between different photovoltaic technologies. For the sake of genericity, such derivation in this article is based on the commonly used one-diode equivalent circuit:

$$J_i = J_{0i} \left(e^{\frac{q(V_i - J_i R_{s_i})}{nkT}} - 1 \right) - J_{ph_i} + \frac{V_i - J_i R_{s_i}}{R_{sh_i}} \quad (3.1)$$

where q , k and T are elementary charge, Boltzmann constant and absolute temperature, respectively. The adjustable parameters in the equation J_0 , n , R_s , R_{sh} and J_{ph} are the saturation current density, diode ideality factor, series resistance, shunt resistance, and (potential) photocurrent density, respectively. The subscript (i) indicates a certain subcell.

4. The J - V characteristic of the multi-junction cell is synthesized using the implied J - V curves of its component subcells, as it is demonstrated with an example in Fig. 3.2. In particular, the subcells are treated as the components in an ideal series connection. At every examined current (J_{mj}), the voltage of the multi-junction cell (V_{mj}) is the sum of the voltages of all subcells (V_i) at such current density level according to their implied J - V characteristics.

$$V_{mj} = \sum_i V_i (J_i = J_{mj}) \quad i = 1, 2, \dots \quad (3.2)$$

5. The operation points of the multi-junction cell and its component subcells are controlled by the applied bias voltage (V_{bias}). In a measurement, there is:

$$V_{mj} = V_{bias} \quad (3.3)$$

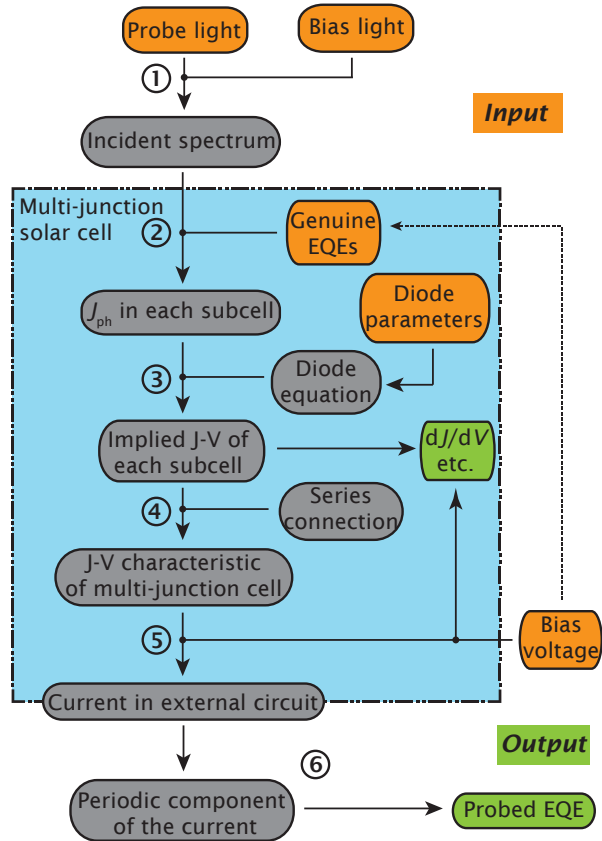


Figure 3.1: Flowchart of the model simulating the probed EQE of a two-terminal multi-junction solar cell under certain measurement configurations. The blue outlined region distinguishes the internal properties of the cell from the external excitation and outcome. The input and output of the model are labeled in orange and green, respectively. The dashed line indicates the extensibility of the model by incorporating additional physical models.

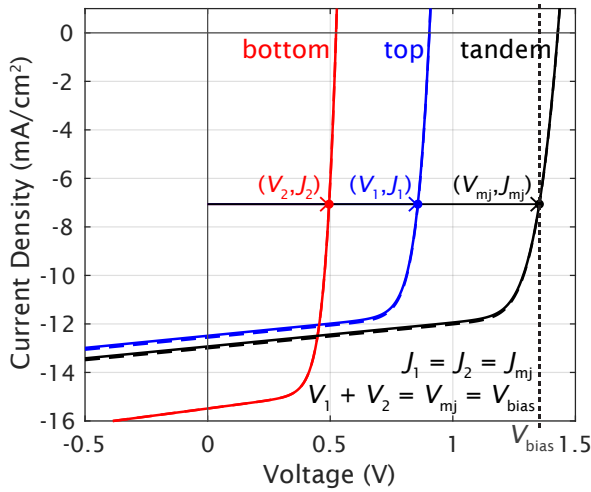


Figure 3.2: Composing the J - V characteristic of a multi-junction cell by the implied J - V characteristics of its component subcells. In this example, the tandem cell is current-limited by the top subcell.

so the current $J_i = J_{mj}$ and also the voltage V_i can be determined correspondingly, as shown in Fig. 3.2.

6. In practice, a lock-in amplifier is used to detect the periodic component of the current excited by the chopped probe light [135], [136]. Based on this principle, in the model the periodic component of the electrical signal is calculated by the subtraction between the currents responding to the illumination with and without the probe light. This arithmetic difference is then converted into the probed EQE using the known spectral photon flux density of the probe light.

A complete set of input includes the incident spectra of the bias light and probe light, as well as the genuine EQE and the diode parameters of each subcell. Depending on the purpose of the simulations, the input parameters can be either measured experimentally, synthesized by other simulations, or generated artificially. The ultimate output of the model is the probed EQE with respect to the cell properties and measurement conditions given in the input. In addition to this, the operation points of the subcells and the related information, which cannot be obtained in a measurement, are also valuable output.

3.5 Artifact analysis

In this section, modeling of EQE measurements on multi-junction cells is used to study the formation of artifacts. Taking into account the device characteristics and measurement condition, the model reflects the realistic response of the device. In the following subsections, several sources of measurement artifacts have been studied by

changing the input of the model. Because of the way how the model is constructed, the revealed artifacts are the consequence of the characteristics of illuminated semiconductor diodes (i.e. the subcells) and the correlation between them. The discussions are generically applicable to different types of two-terminal multi-junction cells, even though thin-film silicon-based solar cells were used in the demonstration.

3.5.1 Artifact formation by the drift of operation points

The mechanism of how the voltage drift in subcells results in measurement artifacts has been explained by Meusel et al. [116], and is also demonstrated here with two distinctive cases for the sake of clarity and completeness of our paper.

The basic mechanism can be understood by looking into the J - V characteristics of the subcells with and without probe light, in the case of a tandem solar cell. The described changes are illustrated in Figure 3.3. At the wavelength of 460 nm, the genuine EQE of the bottom subcell is almost zero. The probe light generates additional potential photocurrent in the top subcell, lifting its implied J - V curve. The grown J - V curve of the top subcell gives a higher voltage at the same current level. Consequently, it shifts the operation point of the bottom subcell to a more negative voltage, thus a higher current and a higher probed EQE. In the case of 820 nm, only the bottom subcell has response to the probe light. The additional potential photocurrent in the bottom subcell shifts the operation voltage of the top subcell to a lower value. Accordingly, the operation point of the bottom subcell is shifted to a less negative voltage and a lower current, counteracting the initial increase in photocurrent thus a declined probed EQE. In both cases, the deviation in current thus the EQE is directly related to the shift of operation voltage in the target (bottom) subcell.

3.5.2 Effect of shunt resistance

EQE measurements of thin-film a-Si:H / nc-Si:H tandem solar cells were simulated to show the influence of shunt resistance of the targeted subcell on measurement artifacts. Without losing genericity, the bottom subcell is chosen as the targeted subcell in the following investigation. In the simulations, R_{sh} of the bottom subcell was adjusted between $200 \Omega \text{ cm}^2$ and $5000 \Omega \text{ cm}^2$. The J_{ph} in the bottom subcell generated by the bias light was set at 14 mA/cm^2 , near its value under AM1.5G illumination. For the top subcell it was set at 20 mA/cm^2 to guarantee the device current-limited by the bottom subcell. The J_{ph} generated by the probe light was in the order of 10^{-1} mA/cm^2 . In all cases the bias voltage was 0 V.

Except the R_{sh} of the bottom subcell, the diode parameters of the simulated subcells were kept unchanged at their default values, which are listed in Table 3.1. At the regime where the illumination level is comparable to that under AM1.5G, all diode parameters except J_{ph} can be treated as constants, which were obtained by fitting the one-diode equation with the AM1.5G-illuminated J - V data.

Figure 3.4(a) shows the simulated EQE spectra in which artifacts can be observed. In the wavelength range where the bottom subcell has a higher response than the top subcell, the simulated probed EQE is lower than its genuine value; the opposite is true at the wavelengths where the bottom subcell has a lower response. The lower the

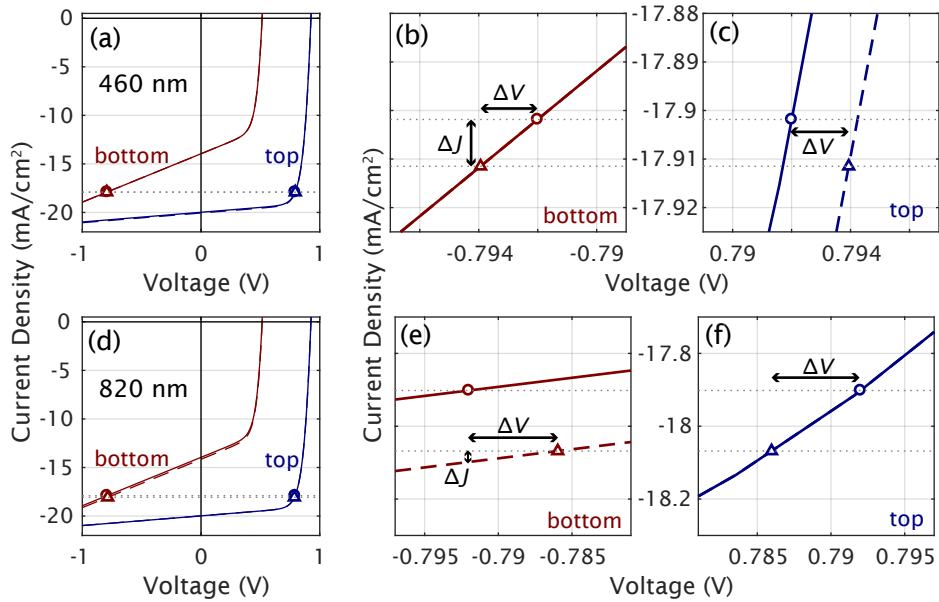


Figure 3.3: The mechanism of artifact formation owing to the drift of operation points, shown by the implied J - V curves of the subcells when the probe light is at 460 nm (a–c) and 820 nm (d–f), respectively. The operation current densities in the two conditions (under bias light with/without probe light) are indicated by the dotted lines beside the markers, which show the operation points.

	$J_0(\text{mA}/\text{cm}^2)$	n	$R_s(\Omega \text{ cm}^2)$	$R_{sh}(\Omega \text{ cm}^2)$
Top subcell	1.05×10^{-8}	1.69	0.94	1000
Bottom subcell	1.05×10^{-5}	1.44	0.65	750

Table 3.1: Default parameters used in the one-diode equation for the demonstrated a-Si:H / nc-Si:H tandem solar cell.

shunt resistance, the more the probed EQE deviates from the genuine value. Meusel et al. ascribed this kind of artifact to the drift of operation voltage occurring in the subcells stimulated by the probe light [116], and it was also explained and further investigated in Section 3.5.1 with two distinctive examples. In our case, the deviation in current thus the EQE is directly related to the shift of operation voltage in the bottom subcell. The drift is more severe with lower R_{sh} , as it is shown in Figure 3.4(b).

The differential conductance of the subcell at its operation point, which is the slope (dJ/dV) of its implied J - V curve, was investigated as it represents how sensitive the current is to a change in voltage. Figure 3.4(c) shows that for the bottom subcell, dJ/dV clearly increased when R_{sh} was reduced. As a result, a subcell with lower R_{sh} suffers from more current drift (ΔJ) in case of a certain voltage drift (ΔV), hence greater extent of artifact. Looking into the operation point of the top subcell, it affects the artifact through different ways at the two wavelengths discussed in the following. At 820 nm, the effect is determined by ΔV in the top subcell induced by the increase in photocurrent, so the artifact is directly affected by dJ/dV at the operation point. It can be seen in Figure 3.4(b) and (c) that ΔV is in line with the variation of dJ/dV in the top subcell. A very steep slope helps to suppress artifacts suggesting that the non-targeted subcell(s) should operate as near its open-circuit point as possible. On the other side, at 460 nm, the mechanism is less straightforward. The ΔV in the top subcell depends on how much its implied J - V curve expands in response to the photocurrent generated by the probe light. Qualitatively, such influence on operation voltage is more pronounced when dJ/dV at operation point is low. Therefore, the requirement at 460 nm conforms to that at 820 nm. In brief, a low dJ/dV for the targeted subcell and a high dJ/dV for the non-targeted subcell(s) are beneficial to the EQE measurement of multi-junction solar cells.

The shunt resistance of the targeted subcell affects the measurement artifacts not only through dJ/dV of the implied J - V curve in the reverse voltage regime, but also by locating the operation point of the non-targeted subcell along its implied J - V curve. Figure 3.4(d) shows the implied J - V curves of the subcells under only bias illumination. Without bias voltage, the non-targeted subcell typically operates at a positive voltage near its V_{OC} . The targeted subcell works at the corresponding negative voltage, and its operation current determines the current in the device. In the regime of the negative voltage, the operation current highly depends on R_{sh} , even though the potential photocurrents (at 0 V) are the same. As a result, given the same level of bias illumination, a lower R_{sh} in the targeted subcell moves the operation point of the non-targeted subcell towards lower voltage, at which the measurement is more susceptible to artifacts. In other words, an intense bias light for the non-targeted subcell is needed for an accurate measurement in case of a low R_{sh} in the targeted subcell. It can be seen in Figure 3.4(d) that, although the photocurrent provided by the probe light was only in the order of 10^{-1} mA/cm², a difference of 6 mA/cm² in J_{ph} generated by the bias light may not be enough to suppress the artifact when the shunt resistance is low. The configuration of the bias light is not as simple as fulfilling the basic current-limiting requirement (a difference in J_{ph}). Under reverse voltage, the operation current of the targeted subcell may approach or even surpass the J_{ph} in the non-targeted subcell in case of a low R_{sh} . A similar problem can occur when the

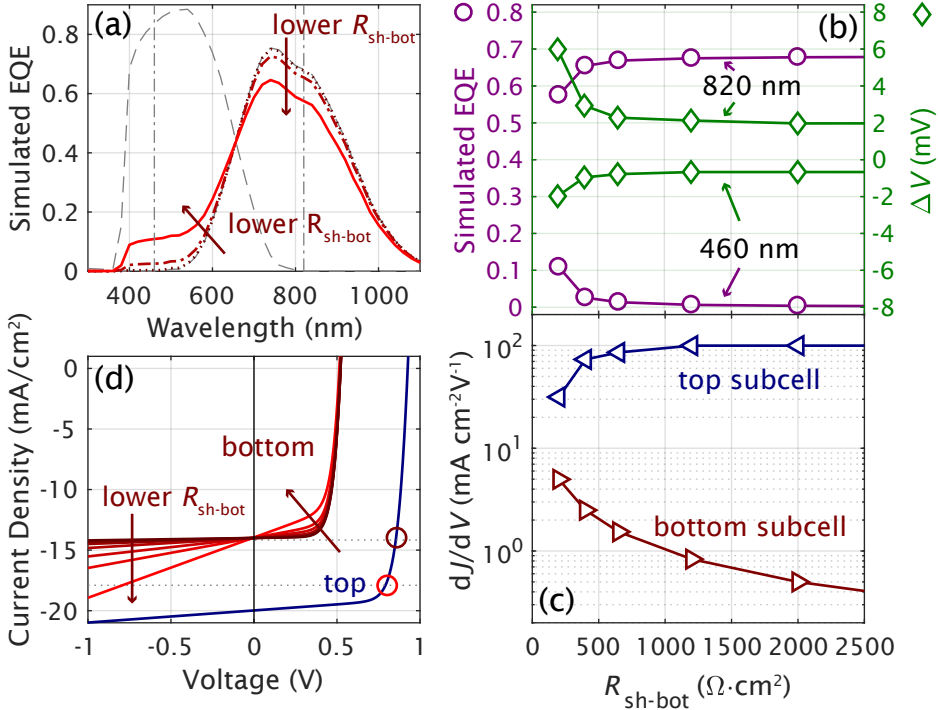


Figure 3.4: The effect of R_{sh} of the targeted subcell on the EQE measurements. (a) The measurement artifact becomes more obvious when R_{sh} is changed in the sequence of 2000, 400, and 200 Ωcm^2 . The gray dashed curves show the genuine EQE spectra of the top and bottom subcells [90], and the vertical dash-dotted lines indicate the two wavelengths at which the cell operation is further discussed. (b) Left axis, circle marker: the probed EQE at certain wavelengths. Right axis, diamond marker: the difference in operation voltage of the bottom subcell between the bias/bias+probe light conditions. (c) dJ/dV of implied J - V curves of the subcells at their operation points under only bias light. (d) Implied J - V curves of the component subcells under the same bias light condition, but with varied R_{sh} in the bottom subcell. The dotted lines indicate the operation currents of the cells with the highest and lowest R_{sh} . The circles emphasize the different dJ/dV in the top subcell at the corresponding operation points.

breakdown voltage of the targeted subcell is low.

3.5.3 Effect of bias conditions

This section reports the effect of the bias-light intensity and of the bias voltage on the measurement artifacts. First, the influence of bias-light intensity was examined. With the bottom subcell as the targeted subcell, its J_{ph} supplied by bias light was assigned at 14 mA/cm^2 , and the illumination level for the top subcell was changed between 15 mA/cm^2 and 40 mA/cm^2 . Similarly to that in Section 3.5.2, EQE measurements of the tandem cell were simulated using the diode parameters given in Table 3.1, except the R_{sh} of the bottom subcell was set at a relatively low value of $200 \Omega \text{ cm}^2$. The bias voltage is 0 V . Figure 3.5(a) shows that the probed EQE is substantially different at various illumination level for the top subcell, according to simulations. At the lowest illumination level, that $J_{ph-top}/J_{ph-bot} = 15/14 \text{ mA/cm}^2$, the probed EQE behaves like the EQE of the top subcell with some artifact, even though the J_{ph} in the top subcell is still higher and one may expect a probed EQE representing the response of the bottom subcell.

To understand this phenomenon, the operation points of the subcells are examined in Figure 3.5(b). When the top subcell is supplied a low J_{ph} of 15 mA/cm^2 , it operates at a low positive voltage near 0 V , instead of the desired high voltage which is near the V_{OC} . In such condition, the top subcell is the one actually throttling the current. The bottom subcell can support the increase in current when an additional potential photocurrent is generated in the top subcell by the probe light, while the opposite is not true. The external current, hence the probed EQE, is more related to the spectral response of the top subcell.

The different profiles of the probed EQE spectra can be explained by the differential conductance dJ/dV of the component subcells at their operation points, as shown in Figure 3.5(c). At the highest illumination level, dJ/dV of the top subcell is higher than that of the bottom subcell by more than one order of magnitude. The probed EQE aligns well with the genuine EQE of the bottom subcell. When the difference between the dJ/dV of the two subcells decreases, the probed EQE deviates more from the genuine EQE of the bottom subcell. The trend continues until a point where dJ/dV of the top subcell goes lower than that of the bottom subcell. In those illumination conditions, the probed EQE exhibits like the EQE of the top subcell. Therefore, Figure 3.5(a–c) explain how a high illumination level for the non-targeted subcell can mitigate the artifacts. By increasing the illumination level J_{ph} in the non-targeted subcell, its operation voltage is positioned towards its V_{OC} , around which the non-targeted subcell has the steepest J - V relation thus interferes the least with the external current and the probed EQE.

Figure 3.5(a) and (c) reveal that the lower the dJ/dV of a certain subcell at its operation point, the greater weight the genuine EQE of this subcell has on the probed EQE. This claim can be justified by the nature of dJ/dV , which can be interpreted as the differential conductance of the subcell at the operation point. At the operation point, when a subcell has a very high differential conductance, the subcell works like a conductor that it hardly affects the current running through the device. Consequently, a subcell with high dJ/dV contributes very little to the probed EQE. In contrast, a

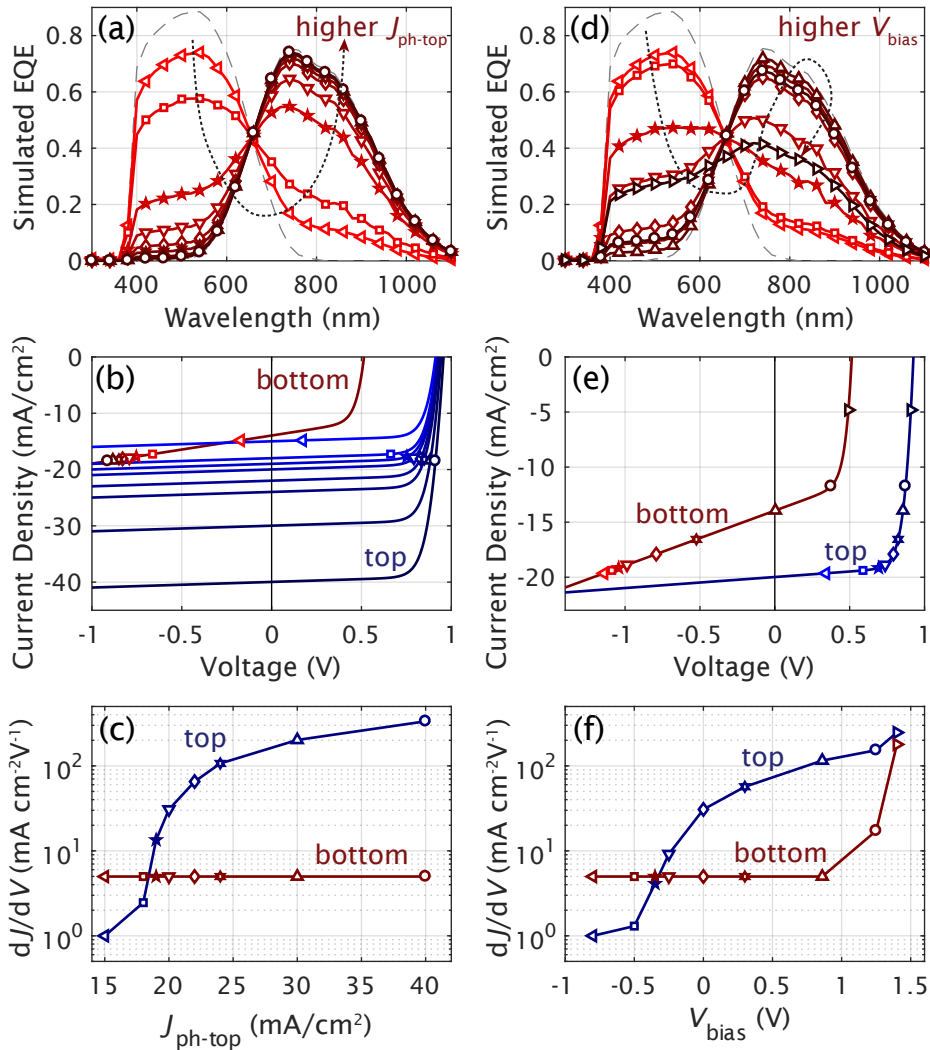


Figure 3.5: Illustration of how the bias light or bias voltage affects measurement artifacts. (a–c) Simulations of EQE measurements with different bias illumination levels in the non-targeted subcell. The probed EQE spectra in (a) show the evolution of artifacts with the intensity of the bias light. (b) Implied J - V curves of the subcells under certain bias light conditions, with the markers indicating the operation points. (c) dJ/dV at the operation points under different bias light levels J_{ph-top} . (d–f) Simulations of EQE measurements with different bias voltage applied. Note that in (d) the probed EQE changes with V_{bias} in different ways in two different voltage regimes.

subcell with a very low differential conductance is highly resistive such that it limits the current. As a result, the probed EQE is dominated by the subcell with the lowest dJ/dV at the operation point.

In terms of alleviating measurement artifacts, the configuration of bias voltage (V_{bias}) could also play a big role considering its relevance to the operation points. Looking into this issue, EQE measurements of a tandem solar cell were simulated with V_{bias} being tuned from -0.8 V to 1.4 V . Once again, R_{sh} of the bottom subcell was set at $200\ \Omega\text{ cm}^2$ to make the artifacts more noticeable, while the other diode parameters were kept the same. With the bottom subcell being the targeted one, the bias illumination level was fixed at $J_{\text{ph-top}}/J_{\text{ph-bot}} = 20/14\text{ mA/cm}^2$. Under the bias light, the V_{OC} of the top subcell is 0.93 V .

A trend similar to the effect of bias illumination can be seen in Figure 3.5(d-f) when V_{bias} ranging between -0.8 V to 0.86 V . In this range, the differential conductance dJ/dV of the bottom subcell at its operation point is constant while the one of the top subcell increases with V_{bias} , leading to a transition of the probed EQE from a top-subcell-like response to a bottom-subcell-like response. With V_{bias} surpassing 0.86 V , at which the operation voltage of the bottom subcell equals 0 V , dJ/dV of the bottom subcell rises abruptly with V_{bias} . It corresponds to the region in which the bottom subcell operates at positive voltage and its operation current becomes more sensitive to the change in operation voltage. As a consequence, the transition of probed EQE with increasing V_{bias} is reversed. The influence from the top subcell becomes significant at high voltage. This phenomenon can be expected from Figure 3.5(f) since the difference between the dJ/dV of the two subcells deminishes in the high-voltage regime.

Commonly, applying a positive bias voltage is taken as a measure to compensate the voltage offset from the non-targeted subcells with the aim that the targeted subcell can be examined near its short-circuit condition. Here we demonstrated that even without taking in account the possible voltage-dependent photoresponse of the targeted subcell, an appropriate bias voltage is still beneficial solely because of the illuminated J - V characteristics of the non-targeted subcells, that is, the diode-like J - V response exhibits a greater dJ/dV at a higher operation voltage. It is noteworthy that beyond a certain limit the positive bias voltage turns to be detrimental. In the shown example the optimal bias voltage was slightly lower than the V_{OC} of the non-targeted subcell. However, finding the optimum is not always as easy when the number of subcells increases and/or the bias illumination level is distinct from the standard testing condition.

3.5.4 Illumination-dependent response

Adapted model for low-light regime

The capability of our model to reproduce measurement artifacts is decided by the effectiveness of the assumptions and physical equations used in the model for describing the behavior of the studied multi-junction cells. One should always bear in mind the conditions in which a model is (relatively) valid. The results discussed in the previous sections are based on the one-diode equivalent circuit. Such model is very useful for identifying the artifacts raised by the diode-like J - V characteristics in general

photovoltaic cells at an illumination level comparable to AM1.5G, which is the case in Section 3.5.2 and 3.5.3. On the other hand, the diode parameters acquired at a certain illumination level do not guarantee a good match with the J - V data obtained in a different condition. An EQE measurement of a tandem cell in dark condition (no bias light) was simulated using the parameters obtained from illuminated diodes. The simulated probed EQE shown in Figure 3.6(a) (the curve labeled “w/o adaption”) gives a broad spread over the spectrum. On the contrary, it is commonly expected and often observed that the EQE measured in the dark mainly outlines the overlap between the EQE spectra of all component subcells. Although such expectation was not always met as shown in literature [117], [137], [138], the result in Figure 3.6(a) is worth extra attention. In this case, the discrepancy between this simulation and the aforementioned expectation originates from a shunt leakage overestimated by the parameters of illuminated diodes. It can be explained by the measured J - V curves of an a-Si:H single-junction cell under dark and AM1.5G conditions, respectively. This exact cell is the one used to acquire the diode parameters of the top subcell in the demonstrated tandem cell. For better comparison of their reverse characteristics, the illuminated J - V curve in Figure 3.6(b) is shifted so that it comes across the origin. Apparently, the short-circuit resistance ($(dJ/dV)^{-1}$ at $V = 0$ V) of the dark J - V curve is much higher than that of the illuminated one, meaning that the change in current caused by a voltage drift is smaller in the dark case. Therefore, the use of the diode parameters acquired from the J - V relation measured under AM1.5G spectrum overestimates the shunt leakage in the dark and low-light conditions. Generally speaking, such behavior can happen when the impedance of the solar cell is not a constant but can be affected by the carrier concentration or injection level in the cell. In case of solar cells constituted by P-I-N diodes, such change of impedance in the short-circuit region can be caused by the recombination losses in the intrinsic layer which are dependent on the carrier concentration thus also on the J_{ph} [139].

The model used in the previous sections was adapted to extend the applicable range over low-light conditions. The one-diode equivalent circuit was kept for synthesizing the J - V relation, but the diode parameters were interpolated between their dark and AM1.5G-illuminated values. When the one-diode equation was individually fitted with the two J - V curves in a pair, such as the two solid lines shown in Figure 3.6(b), it was found that the diode parameters mainly differed in R_{sh} besides J_{ph} . Therefore, a semi-empirical approach inspired by the work of Merten et al. [139] was used for the interpolation of R_{sh} . Assuming a linear relation between $\log R_{sh}$ and $\log J_{ph}$, the R_{sh} at a certain illumination level J_{ph} was interpolated between the two known data points from the dark and AM1.5G conditions.

For the sake of model validation, measurements of the same tandem cell in the dark condition were simulated with the adapted model. The parameters in Table 3.1 were used for both dark and AM1.5G-illuminated conditions, except the dark R_{sh} was both set at $6.7 \times 10^5 \Omega \text{ cm}^2$ based on the measured dark J - V data. The AM1.5G-illuminated J_{ph} was 14.0 mA/cm^2 and 28.0 mA/cm^2 for the top and bottom subcells, respectively, while the dark J_{ph} was 0.002 mA/cm^2 for both. This diode configuration is based on the measurements on the fabricated cells, and it serves as the reference cell in the following study.

The simulation output of the adapted model is shown in Figure 3.6(a). For the

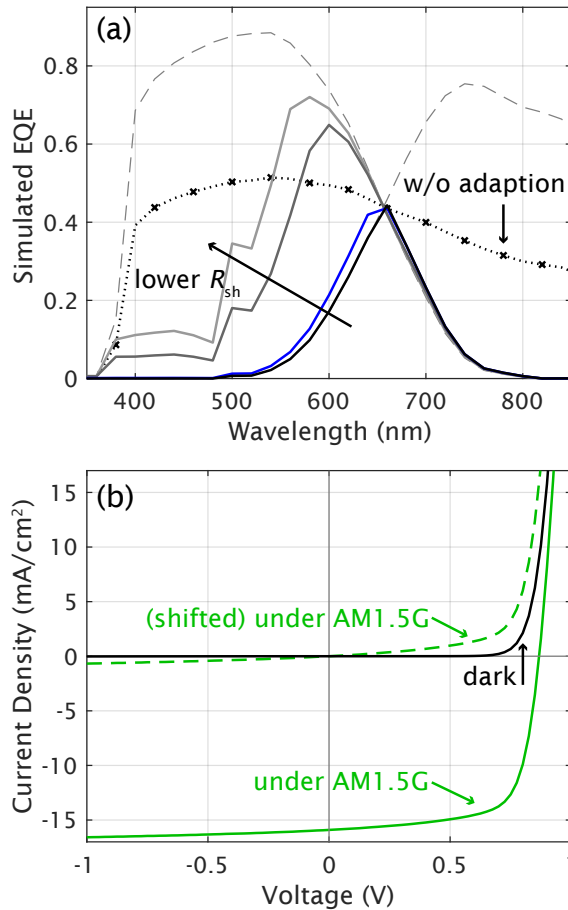


Figure 3.6: The response of solar cells in the dark and illuminated conditions cannot be described with the same set of one-diode parameters. (a) Simulations of EQE measurement on tandem cells in the dark condition. The dotted line with cross markers was simulated with the diode parameters acquired under AM1.5G spectrum. The solid lines were simulated using the adapted model with different R_{sh} in the bottom subcell. The blue line is from the reference cell. The dashed lines are the genuine EQE of the top and bottom subcells. (b) Experimentally measured J - V curves of a single-junction a-Si:H cell under dark and AM1.5G-illuminated conditions. The illuminated one is also shifted and aligned to the origin, plotted as a dashed line, for more straightforward comparison.

reference cell, the EQE probed in the dark basically follows the overlap of two genuine EQE spectra with a slight increase. The slight deviation is not a fault of the simulation but a realistic indication of the shunt leakage at such illumination level. To demonstrate this, the influence of shunt leakage was further examined by simulating tandem cells with different R_{sh} in the bottom subcell. In this series of simulations, the reference $R_{sh-dark}$ and $R_{sh-AM1.5G}$ of the bottom subcell were multiplied by factors of $\frac{1}{50} / \frac{1}{25} / 50$ and $\frac{1}{10} / \frac{1}{5} / 10$, respectively. The result is shown in Figure 3.6(a) along with the reference one. For the cell with extremely high R_{sh} in the bottom subcell, the probed EQE strictly follow the genuine EQE of the bottom subcell in the wavelengths where the top subcell has a higher genuine EQE. When R_{sh} of the bottom subcell decreases, the probed EQE tends to present the spectral response of the top subcell, showing that the bottom subcell with low R_{sh} cannot properly limit the current in the device. This qualitative demonstration agrees with the trend reported by Pravettoni et al. and Bahro et al. [117], [137] With such adaption the model was greatly improved and specialized for simulating thin-film silicon-based solar cells, and can be applied to analyze the measurements conducted in the low-light regime.

Effect of low bias illumination

The effect of low bias illumination on the EQE measurement was investigated by implementing the adapted model. The reference tandem solar cell was simulated with the bottom subcell being the targeted subcell. The bias light for the top subcell was set at a high level of $J_{ph-top} = 20 \text{ mA/cm}^2$ in order to isolate the studied effect from other influences. The bias light for the bottom subcell was varied in a wide range: $J_{ph-bot} = 1.4 \times 10^{-4} - 1.4 \times 10^1 \text{ mA/cm}^2$. In all cases, the potential photocurrent generated in the top subcell was much higher than that in the bottom subcell. The probed EQE at zero V_{bias} is plotted in Figure 3.7(a). This series of EQE spectra exhibits very different features from the ones shown in the previous sections. First, there is barely any artifact signal at the wavelengths that the bottom subcell has zero genuine EQE. It is due to the intense light saturation in the top subcell that effectively prevents any artifacts caused by a voltage drift. Secondly, the probed EQE is higher than the genuine one. The enhancement in probed EQE increases monotonically with the decrease in J_{ph-bot} generated by bias light. This type of artifact can be ascribed to the illumination-dependent $J-V$ characteristics of the targeted subcell.

To explain this type of artifact, in Figure 3.7(b) the implied $J-V$ curves of the bottom subcell were examined with and without the probe light at 820 nm, the wavelength at which the top subcell is not active. In this low-light scenario, the bias-induced J_{ph-bot} is $1.4 \times 10^{-2} \text{ mA/cm}^2$, while at this wavelength the used monochromatic probe light generates a J_{ph-bot} of 0.2 mA/cm^2 . The difference in the currents at short-circuit points between the two $J-V$ curves is the J_{ph} supplied by the probe light thus directly related to the genuine EQE, while the corresponding difference at operation points decides the probed EQE. The R_{sh} in the two conditions are largely different, leading to different slopes between the two $J-V$ curves in their reverse-voltage regime. In consequence, the difference in the currents at operation points is enhanced from that at short-circuit points. A probed signal higher than the genuine EQE is formed, seeming an artifact.

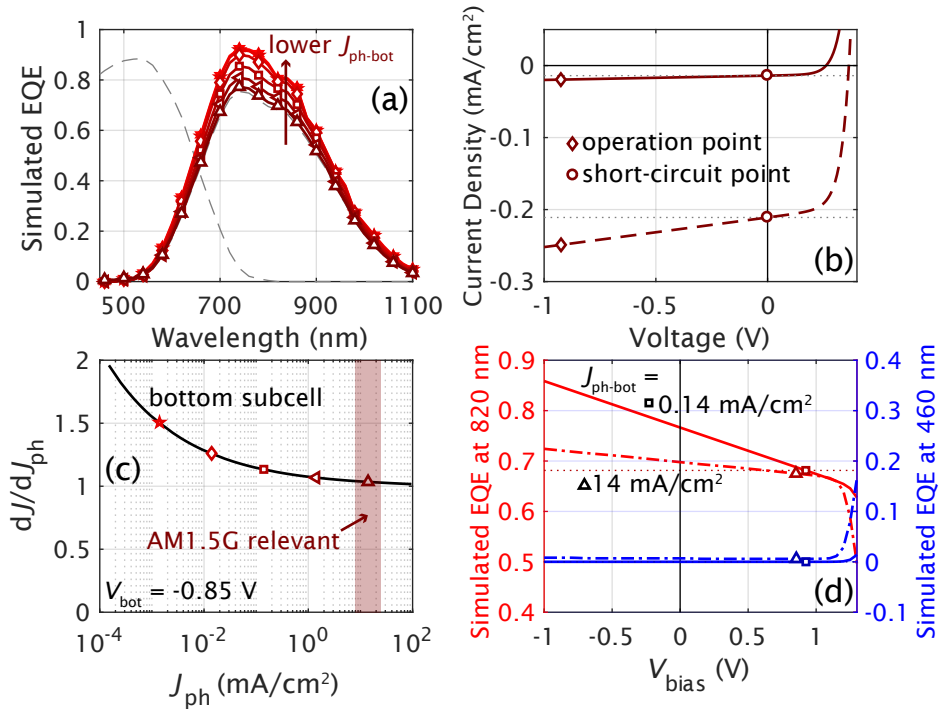


Figure 3.7: The probed EQE depends on the illumination level for the targeted subcell. (a) Probed EQE simulated with various bias illumination levels for the bottom subcell. The dashed lines show the genuine EQE of the two subcells. (b) Implied J - V curves of the bottom subcell without (solid line) and with (dashed line) 820 nm probe light, with the markers indicating the operation points and the short-circuit points. The dotted lines indicate the two J_{ph} levels. (c) The variation rate of the operation current of the bottom subcell at an operation voltage of -0.85 V, in response to the variation of J_{ph} . (d) Probed EQE simulated at 460 nm (blue) and 820 nm (red) in two different illumination levels. On each line a marker is placed at the point where the operation voltage of the targeted subcell is 0 V. The markers representing the illumination level are consistent across (a)–(d).

The probed EQE is subject to the illumination level as seen in Figure 3.7(a). The dependency originates from the principle of differential spectral response measurement, that the output signal is not the total current through the device over the total incident light, but the periodic component of the current, divided by the incoming chopped monochromatic light. In other words, the probed EQE depends on how fiercely the J - V characteristic changes with the additional incident light, at the particular illumination level. As an example, the bottom subcell in the adapted model was analyzed to assess how sensitive the operation current density is to J_{ph} . Such sensitivity was evaluated by dJ/dJ_{ph} , the derivative of the operation current density with respect to the potential photocurrent density. Examined at an operation voltage of -0.85 V, in Figure 3.7(c) the derivative is shown against the illumination level J_{ph} . Clearly, dJ/dJ_{ph} is not uniform throughout the inspected scope of illumination. Ideally, it equals 1 so the probed EQE matches the genuine EQE. Instead, its value is almost 2 in the darkest condition, and converges towards 1 in the high-illumination regime. It is the exact root of the varying signals in Figure 3.7(a).

In the simulations, the dependency of dJ/dJ_{ph} on J_{ph} is a direct consequence of the way how R_{sh} is interpolated in the adapted model. In actual measurements on a variety of multi-junction cells fabricated in different photovoltaic technologies, the cause of illumination-dependent response can be diverse. In general, a similar behavior can be expected whenever such derivative of operation current in the targeted subcell is not uniform over the relevant illumination range. This phenomenon illustrates the need of bias light even for the targeted subcell. Since the probed EQE is correlated with the amount of continuous J_{ph} in the subcell, the targeted subcell should be biased at an illumination level close to its intended operation condition, as commonly suggested [125].

In fact, in spite of the variance, the probed EQE spectra shown in Figure 3.7(a) do not contain much artifacts, but rather represent the EQE of the subcell at certain operation conditions, namely, under low bias light and negative operation voltage. The bias-light and bias-voltage dependences of EQE are not exclusive in the multi-junction cells but are rather common phenomena in single-junction cells [140].

Conventionally, the EQE of the subcell under an illumination near solar irradiation and at the short-circuit point is the main concern and was mostly reported. For that, a positive bias voltage is usually applied to compensate the voltage contribution from the non-targeted subcell(s) and to shift the operation point of the targeted subcell to the desired voltage. Figure 3.7(d) shows the effect of the bias voltage under two different illumination levels. When V_{bias} applied to the tandem cell is 0 V, the probed EQE gives different values in the two conditions. The dependency of probed EQE on V_{bias} is more obvious in case of low J_{ph-bot} , except for very high V_{bias} . By applying a V_{bias} equal to the operation voltage of the top subcell, the bottom subcell operates in the vicinity of 0 V, so the genuine EQE can be approached in both scenarios (For $J_{ph-bot} = 14$ mA/cm², there is a slight artifact because of the voltage drift in the top subcell). From the view point of actual measurements, however, it also means that the probed EQE changes continuously with V_{bias} and there is no clear signature to distinguish the optimal V_{bias} . Of course, in the high-voltage regime the probed EQE spectrum is largely distorted on account of both subcells operating at high forward voltages, so the upper limit of V_{bias} can be decided. For a more precise optimization

of the bias configuration, further analyses by modelling or additional experiments are required.

3.5.5 Experimental application

The purpose of developing the model in this work is to understand the formation of artifacts in EQE measurements so that the artifacts embedded in experimental results can be distinguished from the genuine properties of interest. Tandem solar cells, the multi-junction cells which consist of the least component subcells, were studied in the previous sections, because the limited complexity eases the analysis on artifact formation. When there are three or more subcells in a multi-junction cell, the internal correlations are complicated with the increased variables in the circuit, while the number of terminal is kept the same at two. In experiments, it becomes difficult to interpret the measurement results solely by adjusting the bias configurations. Nevertheless, the principles of the interactions between the subcells are similar no matter how many of them the multi-junction cell comprises. The model can therefore be used for interpreting those intricate experimental results.

As a demonstration of the experimental usage of our model, the model was applied to the measurements of a quadruple-junction thin-film $a\text{-SiO}_x\text{:H} / a\text{-Si:H} / nc\text{-Si:H} / nc\text{-Si:H}$ solar cell. The structure and performance of a similar cell have been reported elsewhere [98]. As a result of the absorber selection and optical design in such devices, the EQE spectra of the subcells strongly overlap with each other in the spectrum, as shown in Figure 3.8(a). The measurements on these cells typically feature a demanding process of adjusting the bias light. Besides, it can be observed in the measurement results that not only the intensity, but also the spectral profile of the probed EQE can sometimes be changed with varied bias voltage. An example is shown in Figure 3.8(b). During the measurement, the bias light was provided by three LEDs with emission peaks at the wavelengths of 447.5 nm, 470 nm and 530 nm, respectively, with the intent to saturate the first, second and third subcells. The three curves plotted in the figure were measured with a bias voltage of -0.2 V , 1.4 V and 2.4 V , respectively. Comparing to the reference spectra in Figure 3.8(a), at V_{bias} of -0.2 V , the probed EQE looks like what can be expected from the third subcell. In the transition from -0.2 V to 1.4 V , the onset of the probed EQE was shifted to the wavelength at which the fourth subcell should start to react. When V_{bias} was further increased, the signal declined in intensity, but extended to the short wavelengths at which the previous two measurements at lower V_{bias} received no response. This kind of evolution is not commonly expected from the adjustment of bias voltage. Incidentally, the discontinuity around 850 nm in all three curves is just an artifact induced by the specific measurement setup.

To explicate the origin of the irregular EQE being observed, simulations of the measurements on this device were performed. Figure 3.8(c) and (d) show the implied J - V curves of all four component subcells as well as the J - V curve of entire cell, under the illumination of only bias light. It should be noted that the additional part of the J_{ph} generated by probe light is only in the order of 10^{-2} mA/cm^2 when the subcell has a high response at that wavelength. Therefore, the situation with probe light was not depicted for a better clarity of the graph. The implied J - V characteristics

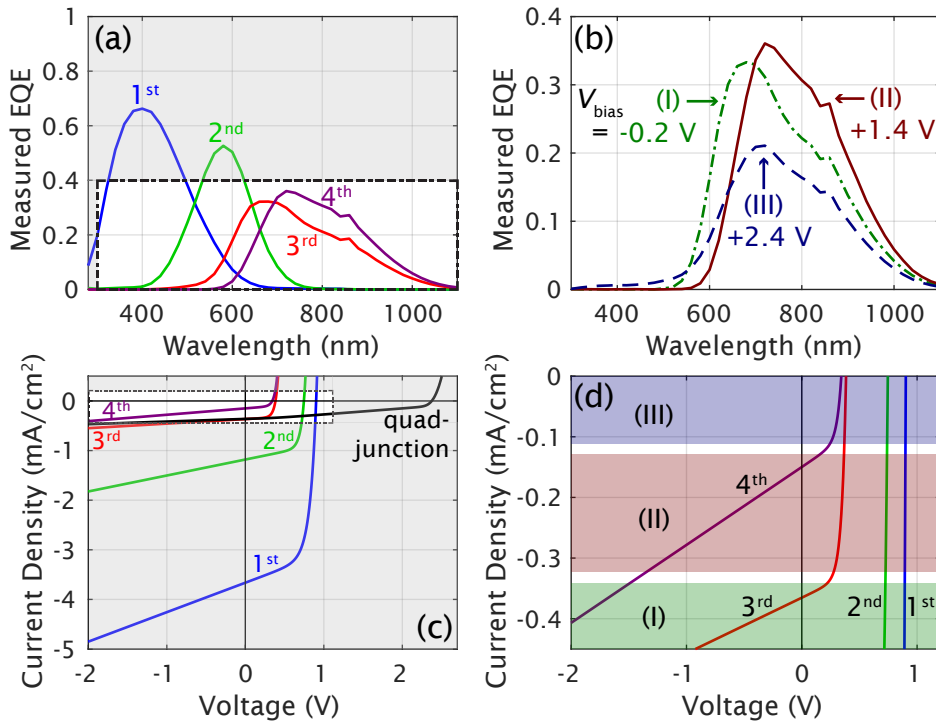


Figure 3.8: Voltage-dependent EQE measurements of a quadruple-junction cell. (a) Genuie EQE spectra of the four component subcells. (b) Experimentally measured EQE spectra show different spectral profiles with varied V_{bias} and fixed bias light configuration. Note that the chart has a same scale as the unshaded area in (a). (c) Simulated $J-V$ curve of the quadruple-junction cell, and the implied $J-V$ curves of the four component subcells under only bias illumination. (d) The unshaded area in (c), which is the part more relevant to the cell operation during the measurements. The graph is divided and rendered into three operation regimes corresponding to the three probed spectra in (b).

are the core of the dependency on V_{bias} shown in Figure 3.8(b). It can be seen that the fourth subcell has the least J_{ph} under the bias light, followed by the third subcell. The bias-induced J_{ph} in the subcells are, from the first to the fourth, $3.7/1.2/3.7 \times 10^{-1}/1.5 \times 10^{-1}$ mA/cm². The graph of implied J - V curves can be divided into three regimes, each of which corresponds to a probed EQE spectrum in Figure 3.8(b). In regime (I) where the external bias voltage is at the lower end, the fourth subcell operates at a high reverse voltage supplied by the other subcells. The amplitude of operation current is so high that the third subcell also operates in its low-conductance (dJ/dV) regime. When R_{sh} of the third subcell is higher than that of the fourth subcell, the operation current is throttled by the third subcell so it dominates the probed EQE, as seen in Figure 3.8(b). In regime (II), with a higher V_{bias} , all subcells except the fourth one operate near their V_{OC} , so the probed EQE mainly presents the photoresponse of the fourth subcell. If V_{bias} further increases, the cell is in regime (III) where all the subcells operate near their V_{OC} . The probed EQE contains the influences from all subcells with different weights related to the differential conductance dJ/dV in the individual subcells at their operation points. As a result, the probed EQE had non-zero values in the wavelength range below 500 nm, where the third and fourth subcells should have zero response.

In the above example, the simulations helped to explain the irregular response observed in experiments, which is the spectrally inhomogeneous dependency of the measured EQE on bias voltage. More importantly, it reflects the capability of the model to identify the sources of the probed EQE obtained in experiments, that is of significant importance in the research and development of two-terminal multi-junction solar cells.

3.6 On the proper measurement configuration and interpretation

It has been demonstrated so far that the signal collected in a EQE measurement of a two-terminal multi-junction cell is subject to the measurement configuration including the bias light, probe light and bias voltage. Such dependency originates from the electrical correlations between the component subcells as well as the optoelectrical characteristics of each subcell as an individual photovoltaic device. The configuration of a measurement is inherent not only in the measuring process but also in the data interpretation, of which people are not always aware. Concerning the EQE measurement, there are two natural questions and they should always come as a duo— “*What configuration?*” and “*What does the result mean?*”

With regard to single-junction cells, one may think of a few different measurement configurations. In all cases, the bias light should provide an illumination similar to AM1.5G or other interested spectrum, while the intensity of the probe light should be negligible and only result in a perturbation in the current. Depending on the purpose of the measurement, there are a few sensible choices of bias voltage which lead to different interpretations. First, the short-circuit condition that $V_{\text{bias}} = 0$ V is the most commonly used. The integration of EQE measured and weighted by the incident spectrum gives the J_{SC} of the cell. Secondly, the cell can be biased as $V_{\text{bias}} = V_{\text{MPP}}$ where V_{MPP} is the operation voltage of the cell at its maximum power point. This

might be more relevant to the actual operation of a solar cell and shows spectrally how photocarriers are generated and collected under such condition. Lastly, in some occasions a V_{bias} of negative value is used to enhance the carrier collection and reduce the recombination losses so that the effective optical absorption can be revealed.

The measurement of two-terminal multi-junction cells requires essentially different configurations and interpretations compared to the single-junction. These distinctions deserve more attention than what they have been given. The concepts used in measuring single-junction cells cannot be directly transferred. Setting V_{bias} at 0V or V_{MPP} of a multi-junction cell apparently does not give access to the EQE of its component subcells in their short-circuit or maximum-power-point condition because of the nature of two-terminal structure. Every single measurement is supposed to examine only one of the subcells, and the bias configuration should be designed for it. In terms of bias voltage, $V_{\text{bias}} = 0\text{V}$ lets the targeted subcell operate at a reverse voltage decided by the other subcells. This effortless setting is clearly not a good option because it is susceptible to artifacts as shown previously, meanwhile, is not related to any relevant operation condition of the multi-junction cell.

By applying a certain positive V_{bias} , the EQE of a subcell can be examined at its own short-circuit point. This method was widely reported in literature [115], [116], [119], [121]–[125], [141], [142]. On one hand, it gives useful information of how the incident photons can be distributed and utilized in different subcells, thus an important means to obtain the feedback needed for optimizing the cell fabrication and achieving current matching between the subcells. On the other hand, the short-circuit points of the subcells do not correlate with the short-circuit point nor other relevant operation conditions of the whole device under solar irradiation. Many researchers calculated the so-called J_{SC} of the subcells from the EQE spectra obtained by this method, and further assigned the lowest value among these J_{SC} of the subcells as the J_{SC} of the multi-junction cell based on the principle of current limitation in a series connection. Such interpretation, however, is not rigorous. The problem is illustrated in Figure 3.9(a). This example assumed a tandem cell similar to the ones simulated in the previous sections. The R_{sh} of the top and bottom subcells is at reasonably high value of $1000\ \Omega\ \text{cm}^2$ and $750\ \Omega\ \text{cm}^2$, respectively. Under AM1.5G illumination, the top and bottom subcells generate current densities J_{ph} of $14.0\ \text{mA}/\text{cm}^2$ and $14.5\ \text{mA}/\text{cm}^2$, respectively, at the short-circuit points of their implied J - V curves. Following the conventional approach one may report a J_{SC} of $14.0\ \text{mA}/\text{cm}^2$ based on the measured EQE of the two subcells, but in Figure 3.9(a) the J - V curve of the tandem cell shows that the J_{SC} is actually $14.2\ \text{mA}/\text{cm}^2$. The curves in Figure 3.9(a) were simulated according to the assumed J_{ph} of the subcells, and they conform to the requirement of perfect series connection. In case these equations are held in a multi-junction cell, it can be mathematically proven that the J_{SC} of the multi-junction cell is always greater than the lowest J_{ph} among the component subcells. Therefore, EQE of the subcells measured at their own short-circuit points may not give the J_{SC} of the multi-junction cell with satisfactory accuracy, despite the useful information which they deliver.

To give an estimation of the possible discrepancy, the J - V characteristics of a tandem solar cell are considered. In a tandem cell where the subcell #1 provides less J_{ph} under AM1.5G than the subcell #2 does, as exemplified in Figure 3.9(b), the discrepancy between the J_{SC} of the tandem cell and the lowest J_{ph} among the component subcells

is:

$$\Delta J \approx V_1 \cdot [dJ/dV]_1|_{(V=0)} \approx -V_2 \cdot R_{sh1}^{-1} \quad (3.4)$$

For a reasonably current-matched tandem solar cell, the practical upper limit of $|\Delta J|$ can be approximated at $V_{MPP2} \cdot R_{sh1}^{-1}$, where V_{MPP2} is the voltage of the maximum power point around which the slope of the implied J - V of subcell #2 changes abruptly. Based on this estimation, if $V_{MPP2} = 0.5 \text{ V}$, the maximum discrepancy ΔJ is 0.5 mA/cm^2 and 0.05 mA/cm^2 for a R_{sh1} of $1 \text{ k}\Omega \text{ cm}^2$ and $10 \text{ k}\Omega \text{ cm}^2$, respectively. Therefore, the discrepancy in the J_{SC} determined by EQE measurements is not always negligible when the R_{sh} of the subcell is a few $\text{k}\Omega \text{ cm}^2$ or lower.

When a certain operation condition of a multi-junction cell is of interest, the EQE measurement of its component subcells should also be related to such condition. To proceed with the measurements, the determination of measurement configurations should involve multiple steps:

1. Decide the interested operation condition of the multi-junction cell, based on the purpose of the study.
2. Find the operation condition of the targeted subcell corresponding to the interested operation condition of the multi-junction cell. This is the condition in which the subcell should operate during the measurement.
3. Set up a measurement configuration to fulfill the required operation condition of the targeted subcell, and to properly bias the rest of the subcells at the same time.

For example, to investigate the tandem cell in Figure 3.9(a) under AM1.5G illumination and in short-circuit condition, the targeted subcell should be biased to the corresponding operation point indicated in the figure. Measuring the top subcell requires the bias light supplying a J_{ph} of 14.0 mA/cm^2 for the top subcell and much more for the bottom. The bias voltage should be applied such that the operation voltage of the top subcell is -0.22 V . Accordingly, when measuring the bottom subcell, it should have a J_{ph} of 14.5 mA/cm^2 and an operation voltage of 0.22 V . Nevertheless, it should be noted that this type of measurement requires extensive knowledge of the multi-junction cell being investigated, which may be obtained by optical and electrical simulations and some preliminary measurements. It might be used for the in-depth analysis of a device, but it is certainly not a means of finding the J_{SC} of a multi-junction cell.

Having discussed various possible measurement configurations, it turns out that the spectral response measurement of two-terminal multi-junction solar cells cannot be used as a tool to precisely determine the J_{SC} . Instead, the measurement provides a great deal of information about the component subcells, which may then be used to approximate the J_{SC} of the multi-junction cell. The accuracy of the estimation can be improved by J - V analysis similar to that in Figure 3.9.

3.7 Outlook

Besides the understanding of certain artifacts as an obvious outcome, the motivation of developing such a model in this work is to bring up the awareness of measurement

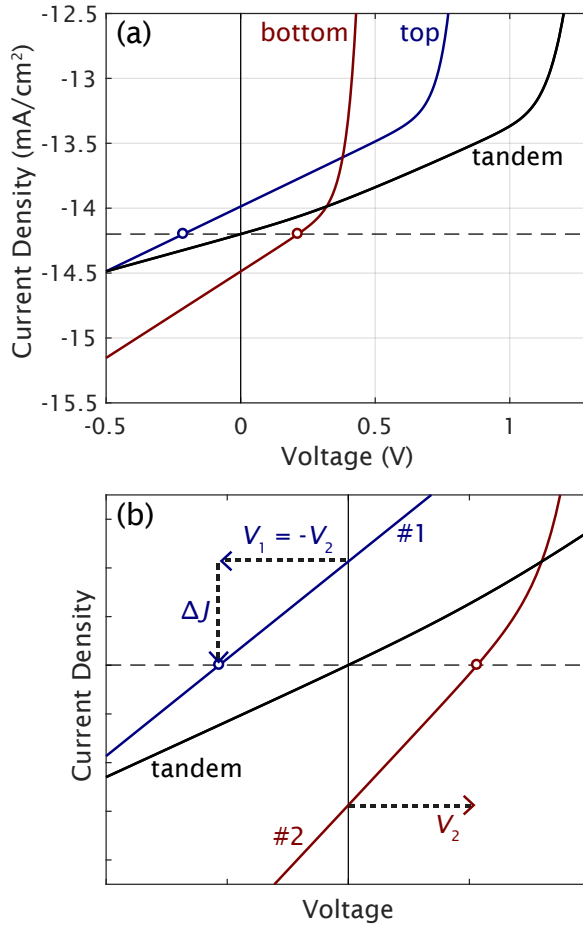


Figure 3.9: J - V and implied J - V curves of a tandem cell and its component subcells, respectively, under the illumination of AM1.5G spectrum. The dashed line indicates the J_{SC} of the tandem cell. The opened circles on the implied J - V curves show the operation points of the subcells when the tandem cell is in short-circuit condition. (a) A specific tandem cell as an example. (b) Estimation of the possible discrepancy ΔJ .

artifacts, so as to promote reliable characterizations and accurate reporting in the field of photovoltaic research. The model was demonstrated with thin-film silicon-based solar cells, but its application is more generic, covering the multi-junction cells made with various photovoltaic technologies. As suggested in Fig. 3.1, supplementary physical models can be inserted at different parts in the flowchart to adapt the model to different types of solar cell, so that the specific characteristics related to their constituting materials can be accurately described and simulated. The adaption made in Section 3.5.4 for describing the illumination-dependent J - V characteristics is an example. Similarly, modifications can be made for the nonlinear J_{SC} -irradiance behavior [143], [144] and the photoshunt effect [145] in organic solar cells, or for the luminescence coupling effect [118], [146] in solar cells consisting of III-V semiconductors, etc. With such extensibility, the model is useful for the experimental study of two-terminal multi-junction solar cells made of novel combinations of absorber materials, and for the cells with unfamiliar or complex spectral response. By simulating the response of solar cells to diverse bias conditions (the preliminary input about spectral response can be generated by optical simulations [98], [141], [143]), the appropriate measurement configurations can be quickly approached. It is particularly important nowadays considering the emergence of many novel hybrid multi-junction structures.

3.8 Conclusions

Having the incident spectrum and bias voltage to construct a virtual measurement condition, our model proposed a generic way to simulate the internal activities of a two-terminal multi-junction solar cell during the process of spectral response measurements. By simulations, sources of artifact formation have been examined. Internally, the influence of shunt resistance in the targeted subcell was confirmed that lower shunt resistance leads to greater voltage drift in other subcell(s) thus more undesirable change to the probed EQE. Externally, the impact of bias conditions was investigated, including the bias-light intensity for the targeted and non-targeted subcells, as well as the bias voltage applied to the two terminals. In brief, the spectral response of the subcell with the lowest differential conductance dJ/dV at its operation point in the measurement condition has the most representation in the probed EQE. Because of the effects of the bias configurations on the operation conditions, a high bias-induced photocurrent(s) in the non-targeted subcell(s) and a medium bias voltage generally help to avoid measurement artifacts. If the J - V characteristic of the targeted subcell deforms with the illumination level and the operation current does not grow linearly with the photocurrent, the probed EQE will be dependent on the bias-light intensity for the targeted subcell beside the bias voltage. Thus the bias conditions for measurements should be configured according to the intended working condition of the multi-junction cell.

Making use of the extra information from the model, the changes in the actually measured EQE in a quadruple-junction thin-film silicon-based solar cell with varied bias voltage were elucidated. It demonstrated how the modeling tool can assist the EQE measurements of multi-junction cells. Not only it can make the acquired results less ambiguous, but combining with other optical or opto-electrical simulations it can

also estimate the optimal bias configuration for an unfamiliar device even ahead of the actual experimental attempt. Such capability will be helpful in the research and development of two-terminal multi-junction solar cells, especially the ones with novel or uncommon device structure.

Finally, attentions were raised to the interpretation of the measured spectral response. The EQE of the component subcells is meaningful information but generally it cannot be directly translated into the short-circuit current density of the multi-junction cell. It was suggested that EQE measurements should be performed in a way that the measured EQE is related to a certain interested/relevant operation condition of the multi-junction cell.

4

Thin-film amorphous silicon germanium solar cells with p- and n-type hydrogenated silicon oxide layers

This chapter was published in *Solar Energy Materials and Solar Cells* [147].

Abstract

Mixed-phase hydrogenated silicon oxide ($\text{SiO}_x\text{:H}$) is applied to hydrogenated amorphous silicon germanium ($\text{a-SiGe}_x\text{:H}$) cells serving as both p-doped and n-doped layers. The bandgap of p- $\text{SiO}_x\text{:H}$ is adjusted to achieve a highly-transparent window layer while also providing a strong electric field. Bandgap grading of n- $\text{SiO}_x\text{:H}$ is designed to obtain a smooth transition of the energy band edge from the intrinsic to n-doped layer, without the need of an amorphous buffer layer. With the optimized optical and electrical structure, a high conversion efficiency of 9.41 % has been achieved. Having eliminated other doped materials without sacrificing performance, the sole use of $\text{SiO}_x\text{:H}$ in the doped layers of $\text{a-SiGe}_x\text{:H}$ cells opens up great flexibility in the design of high-efficiency multi-junction thin-film silicon-based solar cells.

4.1 Introduction

Hydrogenated amorphous silicon germanium (a-SiGe_x:H) is a meaningful building block in multi-junction thin-film silicon-based solar cells. Its electronic bandgap decreases as the Ge content increases in the matrix [17], [148], [149]. As an absorber material, a-SiGe_x:H offers an adjustable, intermediate bandgap between those given by the widely used hydrogenated amorphous silicon (a-Si:H, 1.7 eV) and hydrogenated nanocrystalline silicon (nc-Si:H, 1.1 eV). A combination of these absorbers can lead to better spectral utilization in triple- and quadruple-junction solar cells [80], [127], [150], [151].

To form a p-i-n junction, p-type hydrogenated amorphous silicon carbide (a-SiC:H), a-Si:H, nc-Si:H, hydrogenated silicon oxide (SiO_x:H), and n-type a-Si:H, nc-Si:H, SiO_x:H have been used in the p- and n-layer, respectively, of a-SiGe_x:H solar cells. Among these materials, SiO_x:H is worth extra attention because of its multifunctionality and adaptability demonstrated in the application of thin-film silicon-based solar cells. SiO_x:H is a mixed-phase material comprising nanocrystalline silicon filaments embedded in an amorphous silicon oxide matrix [85], [87], [152]–[156]. The anisotropic growth of the material results in good transverse and poor lateral conductivity, thus improving the electrical performance of the solar cell. Optically, its relatively wide bandgap and low absorption coefficient suppress own parasitic absorption, while providing a high built-in voltage as a p-layer. The tunable refractive index offers a means to reduce the reflection at the window layer, or to enhance the intermediate reflection when used after an absorber layer [80], [84], [89], [90]. Given that well-performing tunnel recombination junctions (TRJs) can be formed between p-type and n-type SiO_x:H [90], SiO_x:H opens a great versatility for the light management in multi-junction solar cells. Lastly, n-type SiO_x:H/Ag was also used to replace the typical ZnO:Al/Ag back reflector, as the low refractive index of SiO_x:H can limit the plasmonic absorption in Ag [29], [86], [88], just like in ZnO:Al/Ag stack. Figure 4.1 shows the optical properties of the p- and n-type SiO_x:H, in comparison to other typical materials used in a-SiGe_x:H cells.

So far, the use of SiO_x:H in a-SiGe_x:H solar cells is not as popular as it is in a-Si:H or nc-Si:H cells. N-type SiO_x:H has been used as the n-layer of a-SiGe_x:H cells behind either intrinsic a-Si:H [127] or a-Si:H/nc-Si:H [157] buffer layer(s). On the p-side, Schüttauf et al. tested several p-layer configurations and a significant drop in V_{OC} was observed in the sample that the p-layer was solely constituted of p-type SiO_x:H, compared to those which also include a a-SiC:H or a-Si:H layer between the oxide layer and the absorber [127]. Nevertheless, taking into account the adaptability of SiO_x:H materials and its successful applications in a-Si:H and nc-Si:H solar cells, it is natural to think of making a a-SiGe_x:H cell using only SiO_x:H for the doped layers, without compromising the performance. From the optical perspective, it can reduce the parasitic absorption caused by the other more absorptive supporting materials, and at the same time provide the most flexibility in light management for both single- and multi-junction devices. Electrically, the doped SiO_x:H materials can be tuned such that they give favorable band offset at the interfaces, or form efficient TRJs with minimized losses. In this paper, we explore the possibility of using both p- and n-type SiO_x:H in thin-film a-SiGe_x:H solar cells without extra buffer layers adjacent to the

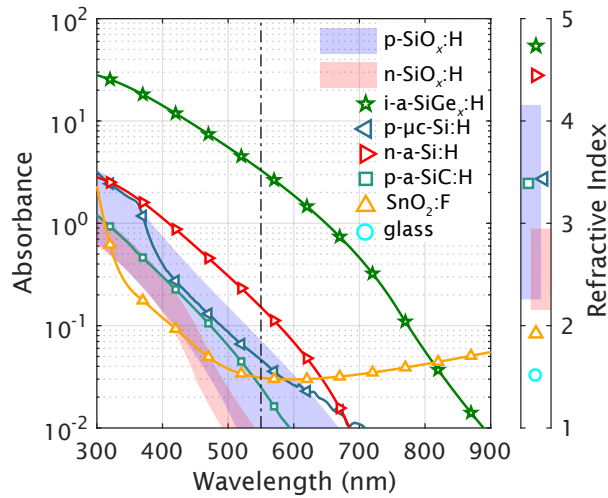


Figure 4.1: Optical properties of typical materials used in a-SiGe_x:H solar cells: (Left) Absorbance $A = \alpha \cdot d$, where α is the absorption coefficient and d is the typical thickness of the material used in a device; (Right) Refractive index at wavelength $\lambda = 550$ nm. The shaded areas in blue and red color represent the adjustable properties of p and n-type SiO_x:H, respectively.

absorber layer, and further optimize the light management of such device.

4.2 Experimental

The thin-film silicon-based alloy materials, including intrinsic a-SiGe_x:H, p- and n-type SiO_x:H and n-type a-Si:H, were deposited in a cluster tool using plasma-enhanced chemical vapor deposition (PECVD) at radio frequency (RF) of 13.56 MHz. The maximum substrate area and electrode area are 100 cm² and 144 cm² in square, respectively. Silane, germane and carbon dioxide were used as the source of silicon, germanium and oxygen, respectively. Diborane and phosphane (phosphine) were used as the doping gas for the p- and n-type materials, respectively. The deposition conditions of the PECVD materials are summarized in Table 4.1.

Thin-film a-SiGe_x:H solar cells were deposited on glass coated with nanotextured SnO₂:F (Asahi VU-type, Asahi Glass Co., Ltd. [158]) in superstrate p-i-n configuration. The typical device structure is glass/SnO₂:F/ZnO:Al/p-layer/i-a-SiGe_x:H/n-layer/Ag/Cr/Al. A thin layer of 20-nm-thick ZnO:Al was deposited using RF magnetron sputtering to protect the SnO₂:F against hydrogen plasma in the PECVD process [159]. The p-layer consists of a 4-nm-thick p-nc-Si:H on top of the front transparent conductive oxide (TCO) forming a good ohmic contact [156], and a 12-nm-thick p-SiO_x:H as the main p-type material for providing the electric field. The total thickness of the intrinsic a-SiGe_x:H is 200 nm. To mitigate the transportation barrier caused by the misalignment of energy bands between the intrinsic and doped

	p-nc-Si:H	p-SiO _x :H	i-a-SiGe _x :H	n-a-Si:H	n-SiO _x :H
<i>T</i> (°C)			180		
<i>p</i> (mbar)	2.2	2.2	3.6	0.6	1.5
<i>P</i> (mW/cm ²)	243.1	90.3	20.8	27.8	69.4
SiH ₄	0.8	0.8	30.0	40.0	1.0
GeH ₄	—	—	3.65	—	—
H ₂	190	190	200	10.8	101
B ₂ H ₆	0.004	0.004	—	—	—
PH ₃	—	—	—	0.22	0.024
CO ₂	—	0.8~2.2	—	—	0.5~2.6
rate (nm/min)	4.0	1.4~1.8	10.5	4.0	1.0~1.3

Table 4.1: Deposition conditions of the PECVD materials used in this work. The constitution of gaseous precursors is shown by their flow rates in standard cubic centimeter per minute (sccm). The bottom row shows the deposition rate of the materials.

materials [160]–[163], U-shape bandgap grading was applied by linearly reducing the GeH₄ flow in the a-SiGe_x:H deposition near the p-i and i-n interfaces. The thickness of the graded layers is 70 nm and 50 nm at the p- and n-side, respectively. It leaves the middle part of the intrinsic layer, which has the lowest bandgap, 80 nm in thickness. The n-layer is made of either n-a-Si:H, n-SiO_x:H, or a combination of the two. The Ag/Cr/Al metal stack with thicknesses of 300/30/800 nm serves as the back reflector as well as back electrode. It was deposited by thermal (Ag) or e-beam (Cr/Al) evaporation with a shadow mask so that the patterned metallic pad also defines the cell area. There are 30 cells on each sample and each cell has a squared area of 16 cm². Cell isolation was completed by etching away the materials outside the metal pads using anisotropic reactive ion etching (RIE). In occasions that ZnO:Al is used after the deposition of n-layer, the samples were dipped in diluted hydrochloric acid to remove the ZnO:Al prior to RIE.

The optical properties of the thin-film materials were characterized by spectroscopic ellipsometry (SE). The measurements were conducted at multiple incident angles using an M-2000D1[®] Spectroscopic Ellipsometer (J.A. Woollam Co.), which is equipped with a dual-lamp light source covering the wavelength range of 193–1690 nm. To determine the optical bandgap of a-SiGe_x:H, the Tauc-Lorentz model [164], [165] was fitted to the SE data measured from samples of single thin films deposited on glass substrates, and the result gave the optical bandgap E_{Tauc} . Alternatively, optical bandgap E_{04} was found as the energy with which a photon has an absorption coefficient of $1 \times 10^4/\text{cm}$ in the material.

The performance of the solar cells was examined by the illuminated current-voltage (*I-V*) measurement and external quantum efficiency (EQE) measurement. The *I-V* measurement was conducted at a controlled cell temperature of 25 °C, with a dual-lamp continuous solar simulator (WACOM WXS-90S-L2, class AAA). The two filtered lamps in the solar simulator were adjusted with two monocrystalline silicon reference cells manufactured by and traceable to the Fraunhofer Institute for Solar Energy Systems

(ISE), to provide an incident irradiance of 1000 W/m² with optimum spectral matching with AM1.5G solar spectrum. The EQE measurement was performed using an in-house system, in which the electrical signal is detected by a lock-in amplifier, and the chopped monochromatic light is provided by a xenon light source, a 3-grating monochromator and a chopper. A silicon photodiode, which was regularly calibrated by Fraunhofer ISE, was used to calibrate the light source in the EQE measurement. As for the external parameters of the solar cells, the open-circuit voltage (V_{OC}) and fill-factor (FF) are determined by the I - V measurement, while the short-circuit current density (J_{SC}) is calculated by weighting the measured EQE with the AM1.5G solar spectrum. The cell performance reported in this work is the average taken from the 12 better performing cells (60%) out of the 30 cells on each sample. While the EQE measurement was conducted on the best performing cell in each sample, the reported deviation in J_{SC} was obtained from the J - V measurement.

4.3 Use of SiO_x:H in p-layer

In this section, p-SiO_x:H is applied in a-SiGe_x:H cells as the main p-layer, and the cell performance is examined. To compare the effect of different p-SiO_x:H, the device structure except the p-layer was kept the same as described in Section 4.2. No buffer layers were used between the p-i nor i-n interface. A series of solar cells were fabricated with different CO₂ flow rate during the deposition of p-layer. The different oxygen content in p-SiO_x:H results in different optical bandgap and electrical conductivity of the material [90].

The optical effect of the different p-SiO_x:H layers is first investigated. The p-layers were deposited with a flow rate ratio $R[\text{CO}_2/\text{SiH}_4]$ from 1.00 to 2.75. External quantum efficiency was measured at a bias voltage of -0.5V to reduce the influence of inefficient carrier collection and to estimate the optical absorption in the absorber layer. The measured result is shown in Figure 4.2. It is clear that in the short wavelengths between 300 nm and 600 nm, the greater the CO₂ flow during the p-layer deposition, the higher spectral response the solar cell exhibits. The difference in blue response mainly comes from the parasitic absorption in the p-layer. With more CO₂, the deposited p-SiO_x:H has a larger optical bandgap and lower absorption coefficient, so it allows more high-energy photons to be utilized in the intrinsic layer and contribute to the photocurrent. Beyond 600 nm, the EQE is very similar between the cells (not shown) because the p-layers barely absorb any photons in that region.

Electrically, the cells in Figure 4.2 show similar performance. With a lowest E_{Tauc} (E_{04}) of 1.41 eV (1.62 eV) in the intrinsic layer, all cells have a FF in the range of 54% - 56%, as shown in Figure 4.3. The V_{OC} shows a slight still monotonic increase with increased CO₂, from 654 mV to 660 mV. For a a-SiGe_x:H absorber with a wider bandgap, however, the p-SiO_x:H has a greater impact on the electrical performance of the solar cell. When the absorber has an E_{Tauc} (E_{04}) of 1.45 eV (1.67 eV) at its lowest point, both V_{OC} and FF show a monotonic increase with ratio $R[\text{CO}_2/\text{SiH}_4]$, in the range of 1.00 - 2.75. Overall, the p-SiO_x:H with a wider bandgap gives a better performance in the solar cell, provided that the p-layer still has sufficient transverse conductivity.

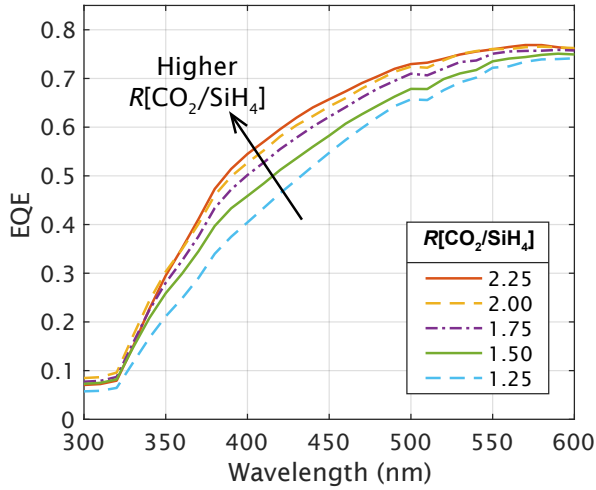


Figure 4.2: EQE of a-SiGe_x:H cells with p-layers deposited at different concentration of CO₂. The spectra were measured at bias voltage $V_{\text{bias}} = -0.5\text{V}$, to feature the optical effect.

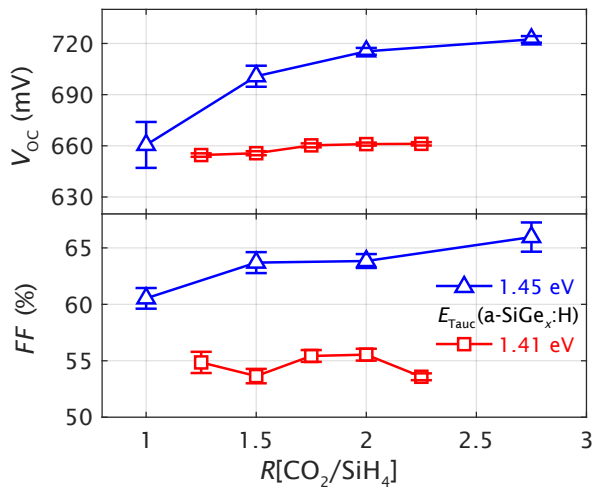


Figure 4.3: External parameters V_{OC} and FF of a-SiGe_x:H cells with p-SiO_x:H made with different ratio of $R[\text{CO}_2/\text{SiH}_4]$.

#	Configuration
<i>a</i>	20 nm n-a-Si:H
<i>b</i>	20 nm n-a-Si:H / 60 nm n-SiO _x :H
<i>c</i>	10 nm n-a-Si:H / 60 nm n-SiO _x :H
<i>d</i>	5 nm n-a-Si:H / 60 nm n-SiO _x :H
<i>e</i>	60 nm n-SiO _x :H
<i>f</i>	30 nm graded n-SiO _x :H / 30 nm n-SiO _x :H

Table 4.2: Configurations of n-layer tested for a-SiGe_x:H cells.

4.4 Use of $\text{SiO}_x\text{:H}$ in n-layer

In a-Si:H solar cells, both n-a-Si:H and n-SiO_x:H acting as the n-layer can lead to decent electrical performance of the cells. The use of n-SiO_x:H is more favorable when the optical losses and the behavior in forming TRJs [80], [166] are considered. Based on such experience, several configurations of n-layer have been tested in this work to see how well they work for a-SiGe_x:H cells. The tested structures are summarized in Table 4.2. Configurations *a* and *e* comprise only a single layer of n-a-Si:H and n-SiO_x:H, respectively. The ratio $R[\text{CO}_2/\text{SiH}_4]$ for n-SiO_x:H was chosen to be 2.0 after some preliminary optimization. Configuration *b*, *c*, and *d* have the same n-SiO_x:H layer as *e*, but with an n-a-Si:H layer between the n-SiO_x:H and the intrinsic layers. Lastly, the deposition of configuration *f* started with a bandgap grading of n-SiO_x:H, in which the ratio $R[\text{CO}_2/\text{SiH}_4]$ was gradually changed from 1.0 to 2.0. The second half of the n-SiO_x:H deposition was then continued at $R[\text{CO}_2/\text{SiH}_4]$ of 2.0. The influence of different n-layer configurations was examined by the performance of the solar cells. A series of a-SiGe_x:H cells were fabricated using identical device structure except for the n-layer. p-SiO_x:H with $R[\text{CO}_2/\text{SiH}_4] = 2.0$ was used as the p-layer and a-SiGe_x:H with a lowest E_{Tauc} of 1.45 eV was used as the i-layer.

The external parameters of the solar cells measured under AM1.5G spectrum are shown in Figure 4.4. It is the most noticeable that configuration *a* provides significantly less photocurrent than all the others do. In this structure, the cell performance suffers from severe plasmonic absorption at the Ag back reflector because the adjacent material, which is n-a-Si:H, has a high refractive index [88]. From configuration *a*, with an additional n-SiO_x:H layer acting as an optical spacer, configuration *b* exhibits improved J_{SC} and slightly dropped FF . When comparing configurations *b*, *c* and *d*, the reduction of n-a-Si:H thickness mitigates the parasitic absorption, leading to the increase in J_{SC} . Furthermore, shrinking the defective n-a-Si:H layer also slightly improves V_{OC} and FF . n-SiO_x:H can act as n-type material to provide the necessary electric field, so the role of n-a-Si:H in these configurations is more about interface passivation and diminishing band offset. Without such buffer in between, configuration *e* gives worse V_{OC} and FF probably because of the band discontinuity between the absorber and the wide-gap n-SiO_x:H. To tackle this problem without using n-a-Si:H, configuration *f* aims at achieving a smooth transition from the intrinsic layer to narrow-gap n-SiO_x:H to wide-gap n-SiO_x:H by means of CO₂ grading during the deposition. As a result, all external parameters are improved from configuration *e* to

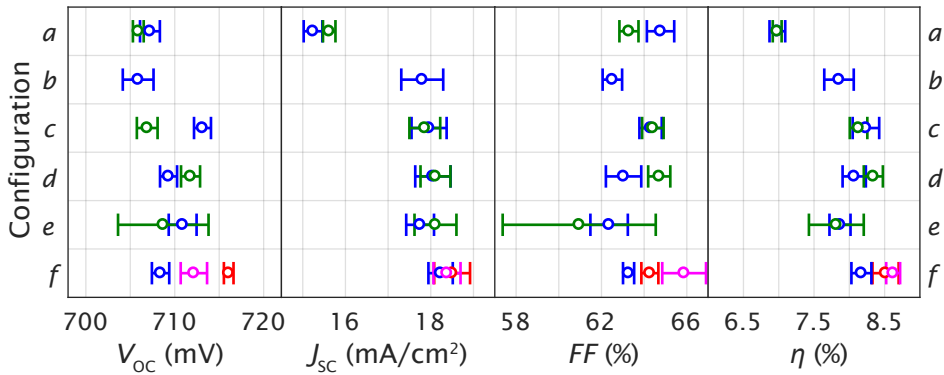


Figure 4.4: External parameters of a-SiGe_x:H cells with different configurations of the n-layer. The multiple data sets (different colors) in a configuration represent samples having the same nominal structure but made in different deposition runs. The error bars are the standard deviation showing the inhomogeneity among the cells within a sample.

f. Remarkably, this n-layer is solely constructed of n-SiO_x:H while its best sample tops the conversion efficiency among all compared configurations.

4.5 Optical spacer at back reflectors

It is demonstrated in Section 4.4 that because of its low refractive index, n-SiO_x:H can function as optical spacer at the back reflector to suppress the plasmonic absorption in Ag. Conventionally, ZnO:Al is used together with Ag back reflector for the same purpose [88]. On the other hand, the free carrier absorption in ZnO:Al [167] can potentially deteriorate the spectral response of the solar cell at long wavelengths.

In this section, we investigate the feasibility of fully replacing ZnO:Al with n-SiO_x:H in a-SiGe_x:H solar cells. A series of cells were fabricated with different configurations of optical spacer before the Ag back reflector. The basic structure includes p- and i-layers identical to the ones used in Section 4.4, as well as a 30-nm-thick n-SiO_x:H layer with bandgap grading. On top of it, wide-gap n-SiO_x:H and/or ZnO:Al with various thickness was deposited before completing the back reflector with Ag. The thicknesses of wide-gap n-SiO_x:H and ZnO:Al are 0/30 nm and 0/40/80/120 nm, respectively.

Figure 4.5 shows the measured EQE of the a-SiGe_x:H cells with different spacer configurations. Without an additional layer of wide-gap n-SiO_x:H, it can be clearly seen in Figure 4.5(a) that the spectral response at wavelengths longer than 700 nm is enhanced when the thickness of ZnO:Al is increased from 0 nm to 40 nm to 80 nm, showing the effect of ZnO:Al on reducing plasmonic absorption. When the thickness of ZnO:Al is further increased to 120 nm, the spectral response is not as good as the 80-nm-thick counterpart. We speculate that 80-nm-thick ZnO:Al is capable of quenching most of the plasmonic absorption so the extra thickness of 40 nm only increases the parasitic absorption in ZnO:Al.

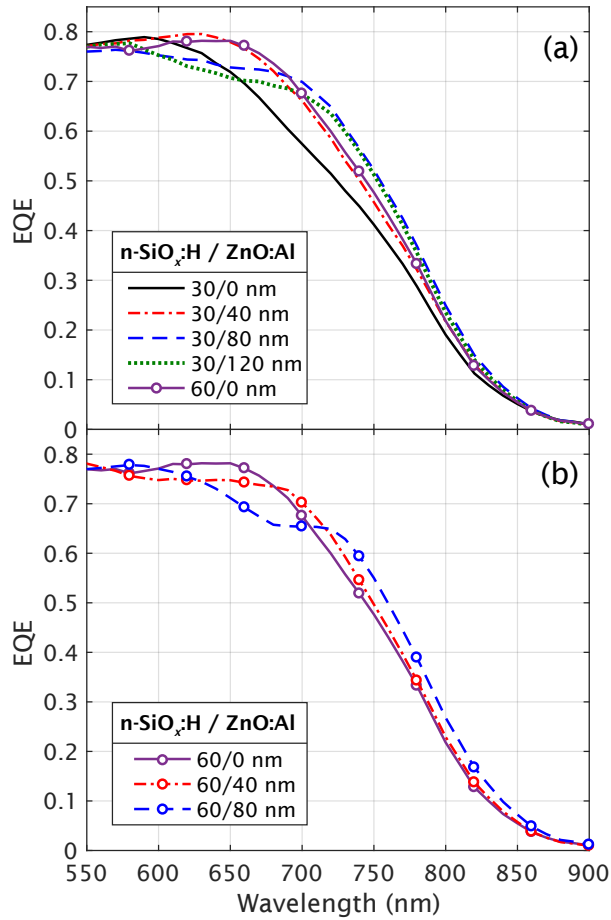


Figure 4.5: EQE of a-SiGe_x:H cells with different thicknesses of n-SiO_x:H and ZnO:Al in front of the back reflector. The thickness of n-SiO_x:H is (a) 30 nm or (b) 60 nm in total. The result of the cell with 60-nm-thick n-SiO_x:H and no ZnO:Al is also plotted in (a) to show the effect of the extended n-SiO_x:H.

A direct comparison in Figure 4.5(a) shows that the cell with 60/0 nm of n-SiO_x:H/ZnO:Al (i.e. no ZnO:Al) exhibits comparable spectral response to that of the cell with thinner n-SiO_x:H and 40-nm-thick ZnO:Al spacer. The addition of 30-nm-thick wide-gap n-SiO_x:H layer provides a similar effect as 40 nm of ZnO:Al. It confirms the capability of n-SiO_x:H material being an optical spacer to avoid parasitic losses. Figure 4.5(b) shows the EQE spectra of cells with different thickness of ZnO:Al on top of the extended n-SiO_x:H layer. A similar improvement in the long wavelengths is observed when the thickness of ZnO:Al is increased, even with the thicker n-SiO_x:H layer. Two remarks should be noted for clarification: Firstly, all solar cells reported in Figure 4.5 show similar V_{OC} and FF , so better spectral response can be translated to better cell performance. Secondly, the strong EQE variation between the samples in the wavelengths of 600 - 700 nm resembles the reflection spectrum of the respective cells (not shown). It is probably due to the interference effect, which is sensitive to the thickness of the films.

By extrapolation, one can expect comparable optical performance from replacing the thick ZnO:Al layer with a thick wide-gap n-SiO_x:H layer. Nonetheless, a thick wide-gap n-SiO_x:H layer can be too resistive to support efficient carrier transportation in the device. Therefore, a combination of n-SiO_x:H and ZnO:Al both with medium thickness should give the best overall performance.

4.6 Improvement by light scattering substrates

Light scattering is particularly important for a-SiGe_x:H solar cells. The intrinsic a-SiGe_x:H materials are rather defective compared to a-Si:H, so the absorber layer in a-SiGe_x:H cells has to be very thin to ensure adequate carrier collection efficiency of the device. Light scattering for enhancing the light absorption in the long wavelengths is therefore necessary for achieving high photocurrent within the thin absorber. In this section, the importance of light scattering for a-SiGe_x:H solar cells is highlighted by comparing cells fabricated on different light-scattering substrates.

The native roughness on APCVD SnO₂:F is too small to provide effective light scattering near the band edge of a-SiGe_x:H. On this respect, the surface of ZnO:B deposited by low-pressure CVD (LPCVD) typically features a greater roughness and larger (average) local surface inclination angle thus better light scattering capability among the longer wavelengths [168]. For comparison, solar cells were deposited on these two types of substrate, in specific, SnO₂:F (Asahi VU-type) and LPCVD ZnO:B with a thickness of 2.3 μm and smoothed by Ar plasma treatment for 4 min (The ZnO:B substrate was prepared by Dr. Hairen Tan during his visiting research at the PV-Lab of IMT, EPFL in Neuchâtel, Switzerland.) The optimized device structure being used contains p-SiO_x:H with $R[CO_2/SiH_4] = 2.0$, 60 nm of n-SiO_x:H with bandgap grading in its first half and $R[CO_2/SiH_4] = 2.0$ in the second half, and 40 nm of ZnO:Al. In addition, the hydrogen dilution during a-SiGe_x:H deposition was slightly increased to improve the material quality, while the ratio between SiH₄ and GeH₄ was maintained the same.

The performance of the optimized solar cells is shown in Figure 4.6. On Asahi-VU substrates, the optimized device structure using doped SiO_x:H for both p- and n-

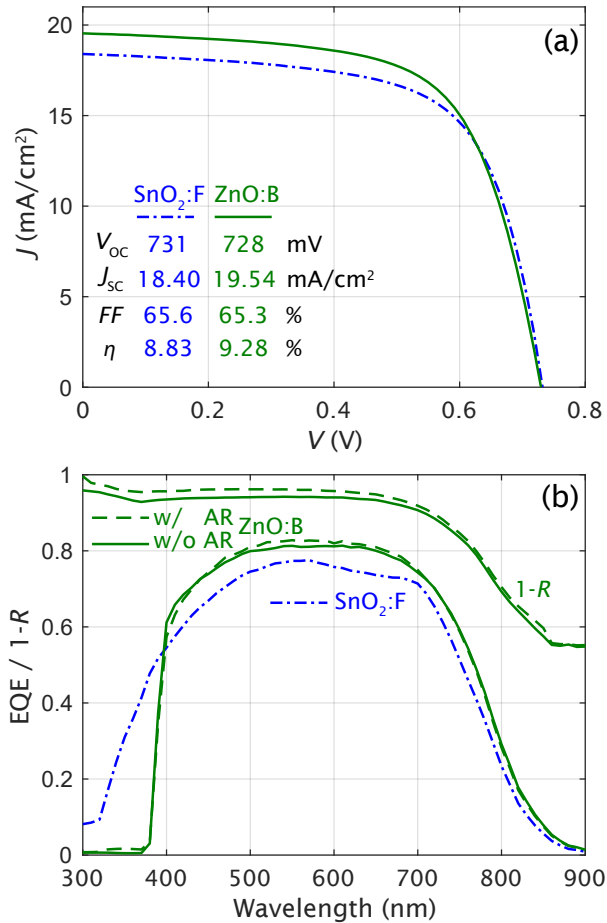


Figure 4.6: (a) Current density-voltage (J - V) curves acquired under AM1.5G illumination, and (b) EQE measured at short-circuit condition, of the optimized a-SiGe_x:H cells fabricated on substrates with different light-scattering capability. Additionally, the EQE and $1-R$ spectra are given for the cells on ZnO:B substrate with and without anti-reflection treatment.

layers delivers a conversion efficiency of 8.8%. For the cells on ZnO:B substrates, the V_{OC} and FF are fairly similar to that on Asahi-VU substrates. An obvious difference appears in the spectral response shown in Figure 4.6(b). Except for wavelengths below 390 nm, at which ZnO:B is very absorptive, the cell made on ZnO:B shows a higher EQE over the whole spectrum of interest. It clearly demonstrates the difference in light scattering from different surface textures. The absorption enhancement leads to an improvement in J_{SC} from 18.4 mA/cm² on Asahi-VU to 19.5 mA/cm² on ZnO:B.

Finally, the optical loss from the reflection at the air/glass interface is tackled. An anti-reflection (AR) foil (produced by temicon GmbH) was applied onto the incident surface of the cell made on ZnO:B substrate, and its influence on the cell reflectance and EQE is shown in Figure 4.6(b). At the wavelength of 550 nm, the reflectance is reduced from 5.8% to 3.9%, which corresponds to a reduction of 33%. The EQE in the visible spectrum is enhanced, consequently. In spite of the parasitic absorption induced by the AR foil in the short wavelengths, an increased J_{SC} of 19.8 mA/cm² is reached. In the end, as a result of the improved light management and optimized device structure, an efficiency of 9.41% is achieved.

4.7 Conclusions

Doped SiO_x:H was implemented in thin-film a-SiGe_x:H solar cells. In the window layer, the bandgap of p-SiO_x:H was adjusted to obtain a high V_{OC} and decent FF , while the transparency of the wide-gap p-layer also resulted in high spectral response in the short-wavelength region. The use of n-SiO_x:H instead of n-a-Si:H reduces the parasitic absorption in the n-layer and suppresses the plasmonic absorption in the neighboring metal layer. A combination of wide-gap n-SiO_x:H and TCO layers with appropriate thicknesses in front of a Ag back reflector provides the most favorable optical properties to enhancing the long-wavelength response of the solar cells. Bandgap grading of n-SiO_x:H was introduced and its application near the i-n interface mitigates the band offset between the wide-gap n-SiO_x:H and the absorber material. As a consequence, thin-film a-SiGe_x:H cells using only SiO_x:H doped layers have been realized without giving up the opto-electrical performance. Having optimized the cell structure, a conversion efficiency of 9.41% in a thin-film a-SiGe_x:H solar cell has been achieved on a ZnO:B-coated substrate with anti-reflection treatment.

5

Quadruple-junction thin-film silicon-based solar cells using four different absorber materials

This chapter was published in *Solar RRL* [169].

Abstract

We fabricated and studied quadruple-junction wide-gap a-Si:H/narrow-gap a-Si:H/a-SiGe_x:H/nc-Si:H thin-film silicon-based solar cells. It is among the first attempts in thin-film photovoltaics to make a two-terminal solar cell with four different absorber materials. Several tunnel recombination junctions were tested, and the n-SiO_x:H/p-SiO_x:H structure was proved a generic solution for the three pairs of neighboring subcells. The proposed combination of absorbers led to more reasonable spectral utilization than the counterpart containing two nc-Si:H subcells. Besides, the use of high-mobility transparent conductive oxide and modulated surface texture significantly enhances the total light absorption in the absorber layers. This work paved the routes toward high-efficiency quadruple-junction cells, and a practical estimation of the achievable efficiency was given.

5.1 Introduction

In the quest for higher power conversion efficiency of photovoltaic (PV) devices, the multi-junction solar cell attracts a great deal of research and development. By properly stacking multiple solar cells, each of which contains an absorber material with a different bandgap, multi-junction solar cells reduce the thermalization losses thus improve the spectral utilization in the power conversion process.

The thin-film silicon-based solar cell has been established as a highly mature PV technology which exhibits excellent control in module manufacturing over a very large area. In the scope of this PV technology, the efficiency improvement by the multi-junction approach has been well demonstrated up to the triple-junction. The record efficiency of stabilized lab cells is 11.8% [79], 12.7% [170] and 14.0% [81] for the single-, double- and triple-junction cells, respectively. The same trend holds for the record initial efficiency [80], [90], which is up to 16.3% for triple-junction cells. To pursue improvements beyond the triple-junction, several labs have made quadruple-junction (4J) thin-film silicon-based solar cells (TFSSCs) with different combinations of absorber materials among hydrogenated amorphous silicon oxide ($a\text{-SiO}_x\text{:H}$), hydrogenated amorphous silicon ($a\text{-Si:H}$), hydrogenated amorphous silicon germanium ($a\text{-SiGe}_x\text{:H}$), and hydrogenated nanocrystalline silicon ($nc\text{-Si:H}$) [98], [127], [128], [171]–[173]. So far, an initial efficiency up to 14.0% has been achieved [128].

Interestingly, most of the reported 4J TFSSCs use the same absorber material which is $nc\text{-Si:H}$ in their third and fourth subcells. A 4J device structure typically consists of $a\text{-Si:H}/a\text{-Si:H}/nc\text{-Si:H}/nc\text{-Si:H}$ absorbers in the four subcells, and the two $a\text{-Si:H}$ absorbers can be made to have different bandgaps. While the use of $nc\text{-Si:H}$ in more than one subcell is a reasonable choice to mitigate the negative influence of light-induced degradation in devices comprising amorphous absorber materials, it does not promote a better spectral utilization which is one of the main motives of making multi-junction solar cells. The spectral response of such 4J cell is exemplified in Fig. 5.1(a). The third and fourth subcells share the same spectral region of effective absorption. The (relatively) high-energy photons absorbed in the third subcell do not result in any additional voltage compared to the low-energy ones absorbed in the bottommost counterpart. In order to fulfill more reasonable spectral utilization in 4J TFSSCs, we propose to replace the third absorber with $a\text{-SiGe}_x\text{:H}$, which has an intermediate bandgap between those of $a\text{-Si:H}$ and $nc\text{-Si:H}$. Such configuration or a similar type has recently been reported at conferences by us and another group [174], [175]. An optical simulation shows in Fig. 5.1(b) that such alteration is effective in reducing the spectral overlap. Quantitatively, the overlap can be assessed with the spectral response by the full width at half maximum (FWHM) of the spectral envelope of the overlapping parts. In Fig. 5.1(a), such FWHM values for three pairs of neighboring subcells are 99/81/284 nm. In comparison, the FWHM values of 102/76/87 nm exhibit a great improvement for the new structure in Fig. 5.1(b).

In this work, we fabricated quadruple-junction thin-film silicon-based solar cells featuring four different absorber materials—wide-gap (W) $a\text{-Si:H}$, narrow-gap (N) $a\text{-Si:H}$, $a\text{-SiGe}_x\text{:H}$ and $nc\text{-Si:H}$. Several structures of tunnel recombination junction (TRJ) were examined to find the effective interconnection between the subcells. Optically, the importance of high-mobility transparent conductive oxide (TCO) was highlighted, and

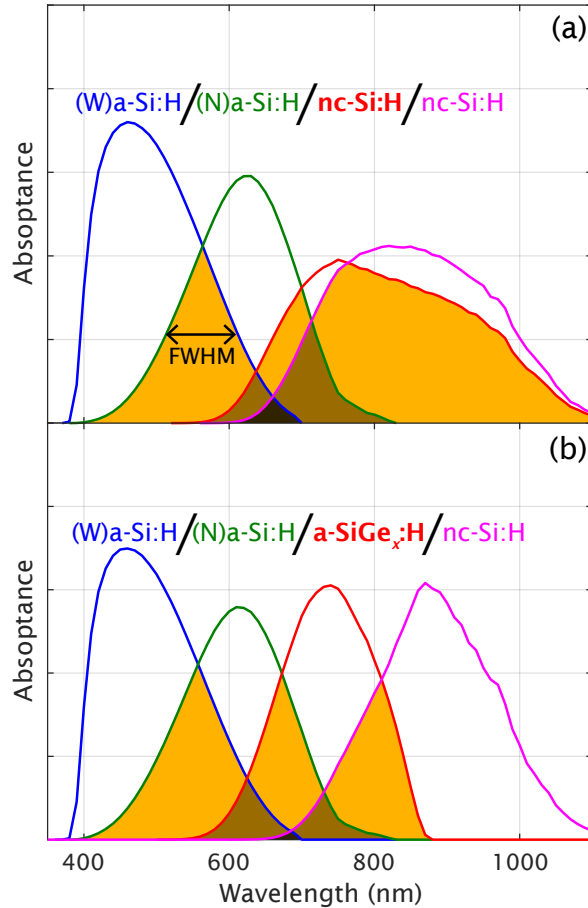


Figure 5.1: Spectral absorptance of the absorber layers, which represents EQE in case of perfect carrier collection, in 4J TFSSCs, given by GenPro4 [107], [176] optical simulations. Current matching was obtained in the simulations by setting the bottommost nc-Si:H of $3.5\ \mu\text{m}$ thick and other absorber thicknesses unconstrained. The shaded areas indicate the overlapping parts of the photoresponse. (W)a-Si:H and (N)a-Si:H represent a-Si:H with wide and narrow bandgaps, respectively.

modulated surface textured (MST) front electrode was applied in 4J cells for enhanced light absorption.

5.2 Experimental

Quadruple-junction (W)a-Si:H/(N)a-Si:H/a-SiGe_x:H/nc-Si:H TFSSCs were fabricated in superstrate configuration. The device structure is depicted in Fig. 5.2. The micro-textured glass substrates were prepared with a chemical etching process which involves a HF/H₂O₂ etchant and a In₂O₃:Sn sacrificial layer [29]. ZnO:Al (AZO) or In₂O₃:H (IOH) was deposited as the front TCO material by radio-frequency magnetron sputtering. In case of the MST substrates, a non-intentionally doped ZnO layer was deposited by low-pressure chemical vapor deposition on micro-textured glass to provide a nanotextured surface [90]. The *p-i-n* junctions of the solar cells were made by plasma-enhanced chemical vapor deposition (PECVD). The optical bandgaps E_{Tauc} of the absorber materials are 1.72, 1.65, 1.42, and 1.12 eV, sequentially. Compared to (N)a-Si:H, the (W)a-Si:H was deposited at a relatively low temperature of 170 °C and the high-pressure regime, and with significant hydrogen dilution [177]. For the intrinsic a-SiGe_x:H, linear bandgap grading was applied near the *p-i* and *i-n* interfaces [147]. All materials were deposited in the reactor at the radio frequency of 13.56 MHz, except the intrinsic nc-Si:H at the very high frequency of 40.68 MHz. Most of the *p*- and *n*-layers were made of mixed-phase hydrogenated silicon oxide (SiO_x:H) [87], [152], [156] doped with boron and phosphorus, respectively. The metal back reflectors were deposited by thermal (Ag) and e-beam (Cr, Al) evaporation, with a shadow mask defining the cell area as 16 mm². The cell isolation was done by removing the materials surrounding the metal pads using anisotropic reactive ion etching. More experimental details regarding the cell fabrication can be found in our previous works [90], [98], [147], [177].

For the external parameters of the solar cells, the open-circuit voltage (V_{OC}) and fill factor (FF) were measured by the illuminated current-voltage (I - V) measurement, while the short-circuit current density (J_{SC}) was determined by the external quantum efficiency (EQE) measurement. In the I - V measurements, a dual-lamp continuous solar simulator (WACOM WXS-90S-L2, class AAA) was used and the samples were controlled at a stage temperature of 25 °C. Two monocrystalline silicon reference cells manufactured by and traceable to the Fraunhofer Institute for Solar Energy Systems (ISE) were used to calibrate the two filtered lamps so that the solar simulator provided optimal spectral matching with the AM1.5G solar spectrum and an incident irradiance of 1000 W/m². The EQE measurements were conducted with an in-house system, in which the light source calibration was done using a silicon photodiode regularly calibrated by Fraunhofer ISE. Bias lights, which were realized by light-emitting diodes (LEDs) with certain emission peaks, were applied such that the subcells not being measured are highly conductive thus pose negligible limitation to the measured current. A bias voltage was applied to offset the subcell being measured to its short-circuit condition. The measurement principle is further described in literature [111], [125].

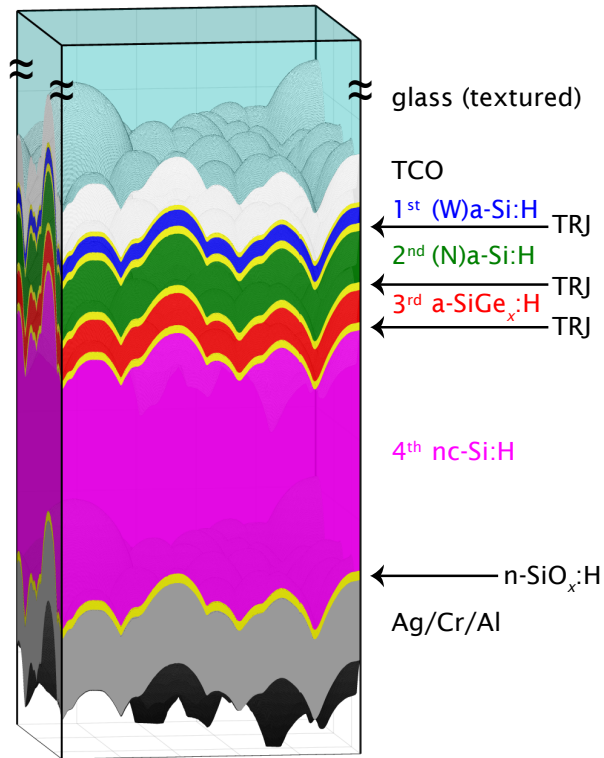


Figure 5.2: An illustration of the proposed device structure for the 4J (W)a-Si:H/(N)a-Si:H/a-SiGe_x:H/nc-Si:H TFSSCs. The light enters from the glass side. In our definition, a TRJ includes all doped layers between the two neighboring absorber layers.

Table 5.1: The V_{OC} losses in dual-junction cells with TRJs formed by different materials. "1st/2nd" means a dual-junction cell comprising the first and second subcells in the 4J cell, which is (W)a-Si:H/(N)a-Si:H, etc.

TRJ materials	ΔV_{OC} (mV)		
	1st/2nd	2nd/3rd	3rd/4th
n-a-Si:H/n-nc-Si:H/p-SiO _x :H	-70	-86	-
n-a-Si:H/n-SiO _x :H/p-SiO _x :H	-34	-63	-
n-SiO _x :H/n-nc-Si:H/p-SiO _x :H	-34	-59	-
n-SiO _x :H/p-SiO _x :H	-32	-67	-45
n ⁺ -SiO _x :H/p-SiO _x :H	-34	-59	-

5.3 Tunnel recombination junctions

In two-terminal multi-junction solar cells, the carriers generated in a subcell should either be collected at one of the electrodes, or recombine with the opposite carriers from the neighboring subcell, in the vicinity of the interface between the two subcells. The recombination process is facilitated by tunnel recombination junctions. To minimize the electrical losses from ineffective recombination, we tested several configurations of TRJ for the three pairs of neighboring subcells in our 4J cell.

Single-junction and dual-junction solar cells were fabricated to resemble the respective parts in the 4J cell. For each pair of neighboring subcells in the 4J cell, TRJs consisting of different material combinations were used in the dual-junction cells while keeping the rest of the structure unchanged. The performance of the TRJs was examined by comparing the V_{OC} of the tandem to the sum of V_{OC} of the two component single-junction cells under AM1.5G illumination. A ΔV_{OC} close to zero is desirable, meaning that the voltages supplied by the subcells can stack up efficiently.

The comparison of the TRJ performance is shown in Table 5.1. Although the use of highly conductive doped nc-Si:H was reported beneficial to forming a good TRJ, its application with a a-Si:H n-layer appears detrimental to the output voltage of the tandem. For the (W)a-Si:H/(N)a-Si:H dual-junction, other tested TRJs involving the use of n-SiO_x:H give similar result, which is a ΔV_{OC} of 32–34 mV. In this comparison, the poor performance of the n-a-Si:H/n-nc-Si:H/p-SiO_x:H TRJ is ascribed to the difference between n-a-Si:H and n-SiO_x:H. The cause is twofold. First, the higher activation energy of 200 meV in n-a-Si:H than that of 80 meV in n-SiO_x:H implies a lower electron concentration and lower recombination rate. Besides, the smaller bandgap of n-a-Si:H means that it is less capable of preventing the holes from passing across the n-layer. Both properties are translated into a worse-performing TRJ. Because of its simplicity and consequently easier control over the optical design, the n-SiO_x:H/p-SiO_x:H TRJ structure is preferred among the tested structures. A similar trend is observed in the (N)a-Si:H/a-SiGe_x:H dual-junction, even though in this case the doping level in n-SiO_x:H needs to be adjusted for the optimal performance. It is probably due to the narrower bandgap of p-SiO_x:H used in the a-SiGe_x:H subcell. Unfortunately, only one TRJ structure was made and tested for the a-SiGe_x:H/nc-Si:H dual-junction. In general, n-SiO_x:H/p-SiO_x:H (with appropriate doping levels) exhibits relatively good

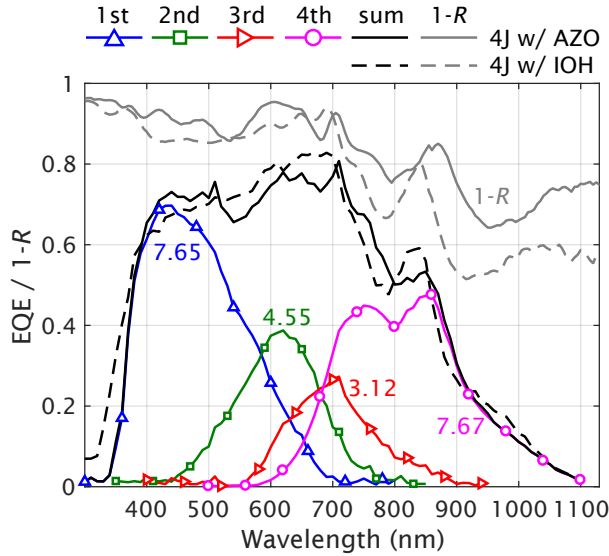


Figure 5.3: Measured EQE and reflectance spectra of 4J solar cells with either AZO or IOH as the front TCO. While the summed EQE and total absorptance ($1 - R$) are shown for both 4J cells, the EQE of individual subcells is only shown for the cell with AZO. The numbers next to the EQE curves indicate the photocurrent density of the subcells in mA/cm^2 .

performance among the TRJs being studied.

Applying the chosen TRJs, 4J solar cells were fabricated on micro-textured glass substrates coated with as-deposited AZO as the front electrode. The thicknesses of the absorber layers are 85/320/190/3500 nm, respectively. The (N)a-Si:H and a-SiGe_x:H were limited to these thicknesses so that the subcells can provide reasonable V_{OC} and FF . The resultant 4J cells exhibit a V_{OC} of 2.789 V and FF of 69.7%. The measured EQE and total absorptance of the device (derived from $1 - R$) are shown in Fig. 5.3. The total photocurrent density is $23.0 \text{ mA}/\text{cm}^2$. In spite of the mismatched photocurrents generated over the four subcells, it is clear that the different bandgaps of the absorbers result in different ending edges of the spectral response of the subcells. The FWHM of the spectral overlap between the third and fourth subcells is 115 nm, a clear improvement from a value of 251 nm for the 4J a-SiO_x:H/(N)a-Si:H/nc-Si:H/nc-Si:H cell reported in our previous work [98].

5.4 Front TCO

The parasitic absorption in the front TCO layer contributes a significant part to the optical losses in solar cells when the absorber is capable of utilizing the near-infrared light. Therefore, a TCO material with a high carrier mobility is preferred for high-efficiency solar cells because the adequate conductance can be achieved with less

free-carrier absorption.

Two 4J solar cells using different TCOs as the front electrode and with the rest of the structure identical are compared. The one reported in the previous section uses an AZO layer with a thickness of $1\ \mu\text{m}$. Another one is with 180 nm of IOH. IOH as a TCO material is well known for its high carrier mobility [96], [97]. The IOH produced in our lab has a carrier mobility close to $160\ \text{cm}^2/(\text{Vs})$ and a carrier concentration around $1.3 \times 10^{20}/\text{cm}^3$, in contrast to a mobility less than $25\ \text{cm}^2/(\text{Vs})$ and concentration more than $4 \times 10^{20}/\text{cm}^3$ in AZO. The two TCO layers used in our solar cells exhibit similar sheet resistance in the range of $15\text{--}20\ \Omega/\square$. Figure 5.3 shows the spectral response of the two 4J cells. On the one hand, the EQE of the cell with IOH shows marginal enhancement in the long wavelengths. It is due to the limited light-scattering capability of the particular substrates, which contain rather large and smooth micro-texture. Quantitatively, the photocurrent density J_{ph} of the fourth subcell is increased from 7.67 to $7.97\ \text{mA}/\text{cm}^2$. On the other hand, the more transparent TCO allows more infrared photons to enter the solar cell, as it is evidenced by the total absorptance spectra $(1-R)$. The 4J cell with IOH, as a whole, absorbs less light in the long wavelengths. Between 700 and 1100 nm, the difference in absorptance is equivalent to a photocurrent of $2.54\ \text{mA}/\text{cm}^2$ under AM1.5G spectrum, and can be ascribed to the additional absorption in AZO. Therefore, by using a high-mobility TCO such as IOH, a greater photocurrent supplied by the infrared light is enabled.

5.5 Enhanced light scattering by MST

Effective light scattering always plays an indispensable role in high-efficiency TFSSCs owing to the limited thickness and the low absorption coefficient in near-infrared of the absorbers. With respect to multi-junction cells, the light management is even more demanding as the photogeneration should be evenly distributed among the subcells and absorption enhancement is needed throughout the whole spectrum between 350 and 1100 nm. It can be seen that the output current of the 4J cells shown in Fig. 5.3 is severely limited by the a-Si:H and a-SiGe_x:H subcells. Since there is not much room to further increase the thickness of these absorbers without sacrificing the carrier transportation, enhanced light scattering is crucial for boosting the performance of such devices.

Modulated surface texture has been proven a powerful means for enhancing the light absorption throughout a broad spectrum in both thin-film and wafer-based silicon PV technology [29], [38], [90]–[95]. Therefore, we implemented MST substrates in 4J solar cells so as to improve the light scattering. The MST substrate used in this work is the same type as the one reported in our previous work [90]. It comprises, from the surface of light incidence, a micro-textured glass for scattering the low-energy photons, an IOH layer acting as a highly-transparent electrode, and $1\ \mu\text{m}$ of non-intentionally doped ZnO with native nano-texture which facilitates scattering of the short wavelengths and light in-coupling. The micro-texture in the MST has smaller and steeper features than the micro-texture used in the preceding sections so it should help scatter the light more effectively [93]. The structure of the 4J cell deposited on the MST substrate is the same as before, except the thickness of (W)a-Si:H was

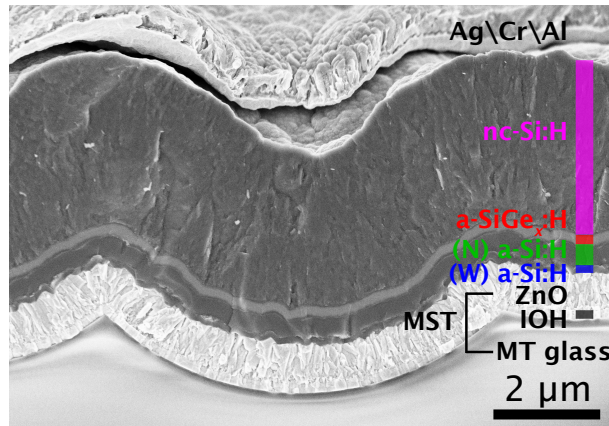


Figure 5.4: Scanning electron microscope image of the 4J cell fabricated on the MST substrate. The materials and their thicknesses are graphically indicated.

slightly reduced to 80 nm to redirect some excess photocurrent to the second subcell. The completed device is presented via scanning electron microscope in Fig. 5.4. In the image, the deposited layers can be clearly distinguished from each other except for the doped layers which are too thin to be identified. It should also be noted that the rough surface of ZnO is smoothed out after the deposition of the second and third subcells, leaving a favorable surface for depositing high-quality nc-Si:H [29], [90].

The spectral response of the 4J cell on MST substrate and of other reference cells is given in Fig. 5.5(a). In relation to the 4J cell on micro-textured substrate with IOH, the MST considerably enhances the light absorption in the 4J cell. As a result of the improved light in-coupling and scattering, the total J_{ph} provided by the three upper subcells increased by 0.91 mA/cm^2 , while J_{ph} of the bottommost subcell increased by 1.11 mA/cm^2 , leading to a total J_{ph} of 25.3 mA/cm^2 and an overall improvement of 2.02 mA/cm^2 . The enhancement in spectral response is noticeable over most part of the relevant spectrum, which is expected from the advanced design of the MST substrate.

Electrically, the demonstrated 4J cell on MST substrate exhibited an average V_{OC} and FF of 2.769 V and 71.9%, respectively. The $J-V$ curve is given in Fig. 5.5(b). The reduced V_{OC} compared to that on micro-texture is probably caused by the influence of the rougher surface texture on the thin (W)a-Si:H subcell. Further optimization on material deposition and TRJ design is required to close the gap between the obtained voltage and the ideal one.

5.6 Potential improvements

Despite the added photocurrent, the J_{SC} of the 4J cell was still limited by the a-SiGe_x:H subcell. The first practical solution to tackle the current mismatch is to redistribute the photocurrents among the first, second and third subcells. By reducing

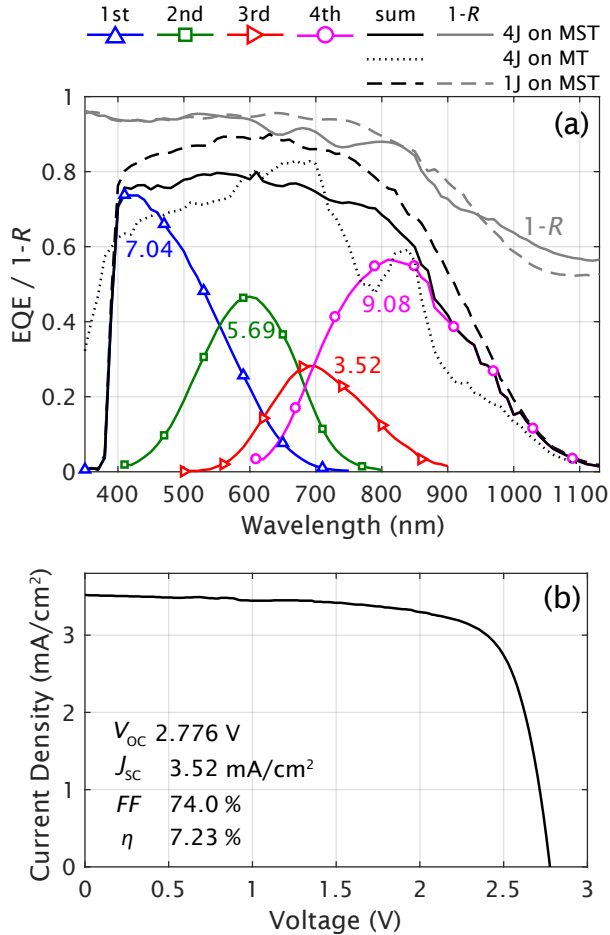


Figure 5.5: (a) Measured EQE and reflectance spectra of the 4J cell on MST substrate. For comparison, the relevant spectra of a single-junction nc-Si:H cell on MST substrate and the 4J cell on micro-textured (MT) substrate with IOH are also plotted. The EQE of the single-junction cell was measured with a negative bias voltage of $-3V$ to emphasize the optical absorption. (b) J - V curve of the best 4J cell on MST substrate. The external parameters indicated in the graph are of the best cell, while the average parameters are reported in the text.

the thicknesses of (W)a-Si:H and (N)a-Si:H absorbers, a J_{ph} of 5.42 mA/cm^2 in each of these subcells can be approached. Considering the excess photocurrent in the fourth subcell, a thicker n-SiO_x:H layer could have been made between the third and fourth subcells to raise the intermediate reflection and thus make the photocurrent better distributed [84], [93], [103]. Optical simulations with GenPro4 [107], [176] were performed to examine the effect of intermediate reflectors. By using an n-SiO_x:H n-layer in the a-SiGe_x:H subcell with a slightly lower refractive index (1.95 instead of 2.10) and a thickness of 100 nm in contrast to the original 30 nm, the J_{ph} of the second and third subcells in total can be increased by 1.24 mA/cm^2 . It can lead to a J_{ph} of 5.83 mA/cm^2 in each of the three upper subcells. However, the aim of this presented 4J cell was to explore the photocurrent achievable in 4J cells on the MST substrate. An intermediate reflector would lower the total J_{ph} and that of the fourth subcell, so it was not intentionally deployed in this fabricated cell.

To give an outlook on the potential improvement based on this device structure, a single-junction solar cell was fabricated on the MST substrate with the same nc-Si:H absorber thickness of $3.5 \mu\text{m}$. The EQE measured at a bias voltage of -3 V is plotted in Fig. 5.5(a) to demonstrate the optical potential of this MST substrate. The equivalent J_{ph} is 28.9 mA/cm^2 in the single-junction, and the possible absorption in 4J cells should be even greater considering the larger total thickness of the absorber layers. The difference in EQE between the single-junction and 4J (summed) is ascribed to the extra parasitic absorption in the doped layers, the light escaping the cell from intermediate reflection, and the imperfect carrier collection in the thick amorphous subcells. Should these issues be engineered, a total J_{ph} over 28 mA/cm^2 in a 4J cell on MST substrate would be feasible. If we take into account the fact that the performance of a-SiGe_x:H deteriorates with increased absorber thickness, this restriction reduces the possible J_{SC} to an approximate 6.5 mA/cm^2 , revealed by another optical simulation using 250 nm a-SiGe_x:H (E_{Tauc} 1.41 eV) absorber and intermediate reflector in the third subcell.

Based on the materials and fabrication processes currently available in our lab, we suggest that a well-optimized 4J cell with this structure will exhibit V_{OC} of 3.0 V, J_{SC} of 6.5 mA/cm^2 , FF higher than 72 %, and an initial efficiency of 14.0 %. The high V_{OC} was estimated with considerations of the V_{OC} of the corresponding single-junction cells and minor voltage losses at the TRJs. To go further, with state-of-the-art a-SiGe_x:H subcell fabrication and process optimization which have been demonstrate in literature [80], [178], we suggest that optimized external parameters with V_{OC} of 3.05 V, J_{SC} of 6.5 mA/cm^2 , FF of 77 %, and an initial efficiency of 15.3 % are practically achievable.

5.7 Conclusions

Quadruple-junction (W)a-Si:H/(N)a-Si:H/a-SiGe_x:H/nc-Si:H thin-film silicon-based solar cells have been realized experimentally. By introducing a a-SiGe_x:H subcell, the spectral utilization in 4J cells was improved and the spectral overlap between the subcells was mitigated. Several tunnel recombination junctions were examined and it was found that a simple n-SiO_x:H/p-SiO_x:H structure delivered a satisfactory outcome for all pairs of neighboring subcells. The use of high-mobility In₂O₃:H instead of ZnO:Al at

the front electrode allowed more infrared photons to enter and be utilized by the bottom subcells. Further improvement in light management was achieved by modulated surface textured substrates made of highly-transparent TCOs. Its light-scattering and anti-reflection effects significantly increased the photocurrent in the 4J cells. Based upon all exploration done in this work as well as state-of-the-art technology reported in literature, an initial efficiency of 15.3% should be achievable with the proposed structure provided certain optimization is taken.

6

Too many junctions? — a case study of multi-junction thin-film silicon-based solar cells

This chapter was published in *Advanced Sustainable Systems* [179].

Abstract

The benefit of two-terminal multi-junction solar cells in regard to the number of junctions (subcells) is critically evaluated. The optical and electrical losses inherent in the construction of multi-junction cells are analyzed using information from thin-film silicon photovoltaics as a representative case. Although the multi-junction approach generally reduces the thermalization and non-absorption losses, several types of losses rise with the number of subcells. Optical reflection and parasitic absorption are slightly increased by adding supporting layers and interfaces. The output voltages decline because of the tunnel recombination junctions, and more importantly of the illumination filtered and reduced by the top subcell(s). The loss mechanisms consume the potential gains in efficiency of multi-junction cells. For thin-film silicon, the triple-junction is confirmed to be the best performing structure. More generally, only when each component subcell shows a high ratio between the output voltage and the bandgap of the absorber material, a multi-junction cell with a large number of subcells can be beneficial. Lastly, the high voltage and low current density of multi-junction cells with a large number of subcells make them difficult to optimize and manufacture, vulnerable to any changes in the solar spectrum, and thus less practical for the ordinary terrestrial applications.

6.1 Introduction

The theoretical limit for the power conversion efficiency of photovoltaic cells is 33.1% [73] in the case of a single p - n junction under unconcentrated sunlight—widely known as the Shockley-Queisser limit [72]. Such efficiency can be surpassed by loosing some of the restrictions which define the limit. Firstly, when the incident irradiance is increased by a concentrator, the ratio of photocurrent to dark current of the solar cell is increased, leading to higher open-circuit voltage (V_{OC}) and fill factor (FF). Secondly, by stacking up multiple p - n or p - i - n junctions (each of which is referred to a subcell) using absorber materials with different energy bandgaps, multi-junction solar cells can reduce the thermalization and non-absorption losses, meaning less spectral mismatch and a better spectral utilization. The theoretical efficiency limit of the solar cell comprising infinite number of component subcells is 68.2% without concentration and 86.8% with concentration [99]. In practice, the III-V photovoltaic technology represents a very successful demonstration of both strategies [180], [181]. Within this category, the benefit of multi-junction concept is apparent as the record efficiency of concentrator photovoltaic cells is 29.3% for the single-junction, and grows to 34.2%, 44.4%, and 46.0% for the monolithic two-terminal double-, triple-, and quadruple-junction cells, respectively [182]–[185].

Multi-junction solar cells can be made with two or more external electrical contacts (terminals). The components in a monolithic two-terminal device are considered to be in series connection. Therefore, the output current of a two-terminal device is constrained by the component which supplies the least photocurrent. Despite the limitation, two-terminal multi-junction cells are much more feasible to design and manufacture than the ones with more terminals, thus more practical for applications. This type of two-terminal devices is the subject of this paper. For simplicity, we refer two-terminal multi-junction solar cells to as multi-junction solar cells, without further specification.

While the multi-junction III-V solar cells mark the highest achieved power conversion efficiency of photovoltaic cells to date, the multi-junction concept has been explored and developed in many other photovoltaic technologies as well. Besides the reduction of losses originating from spectral mismatch, the multi-junction concept offers some additional benefits to the thin-film photovoltaics. The effective absorption is split into a few separate layers in different subcells, meaning that each layer can be made thinner for the same total absorption. Such thickness reduction improves the electrical performance when the carrier transportation in the material is a limiting factor. Moreover, the division of photocurrent implies less resistive losses over the electrical interconnections. The thin-film silicon-based solar cell (TFSSC) has a long history of developing multi-junction solutions to make use of these advantages. The efficiency improvement by additional subcells has been shown up to the triple-junction configuration [79]–[81], [90], [151], [170], [186], [187]. In organic photovoltaics, the absorber materials have rather narrow absorption spectra. Tandem (double-junction) devices with different materials can help to cover a broader part of the solar spectrum, thus have become the subject of active researches for over two decades [188]–[190]. In general, the multi-junction concept attracts more research efforts whenever a photovoltaic technology becomes relatively mature and approaches its practical per-

formance limit of the single-junction. Moreover, hybrid tandem solar cells integrating different photovoltaic technologies have drawn more and more attention over the past years in the pursuit of higher efficiencies. To name a few notable examples, the perovskite/crystalline silicon tandem [129]–[131], [191], perovskite/CIGS tandem [132] and hydrogenated amorphous silicon (a-Si:H)/organic double- and triple-junction solar cells [134] have all demonstrated the potential of exceeding the efficiency of the component single-junction cells. When the absolute efficiency is the main concern, making multi-junction solar cells is the inevitable trend.

How many junctions (subcells) are too many? Ideally, the more subcells are properly integrated in a device, the better performance the device can provide. The gain from putting on one more additional subcell, however, becomes less with the increased number of subcells. Practically, there is a certain point that $N+1$ -junction cells can unlikely outperform N -junction cells in spite of the best engineering efforts. The efficiency improvement has not been achieved beyond the 5-junction configuration in case of the highly-mature and extensively-optimized III-V photovoltaics [112], [184], [185]. While the restriction of developing III-V solar cells with more subcells largely lies in the search of material systems with suitable bandgaps and achievable by compatible fabrication techniques, there are other limiting mechanisms which can play a bigger role in different multi-junction photovoltaic technologies. Optical and electrical losses can occur in the sophisticated device structures, beside the impact of filtered sunlight on the opto-electrical response of the subcells. In these respects, the thin-film silicon-based photovoltaics is very interesting for studying the multi-junction concept. The lesser transport properties of electrical carriers and the weak absorption coefficient near the band edge of the materials pose great challenges to the design and optimization of the device structures. Up to now, the highest initial efficiencies of TFSSCs reported in literature are 11.8% [79], 14.8% [90], 16.3% [80], and 15.0% [192] for the single-, double-, triple-, and quadruple-junction configurations, respectively. Remarkably, multi-junction TFSSCs have achieved high efficiencies with some very complicated structures. On the other hand, it is still under question whether the record held by the triple-junction can eventually be broken by a structure comprising even more subcells.

In this work, we evaluate the effects of the increased number of subcells on the performance of multi-junction solar cells. By carefully examining the optical and opto-electrical losses which originate from the multi-junction approach, the realistic benefit of making multi-junction cells is studied.

6.2 Device structures and outline

Five different structures of multi-junction TFSSCs with up to four subcells were studied. In the order of decreasing bandgap, the absorber materials include (W)a-Si:H (wide-gap hydrogenated amorphous silicon), (N)a-Si:H (narrow-gap a-Si:H), a-SiGe_x:H (hydrogenated amorphous silicon germanium), and nc-Si:H (hydrogenated nanocrystalline silicon), providing a great variety of materials with different spectral sensitivity. The cell structures, identified by the absorber materials, are shown in Table 6.1. They are the single-junction nc-Si:H cell (S), the conventional double-junction a-Si:H/nc-Si:H cell (D), the triple-junction cell with nc-Si:H (TS) or a-SiGe_x:H (TG) in the middle

Subcell	1 st	2 nd	3 rd	4 th
S	nc-Si:H	—	—	—
D	(N)a-Si:H	nc-Si:H	—	—
TS	(W)a-Si:H	nc-Si:H	nc-Si:H	—
TG	(W)a-Si:H	a-SiGe _x :H	nc-Si:H	—
QS	(W)a-Si:H	(N)a-Si:H	nc-Si:H	nc-Si:H
QG	(W)a-Si:H	(N)a-Si:H	a-SiGe _x :H	nc-Si:H

Table 6.1: Material configurations of the studied single- and multi-junction solar cells. The structures are the single-junction (S), double-junction (D), triple-junction with either nc-Si:H (TS) or a-SiGe_x:H (TG), and quadruple-junction with either nc-Si:H (QS) or a-SiGe_x:H (QG). (W)a-Si:H and (N)a-Si:H are the wide-gap and narrow-gap a-Si:H, respectively.

subcell, and the quadruple-junction cell with nc-Si:H (QS) or a-SiGe_x:H (QG) in the third subcell. These structures are chosen for comparison because of their reported use in literature [80], [81], [98], [169] and the different arrangements of the absorber bandgap. This is not an exhaustive list of all reported multi-junction configurations [98], [127], [192], but sufficiently representative for the purpose of this study. Configuration D, TG, and QG provide descending bandgaps of absorber materials along the direction of light incidence, therefore they should offer reasonable spectral utilization, fulfilling the goal of the multi-junction concept. On the other hand, configuration TS and QS were widely used in literature because the emphasized use of nc-Si:H mitigates the light-induced degradation of the whole device.

The different multi-junction structures are compared by their photovoltaic performance. First of all, Section 6.3 derives the potential efficiencies of the studied solar cells from the properties of high-quality single-junction cells and a set of optimistic assumptions. Starting from this baseline, several loss mechanisms are investigated in the following sections to approach a more realistic estimation of the efficiencies. Section 6.4 uses optical modeling to inspect the spectral response of the structures and study how the number of subcells influences the absorption and reflection of the solar cells. The way how a multi-junction cell is formed determines its output voltage. Concerning the voltages, the effect of tunnel recombination junctions (TRJs) is discussed in Section 6.5 while the effect of different irradiance experienced by each subcell is discussed in Section 6.6. Material properties define what device structures are feasible, and Section 6.7 shows how the restriction on absorber thickness change the attainable efficiencies. Section 6.8 comments on what should be considered in the pursuit of higher efficiencies by multi-junction solar cells. Last but not least, the impact of current matching/mismatch on the performance of multi-junction solar cells, especially how the cells with different numbers of subcells react to the variation in solar spectrum, is examined in Section 6.9.

	$V_{OC-1sun}$ (V)	$J_{SC-1sun}$ (mA/cm ²)	Ref.
(W)a-Si:H	1.024	9.73	[80]
(N)a-Si:H	0.901	16.55	[193]
a-SiGe _x :H	0.764	18.87	[80]
nc-Si:H	0.552	25.60	[90]

Table 6.2: V_{OC} and J_{SC} of single-junction solar cells under AM1.5G (1sun) illumination.

	S	D	TS	TG	QS	QG
V_{OC} (V)	0.552	1.453	2.128	2.340	3.029	3.241
J_{SC} (mA/cm ²)	32.9 [113]	16.45	10.97	10.97	8.23	8.23
FF (%)			77.0 [80]			
η (%)	13.98	18.40	17.97	19.76	19.18	20.52

Table 6.3: External parameters of TFSSCs estimated by optimistic assumptions.

6.3 Lossless estimation

To start the comparison, the efficiency potential of these structures is estimated by neglecting many sources of power losses. Several optimistic assumptions are used for this estimation. Firstly, the V_{OC} of the multi-junction cell is the simple arithmetic sum of the V_{OC} of the component single-junction cells, which were individually made and measured under AM1.5G solar spectrum. No additional voltage losses are present in the formation of the multi-junction. The external parameters of some best single-junction cells reported in literature are shown in Table 6.2, and their V_{OC} is used in the estimation. Secondly, the photocurrent is perfectly divided among the component subcells, and the total photocurrent density is 32.9 mA/cm², the highest reported short-circuit current density (J_{SC}) for single-junction nc-Si:H solar cells [113]. This assumption represents the optimal light trapping and current matching, as well as the minimal optical losses. Thirdly, the FF is fixed at a high value of 77% which might be realized by exceptional device optimization [80]. Following these assumptions, the external parameters of the studied structures are derived and shown in Table 6.3.

Based on the parameters reported in literature and with some optimistic assumptions, the performance shown in Table 6.3 serves as the upper limit of these structures where most optical and electrical losses related to multi-junction cells are neglected. In such optimistic scenario, the implied efficiency (η) highly depends on the choice of materials. The use of the same material (nc-Si:H) in two subcells results in the lower efficiencies of structure TS and QS, compared to their counterparts in which all absorber materials are different. The triple-junction structure TS even performs worse than the double-junction structure D in this calculation. As expected, efficiency improvements are suggested between structures S, D, TG, and QG when the number of subcells increases and different absorber materials with proper bandgaps are used.

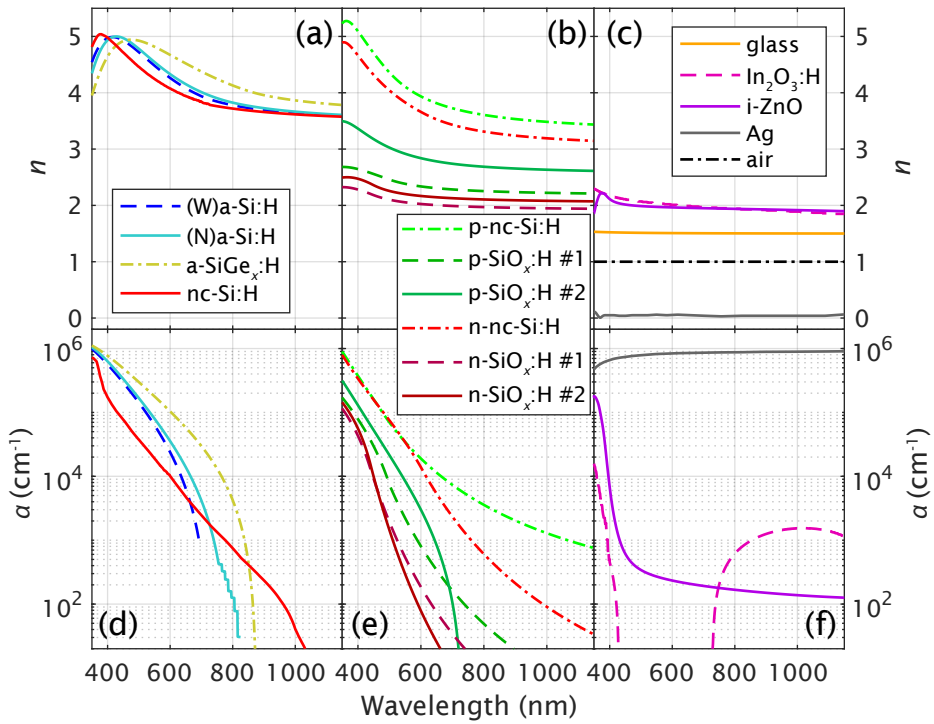


Figure 6.1: The wavelength-dependent refractive index (n) and absorption coefficient (α) of the (a,d) absorber materials, (b,e) doped materials, and (c,f) other supporting materials, used in the studied multi-junction solar cells.

6.4 Optical analysis

When the number of subcells increases, the increase in the total absorber thickness can possibly enhance the effective absorption of the device. Nevertheless, the parasitic absorption and reflection may also increase because of the additional supporting layers and interfaces, leading to extra optical losses (Here supporting layers include all layers which are not an absorber layer). The quantitative examination of the absorptance and reflectance is desired for studying the effects of multi-junction structures on the optical response of the devices. Optical modeling and simulations provide a powerful tool to reveal such internal quantities which can hardly be accessed by measurements.

The model GenPro4 [107], which is suitable to concurrently model different optical regimes from refraction to diffraction, was used to simulate the optical response in the studied structures. The information of the layers and scattering interfaces define the structure in the optical model. The refractive index and absorption coefficient (or extinction coefficient) of the materials were either measured internally by spectroscopic ellipsometry or adopted from literature. Such optical constants of all materials used in the studied structures are shown in Figure 6.1. In respect of the light scattering, the modulated surface texture (MST) was proved an effective light scatterer and in-

Material	Thickness (nm)
air	infinite
glass	7×10^5
In ₂ O ₃ :H	140
ZnO	1000
p-nc-Si:H	4
p-SiO _x :H #1	8
(W)a-Si:H	t_1
n-SiO _x :H #1	30
p-SiO _x :H #1	8
(N)a-Si:H	t_2
n-SiO _x :H #1	30
p-SiO _x :H #2	16
a-SiGe _x :H	t_3
n-SiO _x :H #2	30
p-SiO _x :H #2	12
nc-Si:H	t_4
n-SiO _x :H #2	60
Ag	infinite

Table 6.4: The simulated structure of QG. p-SiO_x:H #1 and n-SiO_x:H #1 are with higher oxygen content, larger bandgap and lower refractive index, compared to p-SiO_x:H #2 and n-SiO_x:H #2. In spite of its absorptive nature, the thin p-nc-Si:H layer was used in the device to mitigate the transport barrier between the TCO and the p-layer [195]. The thickness of nc-Si:H absorber, t_4 , was fixed at 3500 nm in the simulation.

coupler in a broad spectral range [90], [92], [93]. Together with highly transparent supporting layers and a silver back reflector, the MST was applied in the simulations of all studied structures to examine the optical performance within state-of-the-art light trapping scheme [106]. In the model, the MST was realized by assigning a refractive scattering interface between the micro-textured glass and the TCO, and a diffractive scattering interface on top of non-intentionally-doped ZnO [194]—mimicking how the MST is fabricated experimentally [90]. The thicknesses of the doped layers and other supporting layers were fixed in the simulated structures at the typical values used in actual devices. To enable a relevant comparison between the studied structures, the thicknesses of the absorber layers were optimized per case. In all structures, the thickness of absorber layer in the bottommost subcell, which is nc-Si:H, was predetermined at 3500 nm. Such thickness suggests a relatively thick nc-Si:H layer for the absorption of near-infrared light while being able to support a decent carrier transportation. The thicknesses of other absorber layers were iteratively adjusted in the model until the current-matched condition, that the implied photocurrent densities (J_{ph}) of all absorber layers within a structure are equal, is fulfilled. This matched J_{ph} can be approximated as the J_{SC} of the multi-junction cell. As an extensive example, the information used in the simulation of structure QG is given in Table 6.4.

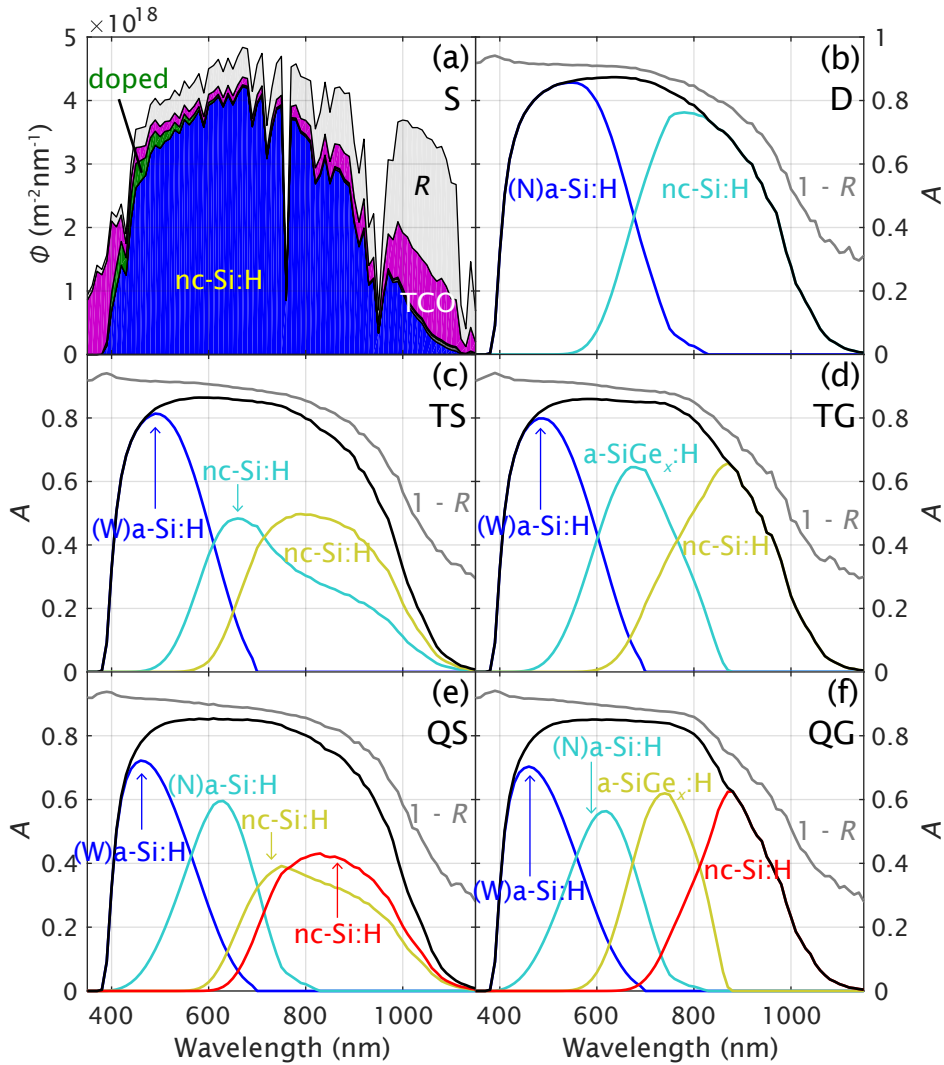


Figure 6.2: Simulated optical response of the studied structures. (a) The absorbed and reflected photon flux density of structure S, with respect to AM1.5G illumination. (b-f) The effective absorptance and $1 - R$ in structure (b) D, (c) TS, (d) TG, (e) QS, and (f) QG. The solid black lines show the sum of effective absorptance from all absorber layers.

The simulated optical response of the studied structures is shown in Figure 6.2. The simulation calculates the spectral absorptance of each layer and the total reflectance of a given structure. Figure 6.2(a) demonstrates the absorption in each layer of the single-junction structure S with respect to the photon flux density of AM1.5G illumination. For better clarity, Figure 6.2(b-f) only plot the absorptance of the absorber layers in the multi-junction structures, together with the respective total absorption derived from $1 - R$, where R is the total reflectance. In structures TG and QG, there is less spectral overlap between the two bottom subcells than there is in structures TS and QS. This suggests a better spectral utilization by the absorber configurations in TG and QG.

6.4.1 Spectral overlap

A spectral overlap between the absorption spectra of two subcells means that photons with a wavelength within the overlapping region can generate carriers in more than one subcell. When the absorber materials of the spectrally overlapping subcells have different bandgaps, some of the high-energy photons which can potentially be used by the wide-gap material are absorbed and converted in the narrow-gap material, leading to a lower generated voltage and more thermalization losses. While the spectral overlap cannot be eliminated due to the absorption properties of the materials, some unnecessary losses caused by the design of device structure should be avoided. For example, in the case of structure QS or QG, the topmost absorber layer is made too thin that it does not fully utilize the effective spectrum of the material so some of the high-energy photons are absorbed in the subsequent subcells. The insufficiently thick absorber layers therefore induce extra thermalization losses. Such designs are less ideal and should be avoided. Furthermore, the concern of spectral overlap suggests that in a multi-junction solar cell, the use of absorber materials with indirect bandgap and lesser absorption capability should be limited. These materials, such as nc-Si:H or nc-SiGe_x:H, should only be used in one subcell at most. When used, it should be placed only in the bottommost subcell. Otherwise, the use of these materials in two or more subcells, or in a non-bottommost subcell, will lead to significant spectral overlap and thermalization losses.

6.4.2 Parasitic absorption

The absorption in the supporting layers including the transparent conductive oxide (TCO) and the doped layers does not result in collectable photocurrent in the external circuit, thus is regarded as parasitic absorption and a major cause of optical losses. Intuitively, one may expect more parasitic absorption in the structure with more subcells taking the extra intermediate layers into account. This speculation was examined using the data available from the optical simulations.

Figure 6.3 shows the absorption in different layers in the form of equivalent J_{ph} under AM1.5G spectrum. The J_{ph} was calculated by Equation 6.1:

$$J_{ph} = e \int_{300 \text{ nm}}^{1200 \text{ nm}} A(\lambda) \cdot \Phi(\lambda) d\lambda \quad (6.1)$$

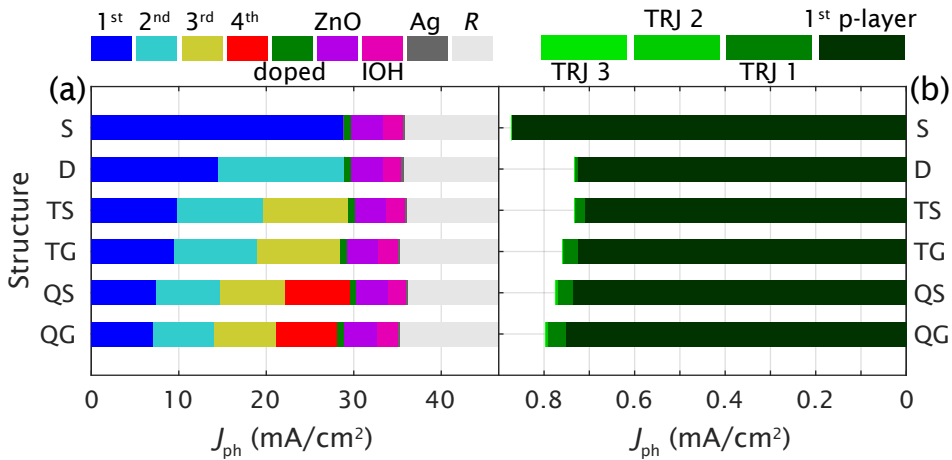


Figure 6.3: (a) The absorption in different layers and the total reflection of the studied structures, equivalent to photocurrent density J_{ph} under AM1.5G spectrum. IOH stands for $\text{In}_2\text{O}_3:\text{H}$, the use of which is indicated in Table 6.4. (b) The parasitic absorption in the doped layers. TRJ 1 is the TRJ between the first and second subcells, etc.

where e is the elementary charge, $A(\lambda)$ is the wavelength-dependent absorptance of a layer or the total reflectance, $\Phi(\lambda)$ is the spectral photon flux density of AM1.5G spectrum. In Figure 6.3(a), all absorption and reflection in a structure are included, so the sum is always 46.48 mA/cm^2 , which accounts for the photons available in the wavelength range from 300 nm to 1200 nm. The parasitic absorption in the TCO layers is comparable throughout the studied structures. Interestingly, the total effective absorption increases in the order of S, D, TS, to QS, but decreases in the order of D, TG, to QG. The parasitic absorption in the doped layers is individually presented in Figure 6.3(b). The bars in the darkest green indicate the contribution of the p-layers in the topmost subcells. Then, the bars in lighter green represent the absorption in the subsequent doped layers which also act as the TRJ. Noticeably, the parasitic absorption in the doped layers is dominated by the p-layer of the topmost subcell, where the majority of visible light is absorbed. The subsequent doped layers are mostly transparent to the residual photons which have lower energy. The absorption in the subsequent doped layers becomes apparent with the increased number of subcells, as the absorption spectra of the topmost subcells become narrower and more reddish photons can arrive at the subsequent layers. Especially, to match the photocurrent in the quadruple-junction structures, the topmost absorber should only utilize the bluest part of the spectrum, making the leftover susceptible to parasitic absorption. Quantitatively speaking, the transparency of the doped materials plays a bigger role than the device structure. A less transparent p-layer used in structure S is responsible for the considerably larger parasitic absorption. Even in the subsequent layers, an insertion of a less transparent 4-nm n-type nc-Si:H layer between the first and second subcells of the structure QG can increase the parasitic absorption by 0.088 mA/cm^2

equivalent, which is a relative increase of 11.1%. To sum up, in the consideration of parasitic absorption, device structures with less subcells are favorable, on the basis of using highly transparent supporting materials.

6.4.3 Reflection losses

Reflection occurs when light impinges upon an interface between two media. In solar cells, beside the primary reflection at the surface which directly decides the amount of photons entering the cell, the intermediate reflection between the interfaces inside the cell can also influence the optical response, both positively and negatively. With the information extracted from the simulations, Figure 6.4(a) illustrates how the reflection develops along the structure of solar cell QG and results in the total reflectance measurable from the surface. The x-axis shows the depth (not in scale) related to the cell structure and the materials are indicated. The profile drawn in a solid line sketches the change of refractive index n of the materials along the depth. The overlaying stem plot shows the accumulated reflection up to a certain interface, in the form of equivalent photocurrent (J_R) under AM1.5G spectrum. The primary reflection at air/glass interface is worth 1.90 mA/cm² as indicated. Before the light enters the topmost (1st) subcell, the refractive index increases stepwise from that of the air to the first absorber. The small steps in n offer an anti-reflection effect, but the abrupt increase in n at the first subcell still causes noticeable intermediate reflection. The highly transparent doped hydrogenated silicon oxide (SiO_x:H) materials have relatively large bandgap and low refractive index. The contrast in n between the absorber and doped materials is depicted by the profile, which raises the accumulated reflection whenever a subsequent subcell is encountered. In the end, the remaining photons which are not absorbed are reflected back by the metal (Ag) reflector.

The intermediate reflection occurring at the subsequent subcells can be a source of optical losses. In Figure 6.4(b), the spectral photon flux density of the reflection supplemented by different interfaces in structure QG, with response to AM1.5G incident spectrum, are stacked to show how each interface builds up the accumulated reflection. It should be pointed out that the intermediate reflection at the subsequent subcells is mostly constituted of low-energy photons, which can be utilized by the bottom subcells but not the top ones. To clarify this behavior, it can be seen in Figure 6.4(b) that the intermediate reflection from the 1st, 2nd, 3rd and 4th subcell starts from the wavelength around 400, 500, 650 and 750 nm, respectively. These reflected photons then escape the solar cell and are lost.

The different components of the accumulated reflection from the studied structures are compared in Figure 6.4(c). It is clear that the more subcells there are in a structure, the more intermediate reflection occurs and the less infrared light can arrive at the bottommost absorber layer. It explains the observation in Figure 6.3(a) that the effective absorption decreases with the increased number of subcells in the group in which a-SiGe_x:H is used (D > TG > QG). In the group of S, D, TS and QS, the impact of reflection losses is offset by the absorption of the thick nc-Si:H layer in the penultimate subcell of structures TS and QS.

Having considered the effects of parasitic absorption and intermediate reflection, it is suggested from the optical point of view that the multi-junction solar cells with more

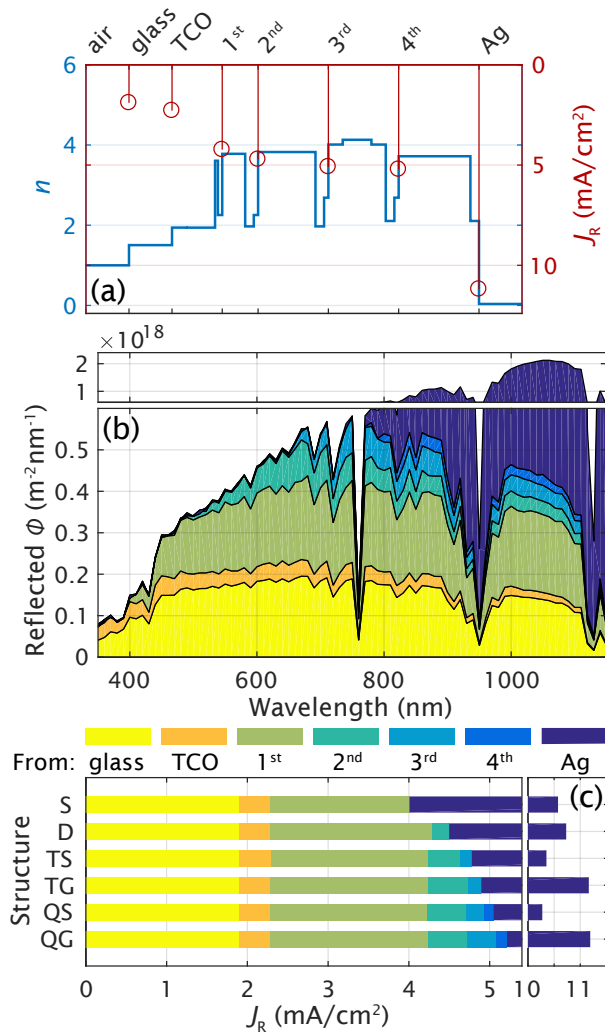


Figure 6.4: Reflection accumulated from different interfaces in multi-junction solar cells. (a) Left-axis: The profile of refractive index n against the depth in the cell, and Right-axis: the equivalent photocurrent J_R of the accumulated reflection up to certain interfaces, in the structure QG. (b) Spectral photon flux density of the accumulated reflection up to certain interfaces in the structure QG. (c) J_R of the studied structures, dissected with the contributions of different interfaces.

		D	TS	TG	QS	QG
	$J_{\text{ph-tot}}$ (mA/cm ²)	28.92	29.41	28.45	29.56	28.14
	J_{SC} (mA/cm ²)	14.46	9.80	9.48	7.39	7.03
(a) Lossless	V_{OC} (V)	1.453	2.128	2.340	3.029	3.241
	η (%)	16.18	16.07	17.09	17.24	17.55
(b) TRJ	ΔV_{OC} (mV)	-15	-30	-30	-45	-45
	V_{OC} (V)	1.438	2.098	2.310	2.984	3.196
	$\Delta \eta$ (%)	-0.17	-0.23	-0.22	-0.26	-0.24
	η (%)	16.01	15.84	16.87	16.98	17.31
(c) Filtered	ΔV_{OC} (mV)	-27.2	-73.7	-65.8	-137.4	-133.3
	V_{OC} (V)	1.426	2.054	2.274	2.892	3.107
	$\Delta \eta$ (%)	-0.30	-0.56	-0.48	-0.78	-0.72
	η (%)	15.87	15.51	16.61	16.45	16.83
(d) Combined	V_{OC} (V)	1.411	2.024	2.244	2.847	3.062
	η (%)	15.71	15.28	16.39	16.20	16.59

Table 6.5: Effects of voltage losses due to TRJs and filtered illumination. The photocurrent densities used for the calculations are derived from the optical simulations. The FF is fixed at 77%. (a) The baseline performance without voltage losses (Lossless), meaning that the V_{OC} is the sum of the component V_{OC} shown in Table 6.2. Then, either the effect of (b) TRJs or (c) filtered illumination is considered solely. (d) Both sources of losses are taken into account. In the calculation, $T = 298.15$ K is used.

subcells are more susceptible to parasitic losses, and thus also require more delicate design and better engineering to overcome the added hurdles.

6.5 Tunnel recombination junctions

As the subcells in two-terminal multi-junction solar cells are connected in series, the electrons/holes generated in a subcell need to recombine with the holes/electrons from the neighboring subcell, taking place near the border between the two subcells. Such process is facilitated by the tunnel recombination junction between the subcells, which can comprise the doped layers between the two absorber layers, possibly with other functional layer(s). When the recombination is not efficient enough, the accumulated carriers lead to a potential barrier and thus a drop in the output voltage of the solar cell.

The influence of TRJs on the studied structures of multi-junction TFSSCs was assessed. In Table 6.5, the total effective $J_{\text{ph-tot}}$ obtained in the optical simulations was listed to determine the J_{SC} used in this estimation. Together with the lossless V_{OC} given in Table 6.3 and a fixed FF of 77%, the derived efficiency η serves as the baseline in the analysis of the electrical losses. With J_{SC} adjusted by the simulations yet other parameters unchanged, the baseline efficiencies follow the same trend as the ones shown in Table 6.3. As a simplistic assumption, the loss of V_{OC} at a TRJ is assumed at a universal value of -15 mV per TRJ regardless of the actual structure.

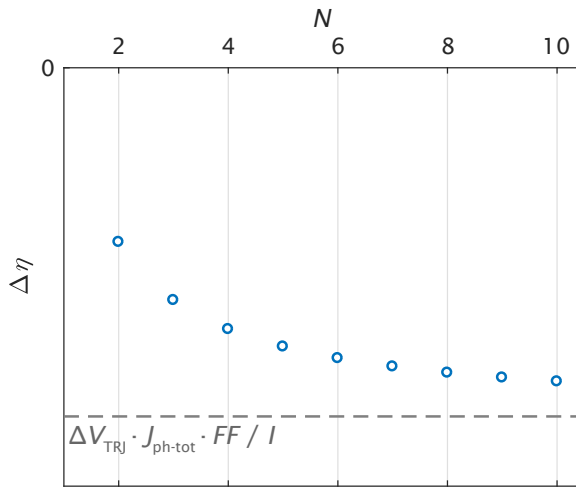


Figure 6.5: The loss in efficiency $\Delta\eta$ of multi-junction solar cells caused by the voltage drop at the TRJs. The magnitude of $\Delta\eta$ increases and saturates with the number of subcells N .

The value was chosen to represent a well-engineered TRJ with a minute amount of voltage drop [80], [169], [178], [192]. The resulted voltage and efficiency are shown in Table 6.5. Although the loss in voltage linearly increases with the number of TRJ, the loss in efficiency is not as severe when the number of subcells becomes large. In terms of the efficiency loss ($\Delta\eta$) caused by TRJs, the difference between the triple-junction and quadruple-junction structures in the same group is merely in the range of 10% relative.

The inconsistency between the losses in voltage and in efficiency can be explained by the change in current density. For a multi-junction solar cells consisting of N subcells and $N - 1$ TRJs, the loss in efficiency $\Delta\eta$ caused by TRJs is:

$$\Delta\eta = (N - 1) \cdot \Delta V_{\text{TRJ}} \cdot \frac{J_{\text{ph-tot}}}{N} \cdot FF/I \quad (6.2)$$

assuming the loss in V_{OC} caused by each TRJ is a constant ΔV_{TRJ} , the total photocurrent density $J_{\text{ph-tot}}$ is unchanged (under incident irradiance I) and perfectly distributed among all subcells. In Equation 6.2, the total losses in voltage increase by a factor of $N - 1$, while the current density counters the effect by a factor of N . Its effect on the efficiency is shown in Figure 6.5. With the increasing number of subcells, the loss in efficiency saturates, as Equation 6.2 becomes independent of N when N approaches infinity:

$$\Delta\eta|_{N \rightarrow \infty} = \Delta V_{\text{TRJ}} \cdot J_{\text{ph-tot}} \cdot FF/I \quad (6.3)$$

Such loss in efficiency equals 0.380% absolute considering the record $J_{\text{ph-tot}} = 32.9 \text{ mA/cm}^2$ and the previously defined ΔV_{TRJ} and FF . In effect, with a finite number of subcells, the $\Delta\eta$ generally worsens with the increased number of subcells. As a consequence,

the efficiency advantage of multi-junction cells with more subcells is narrowed by the deteriorative effect of TRJs.

6.6 Filtered illumination

From the optical perspective, the top subcell(s) in a multi-junction solar cell acts as an optical filter which absorbs a part of the incident spectrum and reduces the irradiance arriving at the bottom subcell(s). Because the component subcells may receive illumination of a lower level when compared with their single-junction counterparts under the same incident solar spectrum, their photovoltaic performance could be quite different from the single-junction.

In particular, the V_{OC} of a solar cell is dependent on the illumination level as:

$$V_{OC} = \frac{nkT}{e} \ln \frac{J_{ph}}{J_0} \quad (6.4)$$

where k and T are the Boltzmann constant and absolute temperature, respectively. At a given temperature, with a certain ideality factor n and dark saturation current density J_0 of the solar cell, the V_{OC} increases with the photocurrent density J_{ph} which is directly affected by the incident irradiance. Consequently, at two different illumination levels, the difference in V_{OC} of a solar cell is correlated to the ratio between the J_{ph} 's:

$$\Delta V_{OC} = V'_{OC} - V_{OC} = \frac{nkT}{e} \ln \frac{J'_{ph}}{J_{ph}} \quad (6.5)$$

where $[V_{OC}, J_{ph}]$ and $[V'_{OC}, J'_{ph}]$ are two pairs of parameters under different illumination levels. For instance, assuming at $T = 298.15$ K, a nc-Si:H cell which has an ideality factor of 1.5, V_{OC} of 0.550 V and J_{ph} of 26.0 mA/cm² under AM1.5G spectrum, if the J_{ph} is reduced to one fourth of its reference value due to the filtered illumination, then Equation 6.5 suggests a ΔV_{OC} of -53.43 mV and thus a V'_{OC} of 0.497 V under the filtered condition.

Equation 6.5 was applied to estimate the influence of filtered illumination on the performance of the studied multi-junction structures. In the calculation, the ideality factor of all subcells was simplistically predetermined at a universal value of 1.5, and the reference parameters $[V_{OC}, J_{ph}]$ were taken from Table 6.2. The result is shown in Table 6.5. Unlike the effect of TRJs, the loss in V_{OC} due to filtered illumination is not linear and it increases drastically with the number of subcells. The distribution of photocurrent to more subcells means less photocurrent generated in each subcell and greater deviation from the AM1.5G-reference performance of the single-junction counterparts. Equation 6.6 estimates how the filtered illumination affects the efficiency with increasing number of subcells.

$$\Delta\eta = \frac{nkT \cdot FF}{eI} \frac{J_{ph-tot}}{N} \ln \frac{1}{N!} \quad (6.6)$$

where $N!$ is the factorial of N . It assumes the ideal device structure in which the J_{ph} of the N th subcell is $1/N$ of the J_{ph} in the respective single-junction cell under

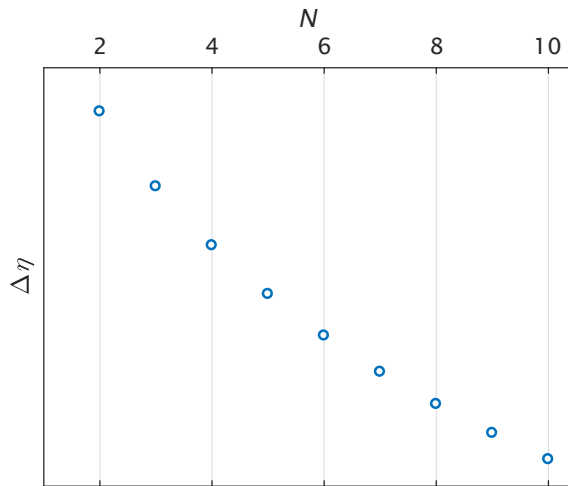


Figure 6.6: The loss in efficiency $\Delta\eta$ caused by the filtered illumination in multi-junction solar cells increases with the number of subcells N , derived by Equation 6.6.

AM1.5G spectrum. Such estimation of efficiency losses is illustrated in Figure 6.6. Both Table 6.5 and Figure 6.6 show that the difference in efficiency caused by filtered illumination clearly increases with the number of subcells. The considerable impact of filtered illumination limits the benefit of making multi-junction solar cells comprising a large number of subcells.

When the effects of TRJs and filtered illumination are both considered, the realistic photovoltaic performance of the multi-junction solar cells further deviates from the optimistic estimation. As shown in Table 6.5, without these voltage losses, the difference in efficiency is 0.91 % between D and TG, and 0.46 % between TG and QG. Such efficiency improvement is reduced to merely 0.68 % and 0.20 %, respectively, when both losses are included. Even though the exact performance of these structures still depends on the light-trapping scheme (J_{SC}) and other device optimization (FF), the trend is revealed that there is an optimal number of subcells and the addition of subcells does not guarantee further improvement.

6.7 Thickness limitations

The electronic transport properties of the materials can pose restrictions on the device structure, particularly on the thickness of the absorber layers. While thick absorber layers are desired for the optical absorption, thin layers are required to facilitate the carrier collection. In previous optical analyses, only the thickness of the bottommost nc-Si:H absorber layer was restricted at 3500 nm. The rest of the absorber layers were unconstrained to find the current-matching condition. The resultant structures are not always realistic. The top panel of Table 6.6 shows the absorber thicknesses in

Structure	t_1 (nm)	t_2 (nm)	t_3 (nm)	t_4 (nm)	t_{tot} (μm)	$J_{\text{ph-tot}}$ (mA/cm^2)	η (%)
D	549	3500	—	—	4.05	28.92	15.71
TS	196	2085	3500	—	5.78	29.41	15.28
TG	157	383	3500	—	4.04	28.45	16.39
QS	70.7	710	2812	3500	7.09	29.56	16.20
QG	61.1	531	817	3500	4.91	28.14	16.59
D w/ SOIR	285	3500	—	—	3.79	28.48	15.46
TG ltd.	128	250	1951	—	2.33	27.04	15.53
TG ltd. w/ SOIR	150	250	3212	—	3.61	28.18	16.22
QS w/ SOIR	64.7	332	2642	3500	6.54	28.92	15.83
QG ltd.	45.8	281	250	1125	1.70	25.37	14.88
QG ltd. w/ SOIR	48.7	315	250	1330	1.94	25.97	15.25

Table 6.6: The thicknesses of the absorber layers in the studied multi-junction structures, and the corresponding performance. t_1 means the absorber thickness of the first subcell from the surface of light incidence, etc. t_{tot} is the total thickness of all absorber layers. The values in bold indicate the thickness which was fixed in the current-matching algorithm of the simulations. The calculation of efficiency has included the influence of voltage losses.

the device structures of which the optical response is presented in Figure 6.2. The thicknesses of the (N)a-Si:H layers in structure D, QS and QG, and of the a-SiGe_x:H layers in structure TG and QG are too thick to be electrically favorable. Especially, the electrical performance of a-SiGe_x:H (sub)cells deteriorates sharply with the increase in absorber thickness. It renders these certain configurations less practical for application.

Two adjustments were therefore deployed to improve the realistic performance estimation of the studied multi-junction solar cells. Firstly, the thickness of the a-SiGe_x:H layer in structure TG and QG was fixed at 250 nm, a reasonable value for providing decent electrical performance. Secondly, an 100-nm-thick silicon oxide intermediate reflector (SOIR) [84], [93] was inserted in the revised structure TG and QG behind the a-SiGe_x:H subcell, as well as in structure D and QS behind the (N)a-Si:H subcell, to compensate the reduced absorption in the thinner absorber layers. The result of the adjusted simulations is summarized in the bottom panel of Table 6.6. Without an intentional intermediate reflector, the constrained structures TG ltd. and QG ltd. severely suffer from the weak optical absorption, generating 1.41 and 2.77 mA/cm² less total J_{ph} than their counterparts, respectively. The application of SOIR helps to bring the J_{ph} in the constrained TG back to a level comparable to the reference. A similar outcome is observed in the structure D and QS with SOIR, that the thicknesses of (N)a-Si:H are almost halved while the total J_{ph} only decreases by 0.44 and 0.64 mA/cm², respectively. On the other hand, the constrained QG cannot provide satisfactory J_{ph} even with SOIR. The limitation lies in the a-SiGe_x:H subcell that the required absorption is more than what it can realistically provide. It is true that the absorption spectrum of a-SiGe_x:H can be extended to longer wavelengths by incorporating more Ge atoms in the material, but the material with more Ge is more defective

that the feasible thickness will be further limited. Therefore, with the analyses of optical and electrical losses as well as the thickness limitation from the materials, the constrained structures reported in Table 6.6 provide a more realistic estimation of what can be achieved with these multi-junction structures. It is noteworthy that the estimated efficiencies of the structures D, TG and QG with SOIR presented in Table 6.6 align very well with the record initial efficiencies of the similar multi-junction structures reported in literature [80], [90], [192], when the difference in FF is taken into account.

6.8 Optimal number of subcells

The preceding sections reveal the influence of different loss mechanisms on the performance of multi-junction TFSSCs. The assessments demonstrate how the benefit of multi-junction cells can be compromised by several losses. On the other hand, the presented efficiencies are not meant to indicate the efficiency limit of this photovoltaic technology. The optical analyses thus the estimation of J_{SC} were based on the simulations on a certain type of light-trapping structure, which is the MST. The capability of a light-trapping structure is sometimes assessed by the achievable J_{SC} of the single-junction nc-Si:H cell on such structure. In this respect, the honeycomb structure deployed in $n-i-p$ configuration holds the record of 32.9 mA/cm^2 [113]. Our optical analyses might be extrapolated to the application of the honeycomb structure by assuming the same differences in total J_{ph} between the single-junction and multi-junction cells. For example, the total J_{ph} on the MST obtained in simulations is 28.86 and 25.97 mA/cm^2 for the single-junction S and the revised structure QG, respectively. Then, from 32.9 mA/cm^2 in the single-junction, the total J_{ph} in the revised QG on the honeycomb structure was speculated at 30.01 mA/cm^2 . By doing so, the implied efficiencies of structures D, TS, TG, QS and QG (all with SOIR and with thickness limitation considered) on the honeycomb structure were extrapolated to 17.78 , 17.51 , 18.67 , 18.17 and 17.75% , respectively, with all the voltage losses considered. The estimated efficiencies are higher with the better light-trapping structure, yet the general trend remains the same. Among the studied structures of TFSSCs, structure TG, the triple-junction cell with a-SiGe_x:H subcell, is the most promising in terms of initial efficiency.

The optimal number of subcells is decided by the balance between the gains and losses occurred in the multi-junction solar cells. The gains are typically identified as the increase in output voltage offered by the absorber materials with wider bandgap. Such gains are greater when the solar cells feature a higher ratio of eV_{OC}/E_g [196], where E_g is the bandgap. As it was demonstrated, the losses grow mainly with the number of subcells, not directly with the amount of gains. For TFSSCs, the optimum happens to be the triple-junction configuration. Beyond triple-junction, the additional losses become comparable to or even more than the gain in voltage.

The loss mechanisms investigated in this work are common to all two-terminal multi-junction solar cells. Therefore, similar analyses can be conducted for other photovoltaic material systems. However, the quantitative results cannot be directly transferred between different technologies, since the extent of influence of each loss

mechanism is decided by the specific materials and device structure. For example, the degree of optical loss will depend on the optical constants of the materials.

The optimum number of junctions may be different for different technologies. For a photovoltaic technology with higher eV_{OC}/E_g , such as the III-V solar cells, the significant gains leave more room for efficiency improvement by adding subcells before the losses neutralize the additional gains. This should be regarded as an important criterion when one considers developing multi-junction solar cells comprising a large number of subcells.

6.9 Variations in photocurrent generation

When multi-junction solar cells generate more power than the single-junction cell does, they also shift the operation regime to that of higher voltages and lower current densities because the component subcells are connected in series. As the current density becomes lower along such regime transition induced by increasing the number of subcells, the power conversion efficiency of the solar cells becomes more and more sensitive to any changes in the current density.

To illustrate, we can consider the structures and parameters presented in Table 6.3, where the photocurrents are perfectly matched between the subcells and the total J_{ph} are all the same at 32.9 mA/cm^2 . If a certain variation reduces the photocurrent in the single-junction cell by 1.0 mA/cm^2 , the J_{SC} goes down by 3.0%. In contrast, if a similar variation decreases the photocurrent in one of the subcells of a quadruple-junction cell by 1.0 mA/cm^2 , then the J_{SC} is also reduced by roughly 1.0 mA/cm^2 , which accounts for a relative reduction of 12.2%, considerably more than that in the single-junction. Apparently, the solar cell with a larger number of subcells is more susceptible to such variations.

The consequences of the susceptibility of multi-junction solar cells are twofold. In the first place, it requires very high standards for the accuracy, uniformity and reproducibility of the fabrication processes of the multi-junction cells, alongside the delicate engineering needed for realizing a well current-matched device. A difference in thickness of 10 nm in the top part of a cell can lead to a difference in photocurrent of more than 0.5 mA/cm^2 , which is significant in a multi-junction cell with many subcells. Therefore, any temporal or spatial inconsistency in the fabrication processes can result in a considerable discrepancy in the device performance. Beside the manufacturing, it also makes the development of high-efficiency multi-junction solar cells more difficult from the beginning.

Another problem of the susceptibility is in the terrestrial application. The solar spectrum incident at a certain location is subject to daily and seasonal variations. Not only the overall intensity but also the spectral distribution of the solar irradiation changes over time due to the influence of the celestial position, the atmosphere and the weather. Because of the aforementioned susceptibility, the spectral variations of sunlight can strongly impact the performance of multi-junction solar cells.

As a demonstration, the photocurrents of the studied structures in the top panel of Table 6.6 were derived under different solar spectra. The transmission model SPC-TRAL2 [197] was used to simulate the solar spectra in different seasons, namely the

summer (21 June), autumn (18 October) and winter (21 December) at noon of the given days. The incident surface was defined by coordinates of 52.00°N 4.37°E (Delft, The Netherlands), tilt angle of 37.0°, and azimuth angle of 180° (South). Together with the AM1.5G spectrum, the simulated spectra are depicted in Figure 6.7(a). With each solar spectrum, integrating the simulated spectral response of the multi-junction structures in Figure 6.2 by Equation 6.1 gives the J_{ph} of each subcell. Figure 6.8(a-c) shows the resulted J_{ph} for three multi-junction structures. Since their distribution of optical absorption was optimized for the AM1.5G spectrum, the photocurrents among the subcells are uniform under AM1.5G but have discrepancies under the seasonal spectra. To quantify the excess J_{ph} which cannot be utilized due to the series connection between the subcells, the ratio of photocurrent utilization (U) is defined as the ratio of the collectible J_{ph} to the total generated J_{ph} :

$$U = \frac{N J_{\text{ph-min}}}{\sum_{i=1}^N J_{\text{phi}}} \quad (6.7)$$

where J_{phi} is the J_{ph} of the i th subcell and $J_{\text{ph-min}}$ is the lowest one among all subcells in a multi-junction cell. In Figure 6.8, naturally, the ratio of photocurrent utilization is effectively 100 % under the AM1.5G spectrum.

In this example, among the seasonal solar spectra, the highest U is observed in autumn for all structures, while the lowest is in winter, as shown in Figure 6.8(d). This can be explained by the similarity/difference between the seasonal spectrum and the AM1.5G spectrum, for which the multi-junction structures were optimized. The degree of similarity is clearly illustrated in Figure 6.7(b), in which the spectral photon flux density Φ of the seasonal spectrum is normalized according to the respective value in AM1.5G spectrum $\Phi_{\text{AM1.5G}}$. Ideally, if a spectrum exhibits a horizontal line in this figure, such spectrum has the same spectral profile as the AM1.5G spectrum, then an AM1.5G-optimized multi-junction cell will operate in the current-matched condition under this spectrum. In Figure 6.7(b), the autumn spectrum shows mostly horizontal in this wavelength range, agrees with the highest U in the studied structures. In contrast, the summer spectrum is more intense in the short wavelengths while the winter one is more intense in the long wavelengths, both result in uneven distribution of J_{ph} and thus lower U . Therefore, it is evident that a multi-junction cell optimized for a certain solar spectrum will result in current mismatch thus incomplete photocurrent utilization under a different spectrum. It can also be observed in Figure 6.8(d) that the losses in U become larger with the increased number of subcells. In addition, the negative impact on the power conversion efficiency is further aggravated with the number of subcells because the influence of the lost J_{ph} is enlarged by the higher output voltage of the multi-junction cells with a large number of subcells. As a result, the more subcells a multi-junction solar cell has, the greater its photovoltaic performance suffers from changes in the solar spectrum.

The analysis with the simulated solar spectra decidedly demonstrates how the spectral variation can deteriorate the photocurrent utilization of multi-junction solar cells. It should be noted that the spectra shown in Figure 6.7(a) only take into account the solar position in relation to the location of the incident surface and emphasize the difference between the seasons. Besides, the solar spectrum is subjected to many other factors such as clouds, albedo, air composition, etc. All of the these factors can

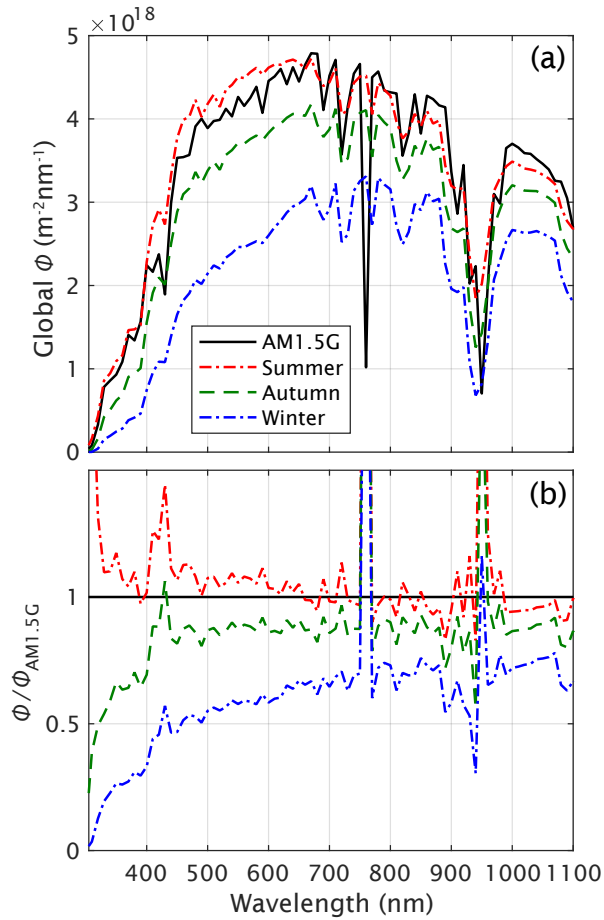


Figure 6.7: (a) Spectral photon flux density Φ of the solar spectra received at a certain location in Delft in different seasons, simulated by the model SPCTRAL2. The AM1.5G spectrum is also plotted as reference. (b) The seasonal spectra normalized to the AM1.5G spectrum, to visualize whether a spectrum has a similar spectral profile to AM1.5G.

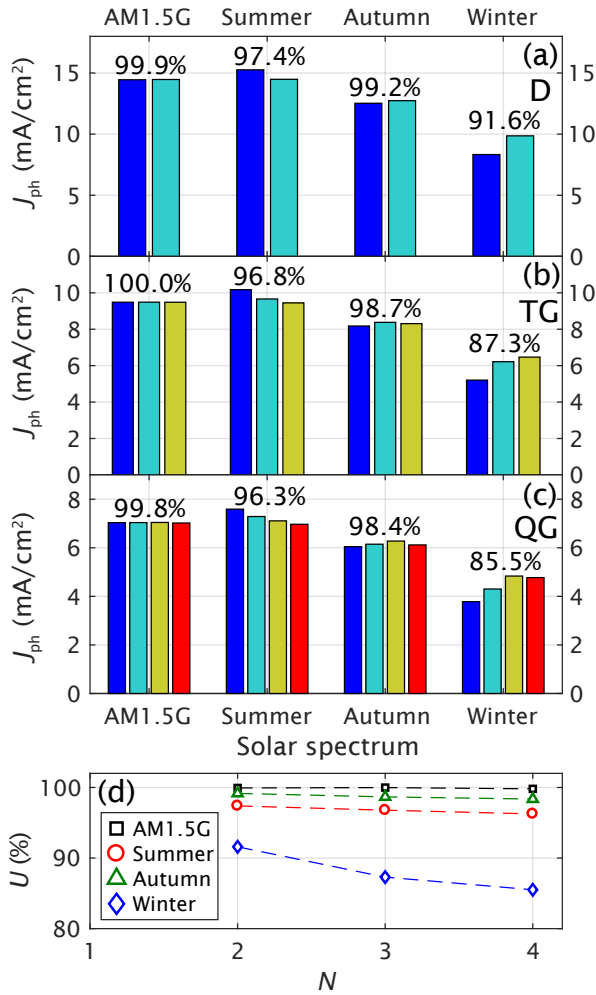


Figure 6.8: (a-c) The distribution of J_{ph} generated in the studied multi-junction structures under different solar spectra, and (d) the corresponding ratio of photocurrent utilization (U). The percentages indicated in panels (a-c) are the respective ratio U .

affect the photocurrent utilization in multi-junction solar cells, although the precise simulation of solar spectrum under different detailed circumstances is out of the scope of this study.

6.10 Conclusions

Is making multi-junction solar cells with a large number of subcells beneficial? Using the information from thin-film silicon photovoltaics, several loss mechanisms inherent in multi-junction cells have been discussed. Optically, both the parasitic absorption and reflection losses slightly increase with the number of subcells. The parasitic absorption is decided by the transparency of the supporting materials and the optical utilization of the topmost subcell. The reflection losses are raised whenever a new subcell is encountered by the light. Electrically, tunnel recombination junctions induce a drop in the output voltage, but the effect on the power conversion efficiency saturates at a large number of subcells. The influence of the filtered illumination received by the subcells appears to be more detrimental since the increase of voltage loss with the number of subcells is faster than a linear growth. Overall, the efficiency potential of multi-junction solar cells is decided by the losses counteracting the gains from the added subcells, which is largely determined by the ratio of the output voltage to the bandgap of the absorber materials. In generic terrestrial (i.e. non-concentration, non-tracking, and non-desert-climate) applications, multi-junction solar cells could be less appealing because the efficiency suffers from the daily and seasonal changes in the solar spectrum.

7

Conclusions and Outlook

In this thesis, quadruple-junction thin-film silicon-based solar cells have been extensively studied. The goal is to explore the potential of such device structures to achieve high performance. Can their performance surpass the best triple-junction TFSSCs, which are the record holder of the technology? Is it feasible to develop a device so complex? What are the strength and drawbacks? This study is to answer these questions.

7.1 Conclusions

Quadruple-junction TFSSCs in *p-i-n* superstrate configuration have been experimentally demonstrated and developed. Such activities are reported in Chapter 2 and 5. Chapter 2 described the fabrication of a-SiO_x:H/a-Si:H/nc-Si:H/nc-Si:H solar cells. The cells were deposited on micro-textured glass substrates, of which the surface morphology is smooth and favorable to the deposition of high-quality nc-Si:H materials. The output voltage of the subcells stacked up in the quadruple-junction cells without significant losses, resulting in a V_{OC} up to 2.91 V. The use of optical simulations based on GenPro4 [107] model facilitated the process of adjusting the absorber thickness and optical absorption in the subcells, in order to achieve current-matching condition under AM1.5G solar spectrum. When ITO was used as the front TCO, a total photocurrent density J_{ph} of 23.73 mA/cm² and a J_{SC} of 5.49 mA/cm² were obtained, leading to an initial efficiency of 11.4% with a FF of 73.9%. With this result, the feasibility of fabricating quadruple-junction TFSSCs with satisfactory V_{OC} and FF has been demonstrated.

Aiming at the use of four different absorber materials for achieving better spectral utilization in quadruple-junction TFSSCs, thin-film a-SiGe_x:H solar cells have been developed and reported in Chapter 4. a-SiGe_x:H can serve as a mid-range absorber, filling the gap between the spectral sensitivity/absorption edge of the a-Si:H and nc-Si:H absorbers. The distinctive point of this work from the previous developments of a-SiGe_x:H cells in literature is the full implementation of mixed-phase SiO_x:H doped materials. On the p-side, p-type SiO_x:H was used, and its the oxygen content thus the optical bandgap was adjusted for the optimal optoelectrical performance of the devices. On the n-side, after testing various material stacks with different buffer layers adjacent to the absorber layer, optimal performance was obtained with solely n-type SiO_x:H by creating a bandgap-grading region near the i-n interface. Having optical bandgap E_{Tauc} of 1.45 eV for the a-SiGe_x:H absorber, initial efficiencies of 8.83%

and 9.28% have been achieved on nano-textured $\text{SnO}_2\text{:F}$ and ZnO:B , respectively, as the front TCO. The successful use of only $\text{SiO}_x\text{:H}$ materials in the doped layers provides simplicity and flexibility in the design the multi-junction TFSSCs, because of the multifunctionality of such mixed-phase materials.

With $\text{a-SiGe}_x\text{:H}$ available as an additional absorber material, Chapter 5 reported the development of quadruple-junction TFSSCs comprising four different absorbers. The absorber combination was wide-gap (W) a-Si:H /narrow-gap (N) $\text{a-Si:H/a-SiGe}_x\text{:H/nc-Si:H}$. (W) a-Si:H is an alternative to $\text{a-SiO}_x\text{:H}$ as they have similar optical properties. Along the direction of light incidence, the four different absorber materials exhibit descending bandgap. As a result, the spectral utilization was improved from the initial attempt in Chapter 2, and the spectral overlap between the response of the subcells was suppressed. The electrical interconnection between the subcells were realized by a $\text{n-SiO}_x\text{:H/p-SiO}_x\text{:H}$ tunnel recombination junction. This simple TRJ structure showed less loss in V_{OC} thus better electrical performance than other TRJ structures in the comparison. The optical performance of the quadruple-junction cells was boosted by the use of modulated surface textured front electrode [90], which consisted of highly-transparent materials and was capable of scattering light in a broad range of wavelengths. A total J_{ph} of 25.33 mA/cm^2 was obtained. The achievable initial efficiency of this device structure was projected at 14.0%, should the optical absorption be better distributed and the parasitic losses be limited.

With the experience and insights accumulated in the development of quadruple-junction TFSSCs, Chapter 6 assessed the efficiency potential of multi-junction solar cells in a thorough and critical manner. The optical and electrical losses related to the formation of multi-junction cells were evaluated. Optical simulations were performed on multi-junction structures with different numbers of subcells and different combinations of absorber materials. The simulations revealed that the parasitic absorption and reflection losses slightly increase with the number of subcells. The main constraint on the optical performance comes from the electrically-favorable thickness of the absorber layers, especially for defective materials like $\text{a-SiGe}_x\text{:H}$. Electrically, the TRJs used between the subcells deteriorate the output voltage of the multi-junction cells, but the impact on the energy conversion efficiency saturates with the number of subcells. The dominant factor of efficiency losses in multi-junction cells with a large number of subcells was shown to be the reduced illumination in the subcells. A subcell acts as an optical filter in front of the subsequent subcells, which consequently receive less illumination and generate lower output voltage than that under the full AM1.5G illumination. With all considerations, the gains and losses in multi-junction cells suggest that the triple-junction cell can provide the highest initial efficiency among all multi-junction structures for TFSSCs. However, extra attention should be given to the susceptibility of multi-junction solar cells to the changes in solar spectrum, as these changes pose a greater detrimental effect to the efficiency of the devices with a large number of subcells.

The spectral response measurement of multi-junction solar cells is prone to measurement artifacts and data misinterpretation. In Chapter 3, the data acquisition and artifact formation in the spectral response measurement have been studied in-depth by means of modeling. The modeling illustrated how the properties of the solar cell and the bias conditions affect the result of the measurement. The signal acquired in

the measurement is dependent on the response of each subcell to the excitation as well as the interactions between the subcells connected in series. The shunt resistance of the subcells, and the spectral profile and intensity of the bias light largely change the J - V characteristics of the subcells. Such J - V characteristics together with the bias voltage determine the operation points of a multi-junction cell and its subcells during the measurement. At their operation points, the subcell with the lowest differential conductance dJ/dV influences the measured signal the most. In a measurement, the lowest dJ/dV should be fulfilled for the subcell being measured, meaning that the rest of the subcells should receive bias light of high intensity and a medium bias voltage is also required. The basic principle is that the cell and subcells should be configured in a way that the subcell being measured is in a condition similar to the working condition of interest. In contrast to the common belief, the J_{SC} of a multi-junction cell may not be directly determined by the measured spectral response, even when the result is free of artifacts. Thoughtful considerations are suggested for the data interpretation. Finally, the modeling tool developed in this work can facilitate the process of finding the optimal measurement conditions, that is especially useful when studying novel device architectures.

7.2 Outlook

The following ideas have been perceived from the understanding gained in this thesis, which may serve as recommendations for the research in the future.

1. To further improve the energy conversion efficiency of quadruple-junction thin-film silicon solar cells from the current record of 15.0% [192], the potential of the substrate n - i - p configuration could be investigated. Advanced light-trapping structures such as the honeycomb structure, which has resulted in the highest photocurrent density in TFSSCs so far [113], could be incorporated in n - i - p quadruple-junction cells. Furthermore, the substrate configuration also gives more control over the anti-reflection coatings, which is needed for the sophisticated light management of such devices. Combining state-of-the-art materials and device optimization for a-SiGe_x:H cells, an initial efficiency more than 17% is in reach.
2. Spectral beam splitting [198], [199] is an interesting topic to study in the pursuit of high energy conversion efficiency and high annual energy yield from an integrated photovoltaic device comprising multiple absorber materials. Two-terminal multi-junction solar cells are susceptible to changes in the solar spectrum, while four-or-more-terminal multi-junction solar cells are limited by many extra restrictions and compromises required in the design and fabrication processes. Spectral beam splitting spatially divides the incident illumination into separate beams, each of which consists of photons in a certain range of wavelength. Different parts of the solar spectrum are harvested by different solar cells with suitable absorber materials. This concept allows the use of single-junction solar cells from different PV technologies without compatibility issues. The cells can be individually and independently optimized for the assigned wavelengths.

Remarkably, because each cell operates independently with a certain part of the spectrum, spectral variations do not harm the performance of such devices, unlike two-terminal multi-junction cells. The challenges in this topic would be to improve the performance and reduce the cost of the spectral beam splitting optics.

Bibliography

- [1] UNFCCC, *Paris Agreement*, 2015.
- [2] A. Kojima, K. Teshima, Y. Shirai, and T. Miyasaka, "Organometal Halide Perovskites as Visible-Light Sensitizers for Photovoltaic Cells," *Journal of the American Chemical Society*, vol. 131, no. 17, pp. 6050–6051, 2009. DOI: [10.1021/ja809598r](https://doi.org/10.1021/ja809598r).
- [3] W. S. Yang, B.-W. Park, E. H. Jung, N. J. Jeon, Y. C. Kim, D. U. Lee, S. S. Shin, J. Seo, E. K. Kim, J. H. Noh, and S. I. Seok, "Iodide management in formamidinium-lead-halide-based perovskite layers for efficient solar cells," *Science*, vol. 356, no. 6345, pp. 1376–1379, 2017.
- [4] W. Spear and P. Le Comber, "Substitutional doping of amorphous silicon," *Solid State Communications*, vol. 17, no. 9, pp. 1193–1196, 1975. DOI: [10.1016/0038-1098\(75\)90284-7](https://doi.org/10.1016/0038-1098(75)90284-7).
- [5] D. E. Carlson and C. R. Wronski, "Amorphous silicon solar cell," *Applied Physics Letters*, vol. 28, no. 11, pp. 671–673, 1976. DOI: [10.1063/1.88617](https://doi.org/10.1063/1.88617).
- [6] O. Isabella, "Light management in thin-film silicon solar cells," PhD thesis, Delft University of Technology, 2013. DOI: [10.4233/uuid:03ae8b9c-6d4d-4653-8071-4b667f559e52](https://doi.org/10.4233/uuid:03ae8b9c-6d4d-4653-8071-4b667f559e52).
- [7] H. Sterling and R. Swann, "Chemical vapour deposition promoted by r.f. discharge," *Solid-State Electronics*, vol. 8, no. 8, pp. 653–654, 1965. DOI: [10.1016/0038-1101\(65\)90033-X](https://doi.org/10.1016/0038-1101(65)90033-X).
- [8] R. C. Chittick, J. H. Alexander, and H. F. Sterling, "The Preparation and Properties of Amorphous Silicon," *Journal of The Electrochemical Society*, vol. 116, no. 1, p. 77, 1969. DOI: [10.1149/1.2411779](https://doi.org/10.1149/1.2411779).
- [9] S. Vepřek and V. Mareček, "The preparation of thin layers of Ge and Si by chemical hydrogen plasma transport," *Solid-State Electronics*, vol. 11, no. 7, pp. 683–684, 1968. DOI: [10.1016/0038-1101\(68\)90071-3](https://doi.org/10.1016/0038-1101(68)90071-3).
- [10] P. Torres, J. Meier, R. Flückiger, U. Kroll, J. A. A. Selvan, H. Keppner, A. Shah, S. D. Littelwood, I. E. Kelly, and P. Giannelis, "Device grade microcrystalline silicon owing to reduced oxygen contamination," *Applied Physics Letters*, vol. 69, no. 10, pp. 1373–1375, 1996. DOI: [10.1063/1.117440](https://doi.org/10.1063/1.117440).
- [11] S. Hänni, "Microcrystalline Silicon for High-Efficiency Thin-Film Photovoltaic Devices," PhD thesis, École polytechnique fédérale de Lausanne, 2014, p. 165. DOI: [10.5075/epfl-thesis-6288](https://doi.org/10.5075/epfl-thesis-6288).
- [12] D. A. Anderson and W. E. Spear, "Electrical and optical properties of amorphous silicon carbide, silicon nitride and germanium carbide prepared by the glow discharge technique," *Philosophical Magazine*, vol. 35, no. 1, pp. 1–16, 1977. DOI: [10.1080/14786437708235967](https://doi.org/10.1080/14786437708235967).

- [13] J. N. Bullock, C. Bechinger, D. K. Benson, and H. M. Branz, "Semi-transparent a-SiC:H solar cells for self-powered photovoltaic-electrochromic devices," *Journal of Non-Crystalline Solids*, vol. 198-200, pp. 1163–1167, 1996. DOI: [10.1016/0022-3093\(96\)00105-6](https://doi.org/10.1016/0022-3093(96)00105-6).
- [14] K. Haga, K. Yamamoto, M. Kumano, and H. Watanabe, "Wide Optical-Gap a-Si:O:H Films Prepared from SiH₄-CO₂ Gas Mixture," *Japanese Journal of Applied Physics*, vol. 25, no. Part 2, No. 1, pp. L39–L41, 1986. DOI: [10.1143/JJAP.25.L39](https://doi.org/10.1143/JJAP.25.L39).
- [15] S. Inthisang, K. Sriprapha, S. Miyajima, A. Yamada, and M. Konagai, "Hydrogenated Amorphous Silicon Oxide Solar Cells Fabricated near the Phase Transition between Amorphous and Microcrystalline Structures," *Japanese Journal of Applied Physics*, vol. 48, no. 12, p. 122402, 2009. DOI: [10.1143/JJAP.48.122402](https://doi.org/10.1143/JJAP.48.122402).
- [16] W. Paul, D. K. Paul, B. von Roedern, J. Blake, and S. Oguz, "Preferential Attachment of H in Amorphous Hydrogenated Binary Semiconductors and Consequent Inferior Reduction of Pseudogap State Density," *Physical Review Letters*, vol. 46, no. 15, pp. 1016–1020, 1981. DOI: [10.1103/PhysRevLett.46.1016](https://doi.org/10.1103/PhysRevLett.46.1016).
- [17] B. von Roedern, D. K. Paul, J. Blake, R. W. Collins, G. Model, and W. Paul, "Optical absorption, photoconductivity, and photoluminescence of glow-discharge amorphous Si_{1-x}Ge_x alloys," *Physical Review B*, vol. 25, no. 12, pp. 7678–7687, 1982. DOI: [10.1103/PhysRevB.25.7678](https://doi.org/10.1103/PhysRevB.25.7678).
- [18] S. Guha, "Light-induced effects in amorphous silicon alloys - Design of solar cells with improved stability," *Journal of Non-Crystalline Solids*, vol. 77-78, pp. 1451–1460, 1985. DOI: [10.1016/0022-3093\(85\)90928-7](https://doi.org/10.1016/0022-3093(85)90928-7).
- [19] G. Ganguly, T. Ikeda, T. Nishimiya, K. Saitoh, M. Kondo, and A. Matsuda, "Hydrogenated microcrystalline silicon germanium: A bottom cell material for amorphous silicon-based tandem solar cells," *Applied Physics Letters*, vol. 69, no. 27, pp. 4224–4226, 1996. DOI: [10.1063/1.116993](https://doi.org/10.1063/1.116993).
- [20] T. Matsui, M. Kondo, K. Ogata, T. Ozawa, and M. Isomura, "Influence of alloy composition on carrier transport and solar cell properties of hydrogenated microcrystalline silicon-germanium thin films," *Applied Physics Letters*, vol. 89, no. 14, p. 142115, 2006. DOI: [10.1063/1.2358318](https://doi.org/10.1063/1.2358318).
- [21] D. L. Staebler and C. R. Wronski, "Reversible conductivity changes in discharge-produced amorphous Si," *Applied Physics Letters*, vol. 31, no. 4, pp. 292–294, 1977. DOI: [10.1063/1.89674](https://doi.org/10.1063/1.89674).
- [22] M. Stuckelberger, "Hydrogenated amorphous silicon: impact of process conditions on material properties and solar cell efficiency," PhD thesis, École polytechnique fédérale de Lausanne EPFL, 2014, p. 249. DOI: [10.5075/EPFL-THESIS-6393](https://doi.org/10.5075/EPFL-THESIS-6393).
- [23] J. Melskens, "Hydrogenated amorphous silicon: nanostructure and defects," PhD thesis, Delft University of Technology, 2015, p. 147. DOI: [10.4233/uuid:13d60d5e-3d68-4ac7-b2b6-a867cc393231](https://doi.org/10.4233/uuid:13d60d5e-3d68-4ac7-b2b6-a867cc393231).

- [24] E. Yablonovitch and G. Cody, "Intensity enhancement in textured optical sheets for solar cells," *IEEE Transactions on Electron Devices*, vol. 29, no. 2, pp. 300–305, 1982. DOI: [10.1109/T-ED.1982.20700](https://doi.org/10.1109/T-ED.1982.20700).
- [25] O. Kluth, B. Rech, L. Houben, S. Wieder, G. Schöpe, C. Beneking, H. Wagner, A. Löffl, and H. Schock, "Texture etched ZnO:Al coated glass substrates for silicon based thin film solar cells," *Thin Solid Films*, vol. 351, no. 1-2, pp. 247–253, 1999. DOI: [10.1016/S0040-6090\(99\)00085-1](https://doi.org/10.1016/S0040-6090(99)00085-1).
- [26] J. Krč, M. Zeman, O. Kluth, F. Smole, and M. Topič, "Effect of surface roughness of ZnO:Al films on light scattering in hydrogenated amorphous silicon solar cells," *Thin Solid Films*, vol. 426, no. 1-2, pp. 296–304, 2003. DOI: [10.1016/S0040-6090\(03\)00006-3](https://doi.org/10.1016/S0040-6090(03)00006-3).
- [27] E. Bunte, W. Zhang, J. Worbs, H. Siekmann, J. Kirchhoff, A. Gordijn, and J. Hüpkes, "Textured glass for silicon thin film solar cells," in *24th European Photovoltaic Solar Energy Conference*, Hamburg, 2009, pp. 2789–2792.
- [28] O. Isabella, P. Liu, B. Bolman, J. Krc, A. H. M. Smets, and M. Zeman, "Modulated surface-textured substrates with high haze: From concept to application in thin-film silicon solar cells," in *37th IEEE Photovoltaic Specialists Conference*, IEEE, 2011, pp. 000 616–000 621. DOI: [10.1109/PVSC.2011.6186029](https://doi.org/10.1109/PVSC.2011.6186029).
- [29] H. Tan, E. Psomadaki, O. Isabella, M. Fischer, P. Babal, R. Vasudevan, M. Zeman, and A. H. M. Smets, "Micro-textures for efficient light trapping and improved electrical performance in thin-film nanocrystalline silicon solar cells," *Applied Physics Letters*, vol. 103, no. 17, p. 173 905, 2013. DOI: [10.1063/1.4826639](https://doi.org/10.1063/1.4826639).
- [30] G. Yang, R. A. C. M. M. van Swaaij, S. Dobrovolskiy, and M. Zeman, "Textured substrate for high-efficiency n-i-p $\mu\text{c-Si:H}$ solar cells," in *2013 IEEE 39th Photovoltaic Specialists Conference (PVSC)*, IEEE, 2013, pp. 0624–0627. DOI: [10.1109/PVSC.2013.6744228](https://doi.org/10.1109/PVSC.2013.6744228).
- [31] G. Yang, R. A. C. M. M. van Swaaij, O. Isabella, and M. Zeman, "A novel way of texturing glass for microcrystalline silicon thin film solar cells application," *Progress in Photovoltaics: Research and Applications*, vol. 23, no. 10, pp. 1283–1290, 2015. DOI: [10.1002/pip.2550](https://doi.org/10.1002/pip.2550).
- [32] K. Söderström, J. Escarré, O. Cubero, F.-J. Haug, S. Perregaux, and C. Ballif, "UV-nano-imprint lithography technique for the replication of back reflectors for n-i-p thin film silicon solar cells," *Progress in Photovoltaics: Research and Applications*, vol. 19, no. 2, pp. 202–210, 2011. DOI: [10.1002/pip.1003](https://doi.org/10.1002/pip.1003).
- [33] C. Battaglia, J. Escarré, K. Söderström, L. Erni, L. Ding, G. Bugnon, A. Billet, M. Boccard, L. Barraud, S. De Wolf, F.-J. Haug, M. Despeisse, and C. Ballif, "Nanoimprint lithography for high-efficiency thin-film silicon solar cells," *Nano letters*, vol. 11, no. 2, pp. 661–5, 2011. DOI: [10.1021/nl1037787](https://doi.org/10.1021/nl1037787).
- [34] T. Papakonstantinou, "Ultra violet nanoimprint lithography for photonic structures applied in thin-film silicon solar cells," Master's thesis, Delft University of Technology, 2014, p. 133.

- [35] K. Sato, T. Oyama, M. Kambe, K. Masumo, and N. Taneda, "Highly Textured SnO₂ Films for a-Si/ μ c-Si Tandem Solar Cells," in *23rd European Photovoltaic Solar Energy Conference and Exhibition*, Valencia, Spain: WIP-Munich, 2008, pp. 2084–2087. DOI: [10.4229/23RDEUPVSEC2008-3C0.9.1](https://doi.org/10.4229/23RDEUPVSEC2008-3C0.9.1).
- [36] G. Yue, L. Sivec, J. M. Owens, B. Yan, J. Yang, and S. Guha, "Optimization of back reflector for high efficiency hydrogenated nanocrystalline silicon solar cells," *Applied Physics Letters*, vol. 95, no. 26, p. 263 501, 2009. DOI: [10.1063/1.3279143](https://doi.org/10.1063/1.3279143).
- [37] B. Yan, G. Yue, L. Sivec, J. M. Owens, K. Lord, J. Yang, S. Guha, and C.-S. Jiang, "Light trapping effect from randomized textures of Ag/ZnO back reflector on hydrogenated amorphous and nanocrystalline silicon based solar cells," in *SPIE Solar Energy + Technology*, A. E. Delahoy and L. A. Eldada, Eds., International Society for Optics and Photonics, 2010, pp. 777102–777102–7. DOI: [10.1117/12.859867](https://doi.org/10.1117/12.859867).
- [38] A. Hongsingthong, T. Krajangsang, I. A. Yunaz, S. Miyajima, and M. Konagai, "ZnO Films with Very High Haze Value for Use as Front Transparent Conductive Oxide Films in Thin-Film Silicon Solar Cells," *Applied Physics Express*, vol. 3, no. 5, p. 051 102, 2010. DOI: [10.1143/APEX.3.051102](https://doi.org/10.1143/APEX.3.051102).
- [39] B. Yan, G. Yue, L. Sivec, J. Owens-Mawson, J. Yang, and S. Guha, "Correlation of texture of Ag/ZnO back reflector and photocurrent in hydrogenated nanocrystalline silicon solar cells," *Solar Energy Materials and Solar Cells*, vol. 104, pp. 13–17, 2012. DOI: [10.1016/j.solmat.2012.04.036](https://doi.org/10.1016/j.solmat.2012.04.036).
- [40] E. Moulin, J. Sukmanowski, M. Schulte, A. Gordijn, F. Royer, and H. Stiebig, "Thin-film silicon solar cells with integrated silver nanoparticles," *Thin Solid Films*, vol. 516, no. 20, pp. 6813–6817, 2008. DOI: [10.1016/j.tsf.2007.12.018](https://doi.org/10.1016/j.tsf.2007.12.018).
- [41] F. J. Beck, S. Mokkaapati, and K. R. Catchpole, "Plasmonic light-trapping for Si solar cells using self-assembled, Ag nanoparticles," *Progress in Photovoltaics: Research and Applications*, vol. 18, no. 7, pp. 500–504, 2010. DOI: [10.1002/pip.1006](https://doi.org/10.1002/pip.1006).
- [42] H. A. Atwater and A. Polman, "Plasmonics for improved photovoltaic devices," *Nature Materials*, vol. 9, no. 3, pp. 205–213, 2010. DOI: [10.1038/nmat2629](https://doi.org/10.1038/nmat2629).
- [43] U. W. Paetzold, E. Moulin, D. Michaelis, W. Böttler, C. Wächter, V. Hagemann, M. Meier, R. Carius, and U. Rau, "Plasmonic reflection grating back contacts for microcrystalline silicon solar cells," *Applied Physics Letters*, vol. 99, no. 18, p. 181 105, 2011. DOI: [10.1063/1.3657513](https://doi.org/10.1063/1.3657513).
- [44] J. Bhattacharya, N. Chakravarty, S. Pattnaik, W. Dennis Slafer, R. Biswas, and V. L. Dalal, "A photonic-plasmonic structure for enhancing light absorption in thin film solar cells," *Applied Physics Letters*, vol. 99, no. 13, p. 131 114, 2011. DOI: [10.1063/1.3641469](https://doi.org/10.1063/1.3641469).

- [45] C. Eminian, F.-J. Haug, O. Cubero, X. Niquille, and C. Ballif, "Photocurrent enhancement in thin film amorphous silicon solar cells with silver nanoparticles," *Progress in Photovoltaics: Research and Applications*, vol. 19, no. 3, pp. 260–265, 2011. DOI: [10.1002/pip.1015](https://doi.org/10.1002/pip.1015).
- [46] T. L. Temple and D. M. Bagnall, "Broadband scattering of the solar spectrum by spherical metal nanoparticles," *Progress in Photovoltaics: Research and Applications*, vol. 21, no. 4, pp. 600–611, 2012. DOI: [10.1002/pip.1237](https://doi.org/10.1002/pip.1237).
- [47] J. Chantana, Y. Yang, Y. Sobajima, C. Sada, A. Matsuda, and H. Okamoto, "Localized surface plasmon enhanced microcrystalline–silicon solar cells," *Journal of Non-Crystalline Solids*, vol. 358, no. 17, pp. 2319–2323, 2012. DOI: [10.1016/j.jnoncrysol.2011.12.038](https://doi.org/10.1016/j.jnoncrysol.2011.12.038).
- [48] H. Tan, R. Santbergen, A. H. M. Smets, and M. Zeman, "Plasmonic Light Trapping in Thin-film Silicon Solar Cells with Improved Self-Assembled Silver Nanoparticles," *Nano Letters*, vol. 12, no. 8, pp. 4070–4076, 2012. DOI: [10.1021/nl301521z](https://doi.org/10.1021/nl301521z).
- [49] B. Niesen, B. P. Rand, P. Van Dorpe, D. Cheyns, L. Tong, A. Dmitriev, and P. Heremans, "Plasmonic Efficiency Enhancement of High Performance Organic Solar Cells with a Nanostructured Rear Electrode," *Advanced Energy Materials*, vol. 3, no. 2, pp. 145–150, 2013. DOI: [10.1002/aenm.201200289](https://doi.org/10.1002/aenm.201200289).
- [50] U. W. Paetzold, "Light Trapping with Plasmonic Back Contacts in Thin-Film Silicon Solar Cells," PhD thesis, Forschungszentrum Jülich, 2013, p. 175.
- [51] H. Tan, R. Santbergen, G. Yang, A. H. M. Smets, and M. Zeman, "Combined Optical and Electrical Design of Plasmonic Back Reflector for High-Efficiency Thin-Film Silicon Solar Cells," *IEEE Journal of Photovoltaics*, vol. 3, no. 1, pp. 53–58, 2013. DOI: [10.1109/JPHOTOV.2012.2220528](https://doi.org/10.1109/JPHOTOV.2012.2220528).
- [52] H. Tan, L. Sivec, B. Yan, R. Santbergen, M. Zeman, and A. H. M. Smets, "Improved light trapping in microcrystalline silicon solar cells by plasmonic back reflector with broad angular scattering and low parasitic absorption," *Applied Physics Letters*, vol. 102, no. 15, p. 153902, 2013. DOI: [10.1063/1.4802451](https://doi.org/10.1063/1.4802451).
- [53] H. Tan, "Materials and Light Management for High-Efficiency Thin-Film Silicon Solar Cells," PhD thesis, Delft University of Technology, 2015, p. 138. DOI: [doi:10.4233/uuid:847f7430-26d3-4034-bc9c-32f394bd9495](https://doi.org/doi:10.4233/uuid:847f7430-26d3-4034-bc9c-32f394bd9495).
- [54] H. Sai, H. Fujiwara, M. Kondo, and Y. Kanamori, "Enhancement of light trapping in thin-film hydrogenated microcrystalline Si solar cells using back reflectors with self-ordered dimple pattern," *Applied Physics Letters*, vol. 93, no. 14, p. 143501, 2008. DOI: [10.1063/1.2993351](https://doi.org/10.1063/1.2993351).
- [55] Z. Yu, A. Raman, and S. Fan, "Fundamental limit of nanophotonic light trapping in solar cells," *Proceedings of the National Academy of Sciences of the United States of America*, vol. 107, no. 41, pp. 17491–17496, 2010. DOI: [10.1073/pnas.1008296107](https://doi.org/10.1073/pnas.1008296107).

- [56] A. Čampa, O. Isabella, R. van Erven, P. Peeters, H. Borg, J. Krč, M. Topič, and M. Zeman, "Optimal design of periodic surface texture for thin-film a-Si:H solar cells," *Progress in Photovoltaics: Research and Applications*, vol. 18, no. 3, pp. 160–167, 2010. DOI: [10.1002/pip.940](https://doi.org/10.1002/pip.940).
- [57] V. E. Ferry, M. A. Verschuuren, M. C. van Lare, R. E. I. Schropp, H. A. Atwater, and A. Polman, "Optimized Spatial Correlations for Broadband Light Trapping Nanopatterns in High Efficiency Ultrathin Film a-Si:H Solar Cells," *Nano Letters*, vol. 11, no. 10, pp. 4239–4245, 2011. DOI: [10.1021/nl202226r](https://doi.org/10.1021/nl202226r).
- [58] H. Sai, K. Saito, and M. Kondo, *Enhanced photocurrent and conversion efficiency in thin-film microcrystalline silicon solar cells using periodically textured back reflectors with hexagonal dimple arrays*, 2012. DOI: [10.1063/1.4761956](https://doi.org/10.1063/1.4761956).
- [59] J. Kim, A. J. Hong, J.-W. Nah, B. Shin, F. M. Ross, and D. K. Sadana, "Three-Dimensional a-Si:H Solar Cells on Glass Nanocone Arrays Patterned by Self-Assembled Sn Nanospheres," *ACS Nano*, vol. 6, no. 1, pp. 265–271, 2012. DOI: [10.1021/nm203536x](https://doi.org/10.1021/nm203536x).
- [60] E. R. Martins, J. Li, Y. Liu, J. Zhou, and T. F. Krauss, "Engineering gratings for light trapping in photovoltaics: The supercell concept," *Physical Review B*, vol. 86, no. 4, p. 041404, 2012. DOI: [10.1103/PhysRevB.86.041404](https://doi.org/10.1103/PhysRevB.86.041404).
- [61] C. Battaglia, C.-M. Hsu, K. Söderström, J. Escarré, F.-J. Haug, M. Charrière, M. Boccard, M. Despeisse, D. T. L. Alexander, M. Cantoni, Y. Cui, and C. Ballif, "Light Trapping in Solar Cells: Can Periodic Beat Random?" *ACS Nano*, vol. 6, no. 3, pp. 2790–2797, 2012. DOI: [10.1021/nm300287j](https://doi.org/10.1021/nm300287j).
- [62] H. Sai, K. Saito, N. Hozuki, and M. Kondo, "Relationship between the cell thickness and the optimum period of textured back reflectors in thin-film microcrystalline silicon solar cells," *Applied Physics Letters*, vol. 102, no. 5, p. 053509, 2013. DOI: [10.1063/1.4790642](https://doi.org/10.1063/1.4790642).
- [63] O. Isabella, S. Solntsev, D. Caratelli, and M. Zeman, "3-D optical modeling of thin-film silicon solar cells on diffraction gratings," *Progress in Photovoltaics: Research and Applications*, vol. 21, no. 1, pp. 94–108, 2013. DOI: [10.1002/pip.1257](https://doi.org/10.1002/pip.1257).
- [64] S. Solntsev, O. Isabella, D. Caratelli, and M. Zeman, "Thin-Film Silicon Solar Cells on 1-D Periodic Gratings With Nonconformal Layers: Optical Analysis," *IEEE Journal of Photovoltaics*, vol. 3, no. 1, pp. 46–52, 2013. DOI: [10.1109/JPHOTOV.2012.2220123](https://doi.org/10.1109/JPHOTOV.2012.2220123).
- [65] C. S. Schuster, "Diffractive Optics for thin-film silicon solar cells," PhD thesis, University of York, 2015, p. 145.
- [66] G. B. Haxel, J. B. Hedrick, and G. J. Orris, *Rare Earth Elements—Critical Resources for High Technology*, 2002.
- [67] *HyET Solar BV*.
- [68] H. Águas, T. Mateus, A. Vicente, D. Gaspar, M. J. Mendes, W. A. Schmidt, L. Pereira, E. Fortunato, and R. Martins, "Thin Film Silicon Photovoltaic Cells on Paper for Flexible Indoor Applications," *Advanced Functional Materials*, vol. 25, no. 23, pp. 3592–3598, 2015. DOI: [10.1002/adfm.201500636](https://doi.org/10.1002/adfm.201500636).

- [69] J.-H. Yoon, J. Song, and S.-J. Lee, "Practical application of building integrated photovoltaic (BIPV) system using transparent amorphous silicon thin-film PV module," *Solar Energy*, vol. 85, no. 5, pp. 723–733, 2011. DOI: [10.1016/j.solener.2010.12.026](https://doi.org/10.1016/j.solener.2010.12.026).
- [70] H. Maurus, M. Schmid, B. Blersch, P. Lechner, and H. Schade, "PV for buildings," *Refocus*, vol. 5, no. 6, pp. 22–27, 2004. DOI: [10.1016/S1471-0846\(04\)00255-0](https://doi.org/10.1016/S1471-0846(04)00255-0).
- [71] A. Smets, M. Zeman, R. van Swaaij, O. Isabella, R. Vasudevan, S. Izadkhast, L. Ramirez, and P. Bauer, *MicroMasters Program on Solar Energy Engineering*, 2017.
- [72] W. Shockley and H. J. Queisser, "Detailed Balance Limit of Efficiency of p-n Junction Solar Cells," *Journal of Applied Physics*, vol. 32, no. 3, p. 510, 1961. DOI: [10.1063/1.1736034](https://doi.org/10.1063/1.1736034).
- [73] S. Rühle, "Tabulated values of the Shockley–Queisser limit for single junction solar cells," *Solar Energy*, vol. 130, pp. 139–147, 2016. DOI: [10.1016/j.solener.2016.02.015](https://doi.org/10.1016/j.solener.2016.02.015).
- [74] A. S. Brown and M. A. Green, "Detailed balance limit for the series constrained two terminal tandem solar cell," *Physica E: Low-dimensional Systems and Nanostructures*, vol. 14, no. 1-2, pp. 96–100, 2002. DOI: [10.1016/S1386-9477\(02\)00364-8](https://doi.org/10.1016/S1386-9477(02)00364-8).
- [75] D. Y. Kim, E. Guijt, R. A. C. M. M. van Swaaij, and M. Zeman, "Development of a-SiO_x:H solar cells with very high V_{OC}×FF product," *Progress in Photovoltaics: Research and Applications*, vol. 23, no. 6, pp. 671–684, 2015. DOI: [10.1002/pip.2581](https://doi.org/10.1002/pip.2581).
- [76] Y. Hamakawa, H. Okamoto, and Y. Nitta, "A new type of amorphous silicon photovoltaic cell generating more than 2.0 V," *Applied Physics Letters*, vol. 35, no. 2, pp. 187–189, 1979. DOI: [10.1063/1.91031](https://doi.org/10.1063/1.91031).
- [77] J. Yang, R. Ross, R. Mohr, and J. P. Fournier, "High efficiency solar cells using amorphous silicon and amorphous silicon-germanium based alloys," in *1985 IEEE 18th Photovoltaic Specialists Conference (PVSC)*, Las Vegas: IEEE, 1985, pp. 1519–1522.
- [78] J. Meier, S. Dubail, D. Fischer, J. A. Anna Selvan, N. Pellaton Vaucher, R. Platz, C. Hof, R. Flückiger, U. Kroll, N. Wyrsh, P. Torres, H. Keppner, A. Shah, and K.-D. Ufert, "The 'Micromorph' Solar Cells: a New Way to High Efficiency Thin Film Silicon Solar Cells," in *13th EC Photovoltaic Solar Energy Conference*, 1995, pp. 1445–1450.
- [79] H. Sai, K. Maejima, T. Matsui, T. Koida, M. Kondo, S. Nakao, Y. Takeuchi, H. Katayama, and I. Yoshida, "High-efficiency microcrystalline silicon solar cells on honeycomb textured substrates grown with high-rate VHF plasma-enhanced chemical vapor deposition," *Japanese Journal of Applied Physics*, vol. 54, no. 8S1, 08KB05, 2015. DOI: [10.7567/JJAP.54.08KB05](https://doi.org/10.7567/JJAP.54.08KB05).

- [80] B. Yan, G. Yue, L. Sivec, J. Yang, S. Guha, and C.-S. Jiang, "Innovative dual function nc-SiO_x:H layer leading to a >16% efficient multi-junction thin-film silicon solar cell," *Applied Physics Letters*, vol. 99, no. 11, p. 113512, 2011. DOI: [10.1063/1.3638068](https://doi.org/10.1063/1.3638068).
- [81] H. Sai, T. Matsui, and K. Matsubara, "Stabilized 14.0%-efficient triple-junction thin-film silicon solar cell," *Applied Physics Letters*, vol. 109, no. 18, p. 183506, 2016. DOI: [10.1063/1.4966996](https://doi.org/10.1063/1.4966996).
- [82] O. Isabella, A. H. M. Smets, and M. Zeman, "Thin-film silicon-based quadruple junction solar cells approaching 20% conversion efficiency," *Solar Energy Materials and Solar Cells*, vol. 129, pp. 82–89, 2014. DOI: [10.1016/j.solmat.2014.03.021](https://doi.org/10.1016/j.solmat.2014.03.021).
- [83] T. Matsui, C.-W. Chang, K. Mizuno, Y. Takeuchi, and M. Kondo, "Compensation of Native Defect Acceptors in Microcrystalline Ge and Si_{1-x}Ge_x Thin Films by Oxygen Incorporation: Electrical Properties and Solar Cell Performance," *Japanese Journal of Applied Physics*, vol. 51, no. 9R, p. 091302, 2012. DOI: [10.1143/JJAP.51.091302](https://doi.org/10.1143/JJAP.51.091302).
- [84] P. Buehlmann, J. Bailat, D. Dominé, A. Billet, F. Meillaud, A. Feltrin, and C. Ballif, "In situ silicon oxide based intermediate reflector for thin-film silicon micromorph solar cells," *Applied Physics Letters*, vol. 91, no. 14, p. 143505, 2007. DOI: [10.1063/1.2794423](https://doi.org/10.1063/1.2794423).
- [85] P. Cuony, M. Marending, D. T. L. Alexander, M. Boccard, G. Bugnon, M. Despeisse, and C. Ballif, "Mixed-phase p-type silicon oxide containing silicon nanocrystals and its role in thin-film silicon solar cells," *Applied Physics Letters*, vol. 97, no. 21, p. 213502, 2010. DOI: [10.1063/1.3517492](https://doi.org/10.1063/1.3517492).
- [86] P. Delli Veneri, L. V. Mercaldo, and I. Usatii, "Silicon oxide based n-doped layer for improved performance of thin film silicon solar cells," *Applied Physics Letters*, vol. 97, no. 2, p. 023512, 2010. DOI: [10.1063/1.3463457](https://doi.org/10.1063/1.3463457).
- [87] P. Cuony, D. T. L. Alexander, I. Perez-Wurfl, M. Despeisse, G. Bugnon, M. Boccard, T. Söderström, A. Hessler-Wyser, C. Hébert, and C. Ballif, "Silicon Filaments in Silicon Oxide for Next-Generation Photovoltaics," *Advanced Materials*, vol. 24, no. 9, pp. 1182–1186, 2012. DOI: [10.1002/adma.201104578](https://doi.org/10.1002/adma.201104578).
- [88] V. Demontis, C. Sanna, J. Melskens, R. Santbergen, a. H. M. Smets, A. Damiano, and M. Zeman, "The role of oxide interlayers in back reflector configurations for amorphous silicon solar cells," *Journal of Applied Physics*, vol. 113, no. 6, p. 064508, 2013. DOI: [10.1063/1.4790875](https://doi.org/10.1063/1.4790875).
- [89] A. Lambertz, V. Smirnov, T. Merdzhanova, K. Ding, S. Haas, G. Jost, R. Schropp, F. Finger, and U. Rau, "Microcrystalline silicon–oxygen alloys for application in silicon solar cells and modules," *Solar Energy Materials and Solar Cells*, vol. 119, pp. 134–143, 2013. DOI: [10.1016/j.solmat.2013.05.053](https://doi.org/10.1016/j.solmat.2013.05.053).

- [90] H. Tan, E. Moulin, F. T. Si, J.-W. Schüttauf, M. Stuckelberger, O. Isabella, F.-J. Haug, C. Ballif, M. Zeman, and A. H. M. Smets, "Highly transparent modulated surface textured front electrodes for high-efficiency multijunction thin-film silicon solar cells," *Progress in Photovoltaics: Research and Applications*, vol. 23, no. 8, pp. 949–963, 2015. DOI: [10.1002/pip.2639](https://doi.org/10.1002/pip.2639).
- [91] T. Oyama, M. Kambe, N. Taneda, K. Masumo, W.-Y. Kim, A. Shibata, Y. Kazama, M. Konagai, K. Takahashi, H. Iida, T. Mishuku, A. Ito, Y. Hayashi, Y. Hayashi, J. Krc, K. Brecl, F. Smole, M. Topic, M. Mizuhashi, Y. Gotoh, K. Adachi, T. Ikeda, K. Sato, Y. Hayashi, Y. Wakayama, K. Adachi, and H. Nishimura, "Requirements for TCO Substrate in Si-based Thin Film Solar Cells -Toward Tandem," in *MRS Proceedings*, vol. 1101, Cambridge University Press, 2008, KK02–01. DOI: [10.1557/PROC-1101-KK02-01](https://doi.org/10.1557/PROC-1101-KK02-01).
- [92] O. Isabella, F. Moll, J. Krč, and M. Zeman, "Modulated surface textures using zinc-oxide films for solar cells applications," *Physica Status Solidi A*, vol. 207, no. 3, pp. 642–646, 2010. DOI: [10.1002/pssa.200982828](https://doi.org/10.1002/pssa.200982828).
- [93] M. Boccard, C. Battaglia, S. Hänni, K. Söderström, J. Escarré, S. Nicolay, F. Meillaud, M. Despeisse, and C. Ballif, "Multiscale Transparent Electrode Architecture for Efficient Light Management and Carrier Collection in Solar Cells," *Nano Letters*, vol. 12, no. 3, pp. 1344–1348, 2012. DOI: [10.1021/nl203909u](https://doi.org/10.1021/nl203909u).
- [94] G. Yang, R. A. van Swaaij, H. Tan, O. Isabella, and M. Zeman, "Modulated surface textured glass as substrate for high efficiency microcrystalline silicon solar cells," *Solar Energy Materials and Solar Cells*, vol. 133, pp. 156–162, 2015. DOI: [10.1016/j.solmat.2014.11.013](https://doi.org/10.1016/j.solmat.2014.11.013).
- [95] A. Ingenito, O. Isabella, and M. Zeman, "Nano-cones on micro-pyramids: modulated surface textures for maximal spectral response and high-efficiency solar cells," *Progress in Photovoltaics: Research and Applications*, vol. 23, no. 11, pp. 1649–1659, 2015. DOI: [10.1002/pip.2606](https://doi.org/10.1002/pip.2606).
- [96] T. Koida, H. Fujiwara, and M. Kondo, "Hydrogen-doped In_2O_3 as High-mobility Transparent Conductive Oxide," *Japanese Journal of Applied Physics*, vol. 46, no. 28, pp. L685–L687, 2007. DOI: [10.1143/JJAP.46.L685](https://doi.org/10.1143/JJAP.46.L685).
- [97] B. Macco, Y. Wu, D. Vanhemel, and W. M. M. Kessels, "High mobility In_2O_3 :H transparent conductive oxides prepared by atomic layer deposition and solid phase crystallization," *physica status solidi (RRL) - Rapid Research Letters*, vol. 8, no. 12, pp. 987–990, 2014. DOI: [10.1002/pssr.201409426](https://doi.org/10.1002/pssr.201409426).
- [98] F. T. Si, D. Y. Kim, R. Santbergen, H. Tan, R. A. C. M. M. van Swaaij, A. H. M. Smets, O. Isabella, and M. Zeman, "Quadruple-junction thin-film silicon-based solar cells with high open-circuit voltage," *Applied Physics Letters*, vol. 105, no. 6, p. 063902, 2014. DOI: [10.1063/1.4892890](https://doi.org/10.1063/1.4892890).
- [99] A. De Vos, "Detailed balance limit of the efficiency of tandem solar cells," *Journal of Physics D: Applied Physics*, vol. 13, no. 5, pp. 839–846, 1980. DOI: [10.1088/0022-3727/13/5/018](https://doi.org/10.1088/0022-3727/13/5/018).

- [100] H. Sai, T. Koida, T. Matsui, I. Yoshida, K. Saito, and M. Kondo, "Microcrystalline Silicon Solar Cells with 10.5% Efficiency Realized by Improved Photon Absorption via Periodic Textures and Highly Transparent Conductive Oxide," *Applied Physics Express*, vol. 6, no. 10, p. 104 101, 2013. DOI: [10.7567/APEX.6.104101](https://doi.org/10.7567/APEX.6.104101).
- [101] H. Sai, T. Matsui, M. Kondo, and I. Yoshida, "Improved Light-In-Coupling via Anti-Reflection Films in Thin Film Microcrystalline Silicon Solar Cells on Honeycomb-Patterned Substrates," in *2014 IEEE 40th Photovoltaic Specialists Conference (PVSC)*, Denver: IEEE, 2014.
- [102] M. Boccard, M. Despeisse, J. Escarre, X. Niquille, G. Bugnon, S. Hänni, M. Bonnet-Eymard, F. Meillaud, and C. Ballif, "Low-refractive-index silicon-oxide interlayers for high-stable-efficiency multi-junction thin-film silicon solar cells," in *2014 IEEE 40th Photovoltaic Specialists Conference (PVSC)*, Denver: IEEE, 2014.
- [103] M. Boccard, M. Despeisse, J. Escarre, X. Niquille, G. Bugnon, S. Hanni, M. Bonnet-Eymard, F. Meillaud, and C. Ballif, "High-Stable-Efficiency Tandem Thin-Film Silicon Solar Cell With Low-Refractive-Index Silicon-Oxide Interlayer," *IEEE Journal of Photovoltaics*, vol. 4, no. 6, pp. 1368–1373, 2014. DOI: [10.1109/JPHOTOV.2014.2357495](https://doi.org/10.1109/JPHOTOV.2014.2357495).
- [104] S. Kim, J.-W. Chung, H. Lee, J. Park, Y. Heo, and H.-M. Lee, "Remarkable progress in thin-film silicon solar cells using high-efficiency triple-junction technology," *Solar Energy Materials and Solar Cells*, vol. 119, pp. 26–35, 2013. DOI: [10.1016/j.solmat.2013.04.016](https://doi.org/10.1016/j.solmat.2013.04.016).
- [105] M. Meusel, R. Adelhelm, F. Dimroth, A. Bett, and W. Warta, "Spectral mismatch correction and spectrometric characterization of monolithic III-V multi-junction solar cells," *Progress in Photovoltaics: Research and Applications*, vol. 10, no. 4, pp. 243–255, 2002. DOI: [10.1002/pip.407](https://doi.org/10.1002/pip.407).
- [106] M. Zeman, O. Isabella, S. Solntsev, and K. Jäger, "Modelling of thin-film silicon solar cells," *Solar Energy Materials and Solar Cells*, vol. 119, pp. 94–111, 2013. DOI: [10.1016/j.solmat.2013.05.037](https://doi.org/10.1016/j.solmat.2013.05.037).
- [107] R. Santbergen, T. Meguro, T. Suezaki, G. Koizumi, K. Yamamoto, and M. Zeman, "GenPro4 Optical Model for Solar Cell Simulation and Its Application to Multijunction Solar Cells," *IEEE Journal of Photovoltaics*, vol. 7, no. 3, pp. 919–926, 2017. DOI: [10.1109/JPHOTOV.2017.2669640](https://doi.org/10.1109/JPHOTOV.2017.2669640).
- [108] M. Sever, B. Lipovšek, J. Krč, A. Čampa, G. Sánchez Plaza, F.-J. Haug, M. Duchamp, W. Soppe, and M. Topič, "Combined model of non-conformal layer growth for accurate optical simulation of thin-film silicon solar cells," *Solar Energy Materials and Solar Cells*, vol. 119, pp. 59–66, 2013. DOI: [10.1016/j.solmat.2013.05.016](https://doi.org/10.1016/j.solmat.2013.05.016).
- [109] A. Lambertz, T. Grundler, and F. Finger, "Hydrogenated amorphous silicon oxide containing a microcrystalline silicon phase and usage as an intermediate reflector in thin-film silicon solar cells," *Journal of Applied Physics*, vol. 109, no. 11, p. 113 109, 2011. DOI: [10.1063/1.3592208](https://doi.org/10.1063/1.3592208).

- [110] T. Koida, H. Fujiwara, and M. Kondo, "Reduction of Optical Loss in Hydrogenated Amorphous Silicon/Crystalline Silicon Heterojunction Solar Cells by High-Mobility Hydrogen-Doped In_2O_3 Transparent Conductive Oxide," *Applied Physics Express*, vol. 1, no. 4, p. 041501, 2008. DOI: [10.1143/APEX.1.041501](https://doi.org/10.1143/APEX.1.041501).
- [111] F. T. Si, O. Isabella, and M. Zeman, "Artifact Interpretation of Spectral Response Measurements on Two-Terminal Multijunction Solar Cells," *Advanced Energy Materials*, vol. 7, no. 6, p. 1601930, 2017. DOI: [10.1002/aenm.201601930](https://doi.org/10.1002/aenm.201601930).
- [112] P. Chiu, D. Law, R. Woo, S. Singer, D. Bhusari, W. Hong, A. Zakaria, J. Boisvert, S. Mesropian, R. King, and N. Karam, "35.8% space and 38.8% terrestrial 5J direct bonded cells," in *2014 IEEE 40th Photovoltaic Specialist Conference (PVSC)*, IEEE, 2014, pp. 0011–0013. DOI: [10.1109/PVSC.2014.6924957](https://doi.org/10.1109/PVSC.2014.6924957).
- [113] H. Sai, T. Matsui, T. Koida, K. Matsubara, M. Kondo, S. Sugiyama, H. Katayama, Y. Takeuchi, and I. Yoshida, "Triple-junction thin-film silicon solar cell fabricated on periodically textured substrate with a stabilized efficiency of 13.6%," *Applied Physics Letters*, vol. 106, no. 21, p. 213902, 2015. DOI: [10.1063/1.4921794](https://doi.org/10.1063/1.4921794).
- [114] M. A. Green, K. Emery, Y. Hishikawa, W. Warta, and E. D. Dunlop, "Solar cell efficiency tables (version 48)," *Progress in Photovoltaics: Research and Applications*, vol. 24, no. 7, pp. 905–913, 2016. DOI: [10.1002/pip.2788](https://doi.org/10.1002/pip.2788).
- [115] J. Burdick and T. Glatfelter, "Spectral response and I–V measurements of tandem amorphous-silicon alloy solar cells," *Solar Cells*, vol. 18, no. 3-4, pp. 301–314, 1986. DOI: [10.1016/0379-6787\(86\)90129-8](https://doi.org/10.1016/0379-6787(86)90129-8).
- [116] M. Meusel, C. Baur, G. Létay, A. Bett, W. Warta, and E. Fernandez, "Spectral response measurements of monolithic GaInP/Ga(In)As/Ge triple-junction solar cells: Measurement artifacts and their explanation," *Progress in Photovoltaics: Research and Applications*, vol. 11, no. 8, pp. 499–514, 2003. DOI: [10.1002/pip.514](https://doi.org/10.1002/pip.514).
- [117] M. Pravettoni, R. Galleano, A. Virtuani, H. Müllejans, and E. D. Dunlop, "Spectral response measurement of double-junction thin-film photovoltaic devices: the impact of shunt resistance and bias voltage," *Measurement Science and Technology*, vol. 22, no. 4, p. 045902, 2011. DOI: [10.1088/0957-0233/22/4/045902](https://doi.org/10.1088/0957-0233/22/4/045902).
- [118] J.-J. Li, S. H. Lim, C. R. Allen, D. Ding, and Y.-H. Zhang, "Combined Effects of Shunt and Luminescence Coupling on External Quantum Efficiency Measurements of Multijunction Solar Cells," *IEEE Journal of Photovoltaics*, vol. 1, no. 2, pp. 225–230, 2011. DOI: [10.1109/JPHOTOV.2011.2172188](https://doi.org/10.1109/JPHOTOV.2011.2172188).
- [119] V. Paraskeva, M. Hadjipanayi, M. Norton, M. Pravettoni, and G. E. Georgiou, "Voltage and light bias dependent quantum efficiency measurements of GaInP/GaInAs/Ge triple junction devices," *Solar Energy Materials and Solar Cells*, vol. 116, pp. 55–60, 2013. DOI: [10.1016/j.solmat.2013.04.010](https://doi.org/10.1016/j.solmat.2013.04.010).

- [120] D. Bahro, M. Koppitz, A. Mertens, K. Glaser, J. Mescher, and A. Colmann, "Understanding the External Quantum Efficiency of Organic Homo-Tandem Solar Cells Utilizing a Three-Terminal Device Architecture," *Advanced Energy Materials*, vol. 5, no. 22, p. 1501019, 2015. DOI: [10.1002/aenm.201501019](https://doi.org/10.1002/aenm.201501019).
- [121] C. Hibberd, F. Plyta, C. Monokroussos, M. Bliss, T. Betts, and R. Gottschalg, "Voltage-dependent quantum efficiency measurements of amorphous silicon multi-junction mini-modules," *Solar Energy Materials and Solar Cells*, vol. 95, no. 1, pp. 123–126, 2011. DOI: [10.1016/j.solmat.2010.03.039](https://doi.org/10.1016/j.solmat.2010.03.039).
- [122] T. Sogabe, A. Ogura, and Y. Okada, "Analysis of bias voltage dependent spectral response in Ga_{0.51}In_{0.49}P/Ga_{0.99}In_{0.01}As/Ge triple junction solar cell," *Journal of Applied Physics*, vol. 115, no. 7, p. 074503, 2014. DOI: [10.1063/1.4866321](https://doi.org/10.1063/1.4866321).
- [123] E. Barrigón, P. Espinet-González, Y. Contreras, and I. Rey-Stolle, "Implications of low breakdown voltage of component subcells on external quantum efficiency measurements of multijunction solar cells," *Progress in Photovoltaics: Research and Applications*, vol. 23, no. 11, pp. 1597–1607, 2015. DOI: [10.1002/pip.2597](https://doi.org/10.1002/pip.2597).
- [124] R. Timmreck, T. Meyer, J. Gilot, H. Seifert, T. Mueller, A. Furlan, M. M. Wienk, D. Wynands, J. Hohl-Ebinger, W. Warta, R. A. J. Janssen, M. Riede, and K. Leo, "Characterization of tandem organic solar cells," *Nature Photonics*, vol. 9, no. 8, pp. 478–479, 2015. DOI: [10.1038/nphoton.2015.124](https://doi.org/10.1038/nphoton.2015.124).
- [125] *Standard Test Methods for Measurement of Electrical Performance and Spectral Response of Nonconcentrator Multijunction Photovoltaic Cells and Modules*, Standard, 2015.
- [126] J.-W. Schüttauf, G. Bugnon, M. Stuckelberger, S. Hänni, M. Boccard, M. Despeisse, F.-J. Haug, F. Meillaud, and C. Ballif, "Thin-Film Silicon Triple-Junction Solar Cells on Highly Transparent Front Electrodes With Stabilized Efficiencies up to 12.8%," *IEEE Journal of Photovoltaics*, vol. 4, no. 3, pp. 757–762, 2014. DOI: [10.1109/JPHOTOV.2014.2307162](https://doi.org/10.1109/JPHOTOV.2014.2307162).
- [127] J.-W. Schüttauf, B. Niesen, L. Löfgren, M. Bonnet-Eymard, M. Stuckelberger, S. Hänni, M. Boccard, G. Bugnon, M. Despeisse, F.-J. Haug, F. Meillaud, and C. Ballif, "Amorphous silicon–germanium for triple and quadruple junction thin-film silicon based solar cells," *Solar Energy Materials and Solar Cells*, vol. 133, pp. 163–169, 2015. DOI: [10.1016/j.solmat.2014.11.006](https://doi.org/10.1016/j.solmat.2014.11.006).
- [128] S. Kirner, S. Neubert, C. Schultz, O. Gabriel, B. Stannowski, B. Rech, and R. Schlatmann, "Quadruple-junction solar cells and modules based on amorphous and microcrystalline silicon with high stable efficiencies," *Japanese Journal of Applied Physics*, vol. 54, no. 8S1, 08KB03, 2015. DOI: [10.7567/JJAP.54.08KB03](https://doi.org/10.7567/JJAP.54.08KB03).
- [129] J. P. Mailoa, C. D. Bailie, E. C. Johlin, E. T. Hoke, A. J. Akey, W. H. Nguyen, M. D. McGehee, and T. Buonassisi, "A 2-terminal perovskite/silicon multijunction solar cell enabled by a silicon tunnel junction," *Applied Physics Letters*, vol. 106, no. 12, p. 121105, 2015. DOI: [10.1063/1.4914179](https://doi.org/10.1063/1.4914179).

- [130] S. Albrecht, M. Saliba, J. P. Correa Baena, F. Lang, L. Kegelmann, M. Mews, L. Steier, A. Abate, J. Rappich, L. Korte, R. Schlattmann, M. K. Nazeeruddin, A. Hagfeldt, M. Grätzel, and B. Rech, "Monolithic Perovskite/Silicon-Heterojunction Tandem Solar Cells Processed at Low Temperature," *Energy & Environmental Science*, vol. 9, no. 1, pp. 81–88, 2016. DOI: [10.1039/C5EE02965A](https://doi.org/10.1039/C5EE02965A).
- [131] J. Werner, C.-H. Weng, A. Walter, L. Fesquet, J. P. Seif, S. De Wolf, B. Niesen, and C. Ballif, "Efficient Monolithic Perovskite/Silicon Tandem Solar Cell With Cell Area $>1 \text{ cm}^2$," *The Journal of Physical Chemistry Letters*, vol. 7, no. 1, pp. 161–166, 2016. DOI: [10.1021/acs.jpcllett.5b02686](https://doi.org/10.1021/acs.jpcllett.5b02686).
- [132] T. Todorov, T. Gershon, O. Gunawan, Y. S. Lee, C. Sturdevant, L.-Y. Chang, and S. Guha, "Monolithic Perovskite-CIGS Tandem Solar Cells via In Situ Band Gap Engineering," *Advanced Energy Materials*, vol. 5, no. 23, p. 1500799, 2015. DOI: [10.1002/aenm.201500799](https://doi.org/10.1002/aenm.201500799).
- [133] C. D. Bailie, M. G. Christoforo, J. P. Mailoa, A. R. Bowring, E. L. Unger, W. H. Nguyen, J. Burschka, N. Pellet, J. Z. Lee, M. Grätzel, R. Noufi, T. Buonassisi, A. Salleo, and M. D. McGehee, "Semi-transparent perovskite solar cells for tandems with silicon and CIGS," *Energy & Environmental Science*, vol. 8, no. 3, pp. 956–963, 2015. DOI: [10.1039/C4EE03322A](https://doi.org/10.1039/C4EE03322A).
- [134] H. Tan, A. Furlan, W. Li, K. Arapov, R. Santbergen, M. M. Wienk, M. Zeman, A. H. M. Smets, and R. A. J. Janssen, "Highly Efficient Hybrid Polymer and Amorphous Silicon Multijunction Solar Cells with Effective Optical Management.," *Advanced Materials*, vol. 28, no. 11, pp. 2170–2177, 2016. DOI: [10.1002/adma.201504483](https://doi.org/10.1002/adma.201504483).
- [135] D. Abou-Ras, T. Kirchartz, and U. Rau, Eds., *Advanced Characterization Techniques for Thin Film Solar Cells*, 1st. Wiley-VCH, 2011, p. 585. DOI: [10.1002/9783527636280](https://doi.org/10.1002/9783527636280).
- [136] *Standard Test Method for Spectral Responsivity Measurements of Photovoltaic Devices*, Standard.
- [137] D. Bahro, M. Koppitz, and A. Colsmann, "Tandem organic solar cells revisited," *Nature Photonics*, vol. 10, pp. 354–355, 2016. DOI: [10.1038/nphoton.2016.96](https://doi.org/10.1038/nphoton.2016.96).
- [138] R. Timmreck, T. Meyer, J. Gilot, H. Seifert, T. Mueller, A. Furlan, M. M. Wienk, D. Wynands, J. Hohl-Ebinger, W. Warta, R. A. J. Janssen, M. Riede, and K. Leo, "Reply to 'Tandem organic solar cells revisited'," *Nature Photonics*, vol. 10, p. 355, 2016. DOI: [10.1038/nphoton.2016.99](https://doi.org/10.1038/nphoton.2016.99).
- [139] J. Merten, J. Asensi, C. Voz, A. Shah, R. Platz, and J. Andreu, "Improved equivalent circuit and analytical model for amorphous silicon solar cells and modules," *IEEE Transactions on Electron Devices*, vol. 45, no. 2, pp. 423–429, 1998. DOI: [10.1109/16.658676](https://doi.org/10.1109/16.658676).
- [140] S. S. Hegedus and W. N. Shafarman, "Thin-film solar cells: device measurements and analysis," *Progress in Photovoltaics: Research and Applications*, vol. 12, no. 23, pp. 155–176, 2004. DOI: [10.1002/pip.518](https://doi.org/10.1002/pip.518).

- [141] R. Timmreck, K. Leo, and M. Riede, "Characterization of tandem organic solar cells comprising subcells of identical absorber material," *Progress in Photovoltaics: Research and Applications*, vol. 23, no. 10, pp. 1353–1356, 2015. DOI: [10.1002/pip.2541](https://doi.org/10.1002/pip.2541).
- [142] K. Söderström, G. Bugnon, R. Biron, C. Pahud, F. Meillaud, F.-J. Haug, and C. Ballif, "Thin-film silicon triple-junction solar cell with 12.5% stable efficiency on innovative flat light-scattering substrate," *Journal of Applied Physics*, vol. 112, no. 11, p. 114503, 2012. DOI: [10.1063/1.4768272](https://doi.org/10.1063/1.4768272).
- [143] J. Gilot, M. M. Wienk, and R. A. J. Janssen, "Measuring the External Quantum Efficiency of Two-Terminal Polymer Tandem Solar Cells," *Advanced Functional Materials*, vol. 20, no. 22, pp. 3904–3911, 2010. DOI: [10.1002/adfm.201001167](https://doi.org/10.1002/adfm.201001167).
- [144] L. J. A. Koster, M. Kemerink, M. M. Wienk, K. Maturová, and R. A. J. Janssen, "Quantifying Bimolecular Recombination Losses in Organic Bulk Heterojunction Solar Cells," *Advanced Materials*, vol. 23, no. 14, pp. 1670–1674, 2011. DOI: [10.1002/adma.201004311](https://doi.org/10.1002/adma.201004311).
- [145] W. Tress, K. Leo, and M. Riede, "Photoconductivity as loss mechanism in organic solar cells," *physica status solidi (RRL) - Rapid Research Letters*, vol. 7, no. 6, pp. 401–405, 2013. DOI: [10.1002/pssr.201307039](https://doi.org/10.1002/pssr.201307039).
- [146] S. H. Lim, J.-J. Li, E. H. Steenbergen, and Y.-H. Zhang, "Luminescence coupling effects on multijunction solar cell external quantum efficiency measurement," *Progress in Photovoltaics: Research and Applications*, vol. 21, no. 3, pp. 344–350, 2013. DOI: [10.1002/pip.1215](https://doi.org/10.1002/pip.1215).
- [147] F. T. Si, O. Isabella, and M. Zeman, "Thin-film amorphous silicon germanium solar cells with p- and n-type hydrogenated silicon oxide layers," *Solar Energy Materials and Solar Cells*, vol. 163, pp. 9–14, 2017. DOI: [10.1016/j.solmat.2017.01.001](https://doi.org/10.1016/j.solmat.2017.01.001).
- [148] S. Guha, J. Payson, S. Agarwal, and S. Ovshinsky, "Fluorinated amorphous silicon-germanium alloys deposited from disilane-germane mixture," *Journal of Non-Crystalline Solids*, vol. 97-98, pp. 1455–1458, 1987. DOI: [10.1016/0022-3093\(87\)90349-8](https://doi.org/10.1016/0022-3093(87)90349-8).
- [149] M. Stutzmann, R. A. Street, C. C. Tsai, J. B. Boyce, and S. E. Ready, "Structural, optical, and spin properties of hydrogenated amorphous silicon-germanium alloys," *Journal of Applied Physics*, vol. 66, no. 2, p. 569, 1989. DOI: [10.1063/1.343574](https://doi.org/10.1063/1.343574).
- [150] J. Yang, A. Banerjee, and S. Guha, "Triple-junction amorphous silicon alloy solar cell with 14.6% initial and 13.0% stable conversion efficiencies," *Applied Physics Letters*, vol. 70, no. 22, p. 2975, 1997. DOI: [10.1063/1.118761](https://doi.org/10.1063/1.118761).
- [151] D. J. You, S. H. Kim, H. Lee, J.-W. Chung, S.-T. Hwang, Y. H. Heo, S. Lee, and H.-M. Lee, "Recent progress of high efficiency Si thin-film solar cells in large area," *Progress in Photovoltaics: Research and Applications*, vol. 23, no. 8, pp. 973–988, 2015. DOI: [10.1002/pip.2510](https://doi.org/10.1002/pip.2510).

- [152] P. Sicanugrist, T. Yoshida, Y. Ichikawa, and H. Sakai, "Amorphous silicon oxide with microcrystalline Si phase," *Journal of Non-Crystalline Solids*, vol. 164-166, pp. 1081–1084, 1993. DOI: [10.1016/0022-3093\(93\)91186-7](https://doi.org/10.1016/0022-3093(93)91186-7).
- [153] P. Sicanugrist, T. Sasaki, A. Asano, Y. Ichikawa, and H. Sakai, "Amorphous silicon oxide and its application to metal/n-i-p/ITO type a-Si solar cells," *Solar Energy Materials and Solar Cells*, vol. 34, no. 1-4, pp. 415–422, 1994. DOI: [10.1016/0927-0248\(94\)90068-X](https://doi.org/10.1016/0927-0248(94)90068-X).
- [154] R. Biron, C. Pahud, F.-J. Haug, J. Escarré, K. Söderström, and C. Ballif, "Window layer with p doped silicon oxide for high Voc thin-film silicon n-i-p solar cells," *Journal of Applied Physics*, vol. 110, no. 12, p. 124511, 2011. DOI: [10.1063/1.3669389](https://doi.org/10.1063/1.3669389).
- [155] L. V. Mercaldo, P. Delli Veneri, I. Usatii, E. M. Esposito, and G. Nicotra, "Properties of mixed phase n-doped silicon oxide layers and application in microcrystalline solar cells," *Solar Energy Materials and Solar Cells*, vol. 119, pp. 67–72, 2013. DOI: [10.1016/j.solmat.2013.05.030](https://doi.org/10.1016/j.solmat.2013.05.030).
- [156] H. Tan, P. Babal, M. Zeman, and A. H. Smets, "Wide bandgap p-type nanocrystalline silicon oxide as window layer for high performance thin-film silicon multi-junction solar cells," *Solar Energy Materials and Solar Cells*, vol. 132, pp. 597–605, 2015. DOI: [10.1016/j.solmat.2014.10.020](https://doi.org/10.1016/j.solmat.2014.10.020).
- [157] B. Liu, L. Bai, X. Zhang, C. Wei, Q. Huang, J. Sun, H. Ren, G. Hou, and Y. Zhao, "Fill factor improvement in PIN type hydrogenated amorphous silicon germanium thin film solar cells: Omnipotent N type $\mu\text{c-SiOx:H}$ layer," *Solar Energy Materials and Solar Cells*, vol. 140, pp. 450–456, 2015. DOI: [10.1016/j.solmat.2015.05.008](https://doi.org/10.1016/j.solmat.2015.05.008).
- [158] Asahi Glass Company, *VU (TCO), TCO Coated glass for thin film application (a-Si/ $\mu\text{c-Si}$)*.
- [159] M. Kubon, E. Boehmer, F. Siebke, B. Rech, C. Beneking, and H. Wagner, "Solution of the ZnO/p contact problem in a-Si:H solar cells," *Solar Energy Materials and Solar Cells*, vol. 41-42, pp. 485–492, 1996. DOI: [10.1016/0927-0248\(95\)00126-3](https://doi.org/10.1016/0927-0248(95)00126-3).
- [160] S. Guha, J. Yang, A. Pawlikiewicz, T. Glatfelter, R. Ross, and S. R. Ovshinsky, "Band-gap profiling for improving the efficiency of amorphous silicon alloy solar cells," *Applied Physics Letters*, vol. 54, no. 23, p. 2330, 1989. DOI: [10.1063/1.101118](https://doi.org/10.1063/1.101118).
- [161] R. Jimenez Zambrano, F. Rubinelli, J. Rath, and R. Schropp, "Improvement in the spectral response at long wavelength of a-SiGe:H solar cells by exponential band gap design of the i-layer," *Journal of Non-Crystalline Solids*, vol. 299-302, pp. 1131–1135, 2002. DOI: [10.1016/S0022-3093\(01\)01080-8](https://doi.org/10.1016/S0022-3093(01)01080-8).
- [162] B. Pieters, M. Zeman, R. van Swaaij, and W. Metselaar, "Optimization of a-SiGe:H solar cells with graded intrinsic layers using integrated optical and electrical modeling," *Thin Solid Films*, vol. 451-452, pp. 294–297, 2004. DOI: [10.1016/j.tsf.2003.11.029](https://doi.org/10.1016/j.tsf.2003.11.029).

- [163] J.-W. Chung, J. W. Park, Y. J. Lee, S.-W. Ahn, H.-M. Lee, and O. O. Park, "Graded Layer Modification for High Efficiency Hydrogenated Amorphous Silicon–Germanium Solar Cells," *Japanese Journal of Applied Physics*, vol. 51, no. 10S, 10NB16, 2012. DOI: [10.1143/JJAP.51.10NB16](https://doi.org/10.1143/JJAP.51.10NB16).
- [164] G. E. Jellison and F. A. Modine, "Parameterization of the optical functions of amorphous materials in the interband region," *Applied Physics Letters*, vol. 69, no. 3, p. 371, 1996. DOI: [10.1063/1.118064](https://doi.org/10.1063/1.118064).
- [165] —, "Erratum: "Parameterization of the optical functions of amorphous materials in the interband region" [Appl. Phys. Lett. 69, 371 (1996)]," *Applied Physics Letters*, vol. 69, no. 14, p. 2137, 1996. DOI: [10.1063/1.118155](https://doi.org/10.1063/1.118155).
- [166] J. Fang, L. Bai, T. Li, G. Hou, B. Li, C. Wei, G. Wang, D. Zhang, Y. Zhao, and X. Zhang, "High-efficiency micromorph solar cell with light management in tunnel recombination junction," *Solar Energy Materials and Solar Cells*, vol. 155, pp. 469–473, 2016. DOI: [10.1016/j.solmat.2016.06.052](https://doi.org/10.1016/j.solmat.2016.06.052).
- [167] J. Sap, O. Isabella, K. Jäger, and M. Zeman, "Extraction of optical properties of flat and surface-textured transparent conductive oxide films in a broad wavelength range," *Thin Solid Films*, vol. 520, no. 3, pp. 1096–1101, 2011. DOI: [10.1016/j.tsf.2011.08.023](https://doi.org/10.1016/j.tsf.2011.08.023).
- [168] D. Dominé, "The role of front electrodes and intermediate reflectors in the optoelectronic properties of high-efficiency micromorph solar cells," PhD thesis, Université de Neuchâtel, 2009, p. 179.
- [169] F. T. Si, O. Isabella, H. Tan, and M. Zeman, "Quadruple-Junction Thin-Film Silicon Solar Cells Using Four Different Absorber Materials," *Solar RRL*, p. 1700036, 2017. DOI: [10.1002/solr.201700036](https://doi.org/10.1002/solr.201700036).
- [170] T. Matsui, A. Bidiville, K. Maejima, H. Sai, T. Koida, T. Suezaki, M. Matsumoto, K. Saito, I. Yoshida, and M. Kondo, "High-efficiency amorphous silicon solar cells: Impact of deposition rate on metastability," *Applied Physics Letters*, vol. 106, no. 5, p. 053901, 2015. DOI: [10.1063/1.4907001](https://doi.org/10.1063/1.4907001).
- [171] F. Urbain, V. Smirnov, J.-P. Becker, A. Lambertz, F. Yang, J. Ziegler, B. Kaiser, W. Jaegermann, U. Rau, and F. Finger, "Multijunction Si photocathodes with tunable photovoltages from 2.0 V to 2.8 V for light induced water splitting," *Energy & Environmental Science*, vol. 9, no. 1, pp. 145–154, 2016. DOI: [10.1039/C5EE02393A](https://doi.org/10.1039/C5EE02393A).
- [172] F. Urbain, V. Smirnov, J.-P. Becker, A. Lambertz, U. Rau, and F. Finger, "Light-induced degradation of adapted quadruple junction thin film silicon solar cells for photoelectrochemical water splitting," *Solar Energy Materials and Solar Cells*, vol. 145, pp. 142–147, 2016. DOI: [10.1016/j.solmat.2015.07.033](https://doi.org/10.1016/j.solmat.2015.07.033).
- [173] V. Smirnov, F. Urbain, A. Lambertz, and F. Finger, "High Stabilized Efficiency Single and Multi-junction Thin Film Silicon Solar Cells," *Energy Procedia*, vol. 102, pp. 64–69, 2016. DOI: [10.1016/j.egypro.2016.11.319](https://doi.org/10.1016/j.egypro.2016.11.319).

- [174] F. T. Si, O. Isabella, and M. Zeman, "Strategies towards high-efficiency quadruple-junction thin-film silicon-based solar cells," in *26th International Photovoltaic Science and Engineering Conference (PVSEC-26)*, Singapore, 2016.
- [175] X. Zhang, "Effective Methods for Performance Promotion of Silicon-based Thin Film Solar Cells," in *OSA Light, Energy and the Environment Congress, Optical Nanostructures and Advanced Materials for Photovoltaics (PV)*, Leipzig, Germany, 2016.
- [176] R. Santbergen and R. van Zolingen, "The absorption factor of crystalline silicon PV cells: A numerical and experimental study," *Solar Energy Materials and Solar Cells*, vol. 92, no. 4, pp. 432–444, 2008. DOI: [10.1016/j.solmat.2007.10.005](https://doi.org/10.1016/j.solmat.2007.10.005).
- [177] M. Fischer, H. Tan, J. Melskens, R. Vasudevan, M. Zeman, and A. H. M. Smets, "High pressure processing of hydrogenated amorphous silicon solar cells: Relation between nanostructure and high open-circuit voltage," *Applied Physics Letters*, vol. 106, no. 4, p. 043905, 2015. DOI: [10.1063/1.4907316](https://doi.org/10.1063/1.4907316).
- [178] B. Liu, L. Bai, Z. Chen, X. Zhang, D. Zhang, J. Ni, Q. Huang, C. Wei, J. Sun, X. Chen, H. Ren, G. Hou, G. Wang, and Y. Zhao, "High efficiency triple junction thin film silicon solar cells with optimized electrical structure," *Progress in Photovoltaics: Research and Applications*, vol. 23, no. 10, pp. 1313–1322, 2015. DOI: [10.1002/pip.2564](https://doi.org/10.1002/pip.2564).
- [179] F. T. Si, O. Isabella, and M. Zeman, "Too Many Junctions? A Case Study of Multijunction Thin-Film Silicon Solar Cells," *Advanced Sustainable Systems*, vol. 1, no. 10, p. 1700077, 2017. DOI: [10.1002/adisu.201700077](https://doi.org/10.1002/adisu.201700077).
- [180] H. Cotal, C. Fetzer, J. Boisvert, G. Kinsey, R. King, P. Hebert, H. Yoon, and N. Karam, "III–V multijunction solar cells for concentrating photovoltaics," *Energy & Environmental Science*, vol. 2, no. 2, pp. 174–192, 2009. DOI: [10.1039/B809257E](https://doi.org/10.1039/B809257E).
- [181] D. Friedman, "Progress and challenges for next-generation high-efficiency multijunction solar cells," *Current Opinion in Solid State and Materials Science*, vol. 14, no. 6, pp. 131–138, 2010. DOI: [10.1016/j.cossms.2010.07.001](https://doi.org/10.1016/j.cossms.2010.07.001).
- [182] J. Ohlmann, J. F. M. Sanchez, D. Lackner, P. Förster, M. Steiner, A. Fallisch, and F. Dimroth, "Recent development in direct generation of hydrogen using multi-junction solar cells," in *AIP Conference Proceedings*, 2016, p. 080004. DOI: [10.1063/1.4962102](https://doi.org/10.1063/1.4962102).
- [183] *Sharp Develops Concentrator Solar Cell with World's Highest Conversion Efficiency of 44.4%*, 2013.
- [184] F. Dimroth, T. N. D. Tibbits, M. Niemeyer, F. Predan, P. Beutel, C. Karcher, E. Oliva, G. Siefert, D. Lackner, P. Fus-Kailuweit, A. W. Bett, R. Krause, C. Drazek, E. Guiot, J. Wasselin, A. Tauzin, and T. Signamarcheix, "Four-Junction Wafer-Bonded Concentrator Solar Cells," *IEEE Journal of Photovoltaics*, vol. 6, no. 1, pp. 343–349, 2016. DOI: [10.1109/JPHOTOV.2015.2501729](https://doi.org/10.1109/JPHOTOV.2015.2501729).

- [185] M. A. Green, K. Emery, Y. Hishikawa, W. Warta, E. D. Dunlop, D. H. Levi, and A. W. Y. Ho-Baillie, "Solar cell efficiency tables (version 49)," *Progress in Photovoltaics: Research and Applications*, vol. 25, no. 1, pp. 3–13, 2017. DOI: [10.1002/pip.2855](https://doi.org/10.1002/pip.2855).
- [186] X. Multone, L. Fesquet, D. Borrello, D. Romang, G. Choong, E. Vallat-Sauvain, M. Charrière, A. Billet, J.-F. Boucher, J. Steinhäuser, J.-B. Orhan, R. Monnard, J.-P. Cardoso, G. Charitat, B. Dehbozorgi, N. Guillot, G. Monteduro, M. Marmelo, R. Semenzi, S. Benagli, and J. Meier, "Triple-junction amorphous/microcrystalline silicon solar cells: Towards industrially viable thin film solar technology," *Solar Energy Materials and Solar Cells*, vol. 140, pp. 388–395, 2015. DOI: [10.1016/j.solmat.2015.04.038](https://doi.org/10.1016/j.solmat.2015.04.038).
- [187] M. Stuckelberger, R. Biron, N. Wyrsh, F.-J. Haug, and C. Ballif, "Review: Progress in solar cells from hydrogenated amorphous silicon," *Renewable and Sustainable Energy Reviews*, vol. 76, pp. 1497–1523, 2017. DOI: [10.1016/j.rser.2016.11.190](https://doi.org/10.1016/j.rser.2016.11.190).
- [188] T. Ameri, G. Dennler, C. Lungenschmied, C. J. Brabec, D. Waller, R. Gaudiana, C. J. Brabec, A. J. Heeger, P. W. M. Blom, M. Koch, K. Leo, M. Pfeiffer, H. Hoppe, D. Meissner, N. S. Sariciftci, I. Riedel, V. Dyakonov, and J. Parisi, "Organic tandem solar cells: A review," *Energy & Environmental Science*, vol. 2, no. 4, p. 347, 2009. DOI: [10.1039/b817952b](https://doi.org/10.1039/b817952b).
- [189] T. Ameri, N. Li, and C. J. Brabec, "Highly efficient organic tandem solar cells: a follow up review," *Energy & Environmental Science*, vol. 6, no. 8, p. 2390, 2013. DOI: [10.1039/c3ee40388b](https://doi.org/10.1039/c3ee40388b).
- [190] J. You, L. Dou, Z. Hong, G. Li, and Y. Yang, "Recent trends in polymer tandem solar cells research," *Progress in Polymer Science*, vol. 38, no. 12, pp. 1909–1928, 2013. DOI: [10.1016/j.progpolymsci.2013.04.005](https://doi.org/10.1016/j.progpolymsci.2013.04.005).
- [191] K. A. Bush, A. F. Palmstrom, Z. J. Yu, M. Boccard, R. Cheacharoen, J. P. Mailoa, D. P. McMeekin, R. L. Z. Hoyer, C. D. Bailie, T. Leijtens, I. M. Peters, M. C. Minichetti, N. Rolston, R. Prasanna, S. Sofia, D. Harwood, W. Ma, F. Moghadam, H. J. Snaith, T. Buonassisi, Z. C. Holman, S. F. Bent, and M. D. McGehee, "23.6%-efficient monolithic perovskite/silicon tandem solar cells with improved stability," *Nature Energy*, vol. 2, no. 4, p. 17009, 2017. DOI: [10.1038/nenergy.2017.9](https://doi.org/10.1038/nenergy.2017.9).
- [192] B. Liu, L. Bai, T. Li, C. Wei, B. Li, Q. Huang, D. Zhang, G. Wang, Y. Zhao, and X. Zhang, "High Efficiency and High Open Circuit Voltage Quadruple-Junction Silicon Thin Film Solar Cells for Tomorrow's Electronic Applications," *Energy & Environmental Science*, 2017. DOI: [10.1039/C7EE00332C](https://doi.org/10.1039/C7EE00332C).
- [193] T. Matsui, K. Maejima, A. Bidiville, H. Sai, T. Koida, T. Suezaki, M. Matsumoto, K. Saito, I. Yoshida, and M. Kondo, "High-efficiency thin-film silicon solar cells realized by integrating stable a-Si:H absorbers into improved device design," *Japanese Journal of Applied Physics*, vol. 54, no. 8S1, 08KB10, 2015. DOI: [10.7567/JJAP.54.08KB10](https://doi.org/10.7567/JJAP.54.08KB10).

- [194] K. Jäger, M. Fischer, R. A. C. M. M. van Swaaij, and M. Zeman, "A scattering model for nano-textured interfaces and its application in opto-electrical simulations of thin-film silicon solar cells," *Journal of Applied Physics*, vol. 111, no. 8, p. 083108, 2012. DOI: [10.1063/1.4704372](https://doi.org/10.1063/1.4704372).
- [195] A. N. Corpus-Mendoza, M. M. De Souza, and F. Hamelmann, "Transport mechanisms and effective Schottky barrier height of ZnO/ μ c-Si:H heterojunction solar cells," *Journal of Applied Physics*, vol. 114, no. 18, p. 184505, 2013. DOI: [10.1063/1.4831661](https://doi.org/10.1063/1.4831661).
- [196] A. Polman, M. Knight, E. C. Garnett, B. Ehrler, and W. C. Sinke, "Photovoltaic materials: Present efficiencies and future challenges," *Science*, vol. 352, no. 6283, aad4424, 2016. DOI: [10.1126/science.aad4424](https://doi.org/10.1126/science.aad4424).
- [197] R. E. Bird, C. Riordan, R. E. Bird, and C. Riordan, "Simple Solar Spectral Model for Direct and Diffuse Irradiance on Horizontal and Tilted Planes at the Earth's Surface for Cloudless Atmospheres," *Journal of Climate and Applied Meteorology*, vol. 25, no. 1, pp. 87–97, 1986. DOI: [10.1175/1520-0450\(1986\)025<0087:SSSMFD>2.0.CO;2](https://doi.org/10.1175/1520-0450(1986)025<0087:SSSMFD>2.0.CO;2).
- [198] A. Imenes and D. Mills, "Spectral beam splitting technology for increased conversion efficiency in solar concentrating systems: a review," *Solar Energy Materials and Solar Cells*, vol. 84, no. 1, pp. 19–69, 2004. DOI: [10.1016/j.solmat.2004.01.038](https://doi.org/10.1016/j.solmat.2004.01.038).
- [199] A. Mojiri, R. Taylor, E. Thomsen, and G. Rosengarten, "Spectral beam splitting for efficient conversion of solar energy—A review," *Renewable and Sustainable Energy Reviews*, vol. 28, pp. 654–663, 2013. DOI: [10.1016/j.rser.2013.08.026](https://doi.org/10.1016/j.rser.2013.08.026).

Acknowledgements

Five years after setting foot on Dutch soil, I still do not know what I did right in the interviews to prove myself a good candidate for this PhD position. With that being said, I would like to start my acknowledgement by thanking my promotor Prof.dr. Miro Zeman, as well as Dr. Olindo Isabella who is my copromotor and daily supervisor. Back then, they regarded me as the worthy candidate among other applicants. Today I still feel honoured and fortunate about it. Besides his regular support, Miro served as a great adviser, often providing me opinions from a very different mindset and perspective. His presence let me see a bigger world, and certainly helped me grow and improve over time. As a supervisor, Olindo is both passionate and rational. He is always open for scientific discussions. Just like his desire for ramen is not bound by the times of the day when he is in Japan, his emails may arrive at midnight or on weekend, offering his help and advices whenever I need. His support does not stay within research: there were so many instances that he encouraged me to recognize my own achievement, as a counter measure balancing against my modest character and self-criticism. A bonus fact: at the time I started in the project, he had not even obtained his doctorate degree; months before my doctoral defence, he became an associate professor. He certainly used his time better than I did.

My research described in this dissertation is not possible without the financial support from the Foundation for Fundamental Research on Matter (FOM, which was reorganized as NWO-I in 2017) and its research programme “Stirring of Light!”. In addition, it has been a pleasure to talk science with the fellows from other universities within the programme, namely Henriëtte E. Bakker, Diana Grishina, Shakeeb B. Hasan, Flavio Mariani, Oluwafemi S. Ojambati, and Leroy P.T. Schepers.

I must express my gratitude to the independent members of my doctoral committee, Prof.dr. A.W. Weeber, Prof.dr. P.M. Sarro, Prof.dr. R. Schlatmann, Dr.ir. J.J. Schermer, and Dr. J.-W. Schüttauf, for reviewing my thesis and attending the defence ceremony in spite of their busy schedule. Their feedback is valuable to me for the refinement of the thesis.

In the course of the PhD project, I have had the honour of collaborating with Dr. Adrien Bidiville and Dr. Takuya Matsui of (Japan) National Institute of Advanced Industrial Science and Technology (AIST), Dr. Bofei Liu and Prof.dr. Xiaodan Zhang of Nankai University, Dr. Piotr Kowalczewski and Prof.dr. Lucio Claudio Andreani of University of Pavia, and Dr. Subhendu Guha. I am grateful for the fruitful discussions we have had. I would also like to thank Dr. Franz-Josef Haug of PV-Lab of IMT, École Polytechnique Fédérale de Lausanne (EPFL) for permitting the use of certain TCO substrates in this work.

The Photovoltaic Materials and Devices (PVMD) Group granted me an excellent environment where I could freely experiment ideas, get inspired by the people, develop further as a researcher, and become who I am today. These were made possible by those whom I have worked with here: Prof.dr. Arno Smets, Dr. René van Swaaij, Martijn Tijssen, Stefaan Heirman, Remko Koornneef, Dr. Serge Solntsev, Dr. Rudi Santbergen, Dr. Klaus Jäger, Dr. Karol Jarolimek, Dr. Do Yun Kim, Dr. Dong Zhang,

Dr. Guangtao Yang, Marinus Fischer, Dr. Lihao Han, Dr. Pavel Babal, Dr. Jimmy Melskens, Dr. Hairen Tan, Dr. Mirjam Theelen, Dr. Andrea Ingenito, Dr. Ravi Vasudevan, Dr. Dimitris Deligiannis, Dr. Martijn van Sebille, Johan Blanker, Paula Perez Rodriguez, Robin Vismara, Nasim Rezaei, Hamed Ahmadpanahi, Xun Sun, Gianluca Limodio, Dr. Paul Procel, Thierry de Vrijer, Dr. Andrea Illiberi, Yuan Gao, Yilei Tian, Klaas Bakker, Juan Camilo Ortiz Lizcano, Dr. Engin Özkol, Ana Rita Montes, and Dr. Hesam Ziar. I have been helped and enlightened in numerous ways, by them sharing scientific insights, offering technical support and know-how, engaging in discussions, demonstrating the good academic conduct, or giving me a hand in times of need. Precious memories have also been made beside the research time: the distraction office, the coffee corners, the weekly evaluation, the “dropper”, the frisbee city league, the spikeball o'clock, just to name a few. Lastly, I would like to acknowledge my debt to Hairen; without him, none of these would have happened in the first place.

I wish to express my sincere appreciation to Annette Bor, Laura Bruns, Sharmila Rattansingh, Ellen Schwencke-Karlas, Ilona van der Wenden, Claudia de Kooter, and Diana Vedder for the administrative assistance throughout the project. I am thankful to Dr. Cassan Visser, Dr. Gregory Pandraud, Silvana Milosavljevic, Mario Laros, Robert Verhoeven and Johan van der Cingel of Else Kooi Laboratory, and Hozanna Miro and Charles de Boer of Kavli Nanolab, for the technical support at the respective laboratories.

I have supervised or co-supervised a few MSc. thesis projects in the past years. It is great experience to work with Theodoros Papakonstantinou, Adwait Apte, Thierry de Vrijer, Ariyanto Wibowo Setia Budhi, and Ronald van Schie. I have learnt a great deal in the process.

I am lucky to have met my girlfriend Yi Hsiu Liu in Delft. Her company, encouragement and love mean a lot to me.

Last but not least, I can never thank my parents enough for their unconditional love and support. They always give me the best and ask for nothing in return. They are too kind to restrict me from pursuing what I want, even if it means that we shall live in two different continents and can only meet for less than ten days per year. Their hearts, while fragile, are strong.

感謝父母親給予我無保留的支持。

List of Publications

Articles on peer-reviewed journals

1. T. de Vrijer, **F. T. Si**, H. Tan, and A. H. M. Smets, "Chemical stability and performance of doped silicon oxide layers for use in thin-film silicon solar cells," *to be submitted*.
2. R. Vismara, O. Isabella, A. Ingenito, **F. T. Si**, and M. Zeman, "Geometrical optimization of core-shell nanowires for enhanced absorption in c-Si heterojunction c-Si solar cells," *to be submitted*.
3. **F. T. Si**, O. Isabella, and M. Zeman, "Too many junctions? — a case study of multi-junction thin-film silicon solar cells," *Advanced Sustainable Systems*, vol. 1, no. 10, p. 1700077, 2017. DOI: [10.1002/adsu.201700077](https://doi.org/10.1002/adsu.201700077).
4. **F. T. Si**, O. Isabella, H. Tan, and M. Zeman, "Quadruple-junction thin-film silicon solar cells using four different absorber materials," *Solar RRL*, vol. 1, no. 3–4, p. 1700036, 2017. DOI: [10.1002/so1r.201700036](https://doi.org/10.1002/so1r.201700036).
5. **F. T. Si**, O. Isabella, and M. Zeman, "Thin-film amorphous silicon germanium solar cells with p- and n-type hydrogenated silicon oxide layers," *Solar Energy Materials and Solar Cells*, vol. 163, pp. 9–14, 2017. DOI: [10.1016/j.solmat.2017.01.001](https://doi.org/10.1016/j.solmat.2017.01.001).
6. **F. T. Si**, O. Isabella, and M. Zeman, "Artifact interpretation of spectral response measurements on two-terminal multijunction solar cells," *Advanced Energy Materials*, vol. 7, no. 6, p. 1601930, 2017. DOI: [10.1002/aenm.201601930](https://doi.org/10.1002/aenm.201601930).
7. D. Y. Kim, E. Guijt, **F. T. Si**, R. Santbergen, J. Holovský, O. Isabella, R. A. C. M. M. van Swaaij, and M. Zeman, "Fabrication of double- and triple-junction solar cells with hydrogenated amorphous silicon oxide (a-SiO_x:H) top cell," *Solar Energy Materials and Solar Cells*, vol. 141, pp. 148–153, 2015. DOI: [10.1016/j.solmat.2015.05.033](https://doi.org/10.1016/j.solmat.2015.05.033).
8. H. Tan, E. Moulin, **F. T. Si**, J.-W. Schüttauf, M. Stuckelberger, O. Isabella, F.-J. Haug, C. Ballif, M. Zeman, and A. H. M. Smets, "Highly transparent modulated surface textured front electrodes for high-efficiency multijunction thin-film silicon solar cells," *Progress in Photovoltaics: Research and Applications*, vol. 23, no. 8, pp. 949–963, 2015. DOI: [10.1002/pip.2639](https://doi.org/10.1002/pip.2639).
9. **F. T. Si**, D. Y. Kim, R. Santbergen, H. Tan, R. A. C. M. M. van Swaaij, A. H. M. Smets, O. Isabella, and M. Zeman, "Quadruple-junction thin-film silicon-based solar cells with high open-circuit voltage," *Applied Physics Letters*, vol. 105, no. 6, p. 063902, 2014. DOI: [10.1063/1.4892890](https://doi.org/10.1063/1.4892890).

Oral presentations at conferences

1. **F. T. Si**, H. Tan, D. Y. Kim, G. Yang, R. Santbergen, R. A. C. M. M. van Swaaij, A. H. M. Smets, O. Isabella, and M. Zeman, "Quadruple-junction thin-film silicon solar cells using four different absorber materials," in *33rd European Photovoltaic Solar Energy Conference and Exhibition*, Amsterdam, The Netherlands, September 2017.
2. **F. T. Si**, O. Isabella, and M. Zeman, "Strategies towards high-efficiency quadruple-junction thin-film silicon-based solar cells," in *26th International Photovoltaic Science and Engineering Conference*, Singapore, October 2016.
3. **F. T. Si**, D. Y. Kim, R. Santbergen, H. Tan, R. A. C. M. M. van Swaaij, A. Bidiville, T. Matsui, A. H. M. Smets, O. Isabella, and M. Zeman, "Silicon-based quadruple-junction thin-film solar cells," in *2015 MRS Spring Meeting & Exhibit*, San Francisco, USA, April 2015.
4. **F. T. Si**, D. Y. Kim, R. Santbergen, H. Tan, R. A. C. M. M. van Swaaij, A. H. M. Smets, O. Isabella, and M. Zeman, "Quadruple-junction silicon-based thin-film solar cells," in *Physics@FOM Veldhoven 2015*, Veldhoven, The Netherlands, January 2015.
5. **F. T. Si**, D. Y. Kim, R. Santbergen, H. Tan, R. A. C. M. M. van Swaaij, A. Bidiville, T. Matsui, A. H. M. Smets, O. Isabella, and M. Zeman, "High V_{oc} silicon-based thin-film quadruple-junction solar cells," in *6th World Conference on Photovoltaic Energy Conversion*, Kyoto, Japan, November 2014.
6. **F. T. Si**, T. Papakonstantinou, O. Isabella, and M. Zeman, "Studies of light scattering effect of surface morphology on thin-film silicon solar cells facilitated by nano-imprint lithography," in *Photovoltaic Technical Conference 2014*, Aix en Provence, France, May 2014.

Poster presentations at conferences

1. **F. T. Si**, O. Isabella, and M. Zeman, "Modeling of spectral response measurements of two-terminal multi-junction solar cells," in *43rd IEEE Photovoltaic Specialists Conference*, Portland, USA, June 2016. DOI: [10.1109/PVSC.2016.7749889](https://doi.org/10.1109/PVSC.2016.7749889).
2. **F. T. Si**, O. Isabella, and M. Zeman, "On the spectral response measurements of monolithic multi-junction solar cells," in *Physics@FOM Veldhoven 2016*, Veldhoven, The Netherlands, January 2016.
3. **F. T. Si**, T. Papakonstantinou, A. Ingenito, G. Yang, H. Tan, O. Isabella, and M. Zeman, "Light scattering effect of nano-imprinted random textures on thin-film amorphous and nano-crystalline silicon solar cells," in *29th European Photovoltaic Solar Energy Conference and Exhibition*, Amsterdam, The Netherlands, September 2014.

Invited lecture

1. **F. T. Si**, D. Y. Kim, R. Santbergen, H. Tan, R. A. C. M. M. van Swaij, A. Bidiville, T. Matsui, A. H. M. Smets, O. Isabella, and M. Zeman, "High V_{oc} silicon-based thin-film quadruple-junction solar cells," Nankai University, Tianjin, China, 23 December 2014.

Curriculum Vitae

Fai Tong Si was born in Macau on 3 September 1987. He studied Materials Science at Fudan University in Shanghai, China, and obtained his B.Sc. degree in 2009. He received his M.Eng. degree in 2012 from Institute of Semiconductors, Chinese Academy of Sciences in Beijing, China, where he continued his study on Semiconductor Materials and Devices. The topic of his master thesis project is the deposition and characterization of graphene. Afterwards, he joined the Photovoltaic Materials and Devices Group at Delft University of Technology to pursue a doctorate. His PhD project focused on the light management of thin-film silicon-based solar cells and the implementation of multi-junction concept.

Contact

E-mail: faitong.si@gmail.com

LinkedIn: <https://www.linkedin.com/in/faitongsi/>

